5-2021

Expanding Band Parameter Analysis Methods for HED Meteorites and V-type Asteroids

Noah Adm Haverkamp Frere
University of Tennessee, Knoxville, nfrere@vols.utk.edu

To the Graduate Council:

I am submitting herewith a thesis written by Noah Adm Haverkamp Frere entitled "Expanding Band Parameter Analysis Methods for HED Meteorites and V-type Asteroids." I have examined the final electronic copy of this thesis for form and content and recommend that it be accepted in partial fulfillment of the requirements for the degree of Master of Science, with a major in .

Sean S. Lindsay, Major Professor

We have read this thesis and recommend its acceptance:

Andrew W. Steiner, Tony Mezzacappa

Accepted for the Council:
Dixie L. Thompson

Vice Provost and Dean of the Graduate School

(Original signatures are on file with official student records.)

Expanding Band Parameter Analysis Methods for HED Meteorites and V-type Asteroids

A Thesis Presented for the
Master of Science
Degree
The University of Tennessee, Knoxville

Noah Adm Haverkamp Frere
May 2021

dedication...

To my three goddesses who look after me and teach —
my goddess wife & soulmate, Jill Frere, who re-taught me how to be;
my goddess daughter, Santosha, born shortly after embarking on this journey;
and the ancient goddess Vesta, after whom the asteroid, without which this research would not exist, is named.

Acknowledgements

Thank you to those who welcomed me into the friendly Physics Department at UT, Knoxville — Chrisanne Romeo, queen of the department, who set the tone for my whole experience from the very first day of visiting; Dr. Marianne Breinig who was always there, and warmly welcomed me into graduate school when I was not sure I was going to end up going at all; the professors and staff who were as kind as could be, especially Dr. Christine Nattrass who always went above and beyond; and Paul Lewis, who provided rooftop telescopes, which provided an opportunity to just look deep into space and forget about the physics from time to time.

Thank you to Dr. David Fields, who always engaged me when it comes to physics and astronomy, and encouraged me from the very beginning.

Thank you to my committee members, Dr. Tony Mezzacappa and Dr. Andrew Steiner for taking the time to read this manuscript and judge my defense.

Thank you to my parents who embody kindness, and prioritize learning, hard work and growth.

Thank you to Dr. Jeffrey Edward Davis and MOCD (Milarepa Osel Cho Dzong) for granting me the space in their Smoky Mountain home and retreat center to allow me to focus on the writing process.

And lastly, thank you to my advisor and mentor, Dr. Sean S. Lindsay. I would not choose a different mentor if the whole word were available to choose from. He has all the qualities necessary to fulfill the role, as well as all the qualities necessary to be a noble human.

Abstract

Vesta and Vesta-like asteroids have been convincingly linked, through visible and near-infrared (VNIR; 0.7 - 2.5 µm [micron]) spectral analysis, to a clan of basaltic achondritic meteorites – howardites, eucrites, and diogenites (HEDs). VNIR reflectance spectra of V-type asteroids and HED meteorites have two absorption features centered near 1 µm (Band I) and 2 µm (Band II) caused primarily by Fe^{2+} [iron] and Ca^{2+} [calcium] cations in pyroxene. Previous studies have shown a correlation between the mol% Fs and Wo with the central wavelengths of Band I and Band II, hereafter called Band I Center (BIC) and Band II Center (BIIC). This dependency on mineral composition allows for the generation of calibration equations that link BIC and BIIC to mol% Fs and Wo, which can be applied to estimate the mineralogy of V-type asteroids from their NIR spectra. The ability to accurately determine BIC and BIIC wavelength positions is dependent on the signal-to-noise ratio (SNR) of the spectrum. The typical SNR of asteroid spectra is SNR ~ 50, noticeably lower than the SNR of meteorite spectra, which is about ten times higher. Sanchez et al. (2020) artificially reduced the SNR of the ordinary chondrite meteorite spectra to explore mineralogical determinations using S-type asteroid spectra of comparable SNR. Sanchez et al. (2020) also extended the applicability of S-type calibration equations to incomplete spectral data sets lacking visible data or having unreliable/incomplete data between 2.4 - 2.5 µm.

Here I performed a similar analysis on HEDs and V-type asteroids using a reduction in SNR for HED meteorite spectra. In addition, I used six versions of each spectra, covering wavelength ranges from five different terminal wavelengths (~0.75 and 0.8 µm for Band I; 2.4, 2.45, and 2.5 µm for Band II), mimicking incomplete spectral data sets. Like Sanchez et al. (2020), I found that the decreased SNR calibration equations mostly yielded a lower R^2, and an increased rms error, compared with their high SNR calibrations. I also created calibration equations using the minimum of Band I as an alternative to the center of Band I, and explored the efficacy of those equations. When applied to V-type asteroids, I found that the derived mineralogy from Band I is

systematically higher than that of Band II, but that averaging the results from both bands gives mineralogical results for the V-type asteroids most consistent with those of the HEDs. I discuss the potential reasons for this discrepancy, including SNR, temperature effects, the overall slope of the reflectance spectra, and space weathering.

Table of Contents

List of Tables

List of Figures

Chapter 1 ☽ Introduction

Our solar system comprises not only the eight planets with their moons revolving around the Sun, but also minor bodies such as comets and asteroids. Asteroids are rocky bodies that coalesced in the early stages of the solar system's evolution. There are millions, ranging in size from 1 meter across to almost 1000 km across (Rubin and Grossman, 2010). Most of them inhabit the Main Asteroid Belt (MBA), an area that spans much of the space between Mars and Jupiter. The second largest asteroid, 4 Vesta, was discovered in 1807 and occupies the MBA. Its mean diameter is 525 km (Russell et al. 2012) and is the brightest asteroid visible from earth, due to it's extremely high geometrical albedo of 0.423 (Tedesco et al. 2004).

Studying the evolution of the asteroids both in terms of chronology and distance from the Sun improves our understanding of the evolution of our solar system, which can then inform our models of solar systems other than ours. As the solar system evolved, asteroids migrated, collided, dismantled and reassembled. As they migrate closer to or further from the Sun, they sometimes are effected by, for example, the mean-motion resonances with Jupiter, or the $\nu 6$ secular resonance of Saturn, which can eventually act to forcibly eject asteroids from their habitual motion. Observations of asteroids near these resonance points suggest that debris from these types of asteroids may have eventually reached the earth as meteorites. Thus, studying the inclinations, eccentricities and orbital radii of asteroid families, and matching those types with meteorites, can elucidate our comprehension of the evolution of the solar system. Most of the V-type asteroids lie between the Jovian 3:1 and $\nu 6$ resonances, and are thus situated in a manner conducive to their potential ejection from the MBA (Wisdom 1985, (Migliorini et al. 1997).

High-quality reflectance spectra have been obtained for hundreds of asteroids, and many of these resemble Vesta's spectrum. The asteroids whose spectra resemble Vesta are thus thought to have come from Vesta, and are dubbed V-type asteroids. Since Vesta has a massive crater that spans almost the diameter of Vesta itself, and is 19 km deep, then Vesta must have been struck by a large asteroid or other solar system body,

which then excavated a large portion of its mantle and interior. The dimensions of this crater indicate excavation of ~10^6 km^3 of rock, which is more than enough to account for the known V-types (Thomas et al. 1997). A large part of this thesis is the examination of the spectra of 17 V-types (including Vesta).

McCord et al. (1970) found similarities in the spectral reflectance between Vesta and a group of mafic silicate meteorites called the HEDs (howardites, eucrites and diogenites). Over the ensuing decades, numerous studies have been performed linking the V-types to the HEDs (Consolmagno and Drake, 1977; Binzel et al. 1997; Gaffey 1997). There is substantial evidence that the HEDs may have originated in Vesta (Consolmagno and Drake 1977; Binzel and Xu 1993; Thomas et al. 1997; Drake 2001; McSween et al. 2013). It is also possible that some HEDs originated from a different parent body other than Vesta (Binzel and Lazarro 2000; Hardersen et al. 2004), as the dynamical properties of some V-type asteroids make it difficult to explain how these asteroids might have emerged from Vesta — that is, there may be other V-types that arose during the solar system's evolution independently of Vesta.

A few asteroids, including Vesta, were large enough to have differentiated in the early solar system, as a planet does, due to the heat from, for example, ^{26}Al, and gravitational forces, acting on its geochemical makeup. Thermal metamorphism is responsible for heterogeneous petrologies on Vesta, which mirrors the variety of compositions among HEDs (Yamaguchi et al. 1997, McSween et al. 2013). HEDs are achondrites, which means that the chondrules present in other types of meteorites, such as OCs (ordinary chondrites), are not present since they have melted in their parent body. This thesis attempts to improve techniques for linking HED meteorites with their probable V-type parent asteroids, which can then shed light on how and in what part of the solar system the solar nebula behaved to produce various kinds of protoplanets, which then were disrupted in the chaotic early environment of the solar system (Michel et al. 2015).

The spectra of V-types and HEDs contain two prominent absorption features centered around 1 and 2 µm, called Band I and Band II, respectively (see Figure 1). The electronic field transitions in the Fe2+ and Ca2+ cations in pyroxene are the main cause for these features (Clark, 1957; Burns, 1970; Adams, 1974; Cloutis and Gaffey, 1993; Burns, 1993). The relative amount of iron and calcium cause the absorption features to

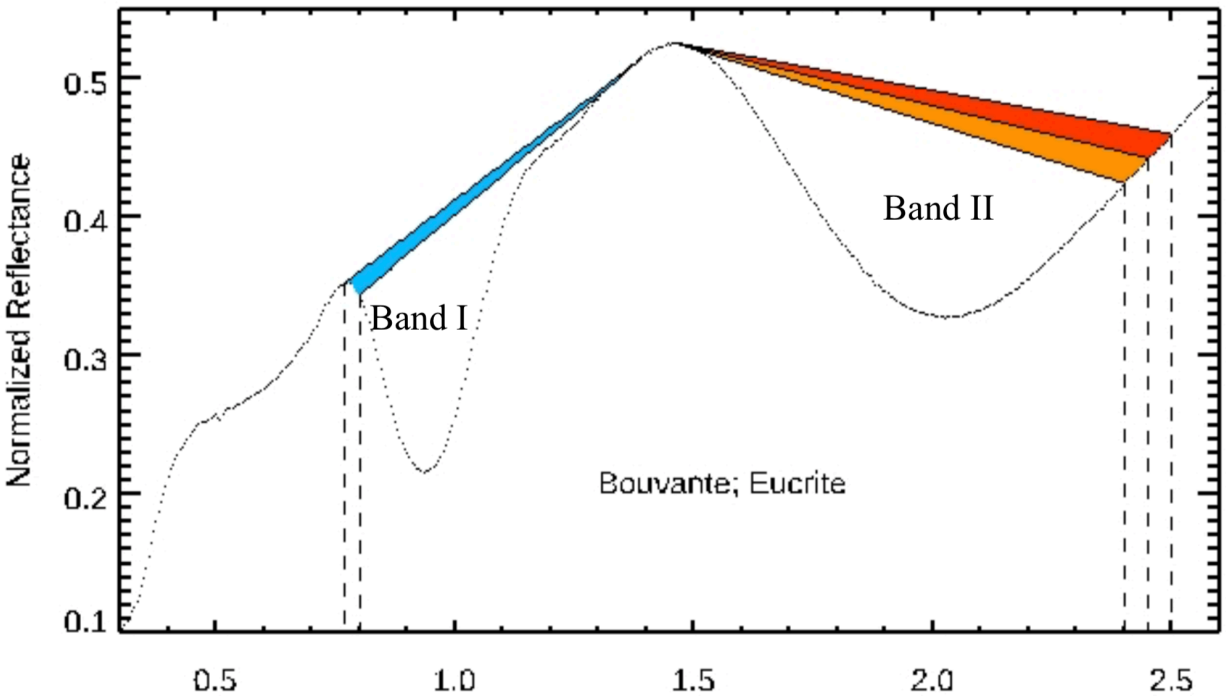

Figure 1: A graphical representation of the red edge problem. The blue and red hued shaded areas demonstrate how the choice of blue and red edge, respectively, affect the Band I and Band II straight-line continua.

slightly change in shape and position. The pyroxene quadrilateral is a map of the three end members of pyroxene: the iron-rich ferrosilite (Fs), magnesium-rich enstatite (En), and calcium-rich wollastonite (Wo — which doesn't occur as an end-member in nature). Band parameter analysis can be used to locate the band centers (Band I center, or BIC; and Band II center, or BIIC) of the 1- and 2-µm absorption features of a mafic silicate object's reflectance spectrum. Since the band centers have been linked to the amount of iron and calcium contained in these objects, we can make mineralogical determinations of the relative amount of Fs, En and Wo in that object. If that object under consideration is a meteorite, then the reflectance spectrum is obtained in a laboratory in controlled conditions, and the signal-to-noise ratio (SNR) of the spectrum is very high.

However, it is not so easy to obtain high SNR spectra of asteroids. All spectra of asteroids are obtained from earth-based telescopes, and the water in earth's atmosphere causes absorptions in the spectra that are difficult to impossible to remove. Additionally, asteroids are faint targets with the typical SNR of asteroid spectra being on the order of ten times lower than the spectra of meteorites (Sanchez et al. 2020). Figure 2 shows a typical V-type asteroid spectrum (2579 Spartacus). In addition, the asteroid spectra often lack the wavelength coverage needed to show the complete Band I and/or II. In this case, it is not possible to find the true BIC or BIIC, and thus the mineralogy cannot be calculated using the methods developed up to this point in time. The short-wavelength edge of the spectrum is dubbed the "blue edge," and hence the problems stemming from an incomplete or noisy (low SNR) blue edge are referred to as the "blue edge problem." This is similar to the "red edge problem" diagnosed by Lindsay et al. (2015), which addressed the noisy and/or truncated spectra of S-type asteroids and their meteorite analogs, the ordinary chondrites. One of the goals of this thesis is to find ways to overcome the problems associated with low SNR and/or truncated asteroidal spectra, for both the blue and red edges.

In order to retrieve mineralogical information from a spectrum, a calibration equation that links a band parameter to mineral content is required. Burbine et al. (2009, 2018) derived calibration equations linking Fs and Wo from HEDs to band minima and centers from their spectra. However, the band parameter technique used to obtain band centers vary from author to author, and thus the band centers calculated by one author may not agree with those that were used to determine Burbine's

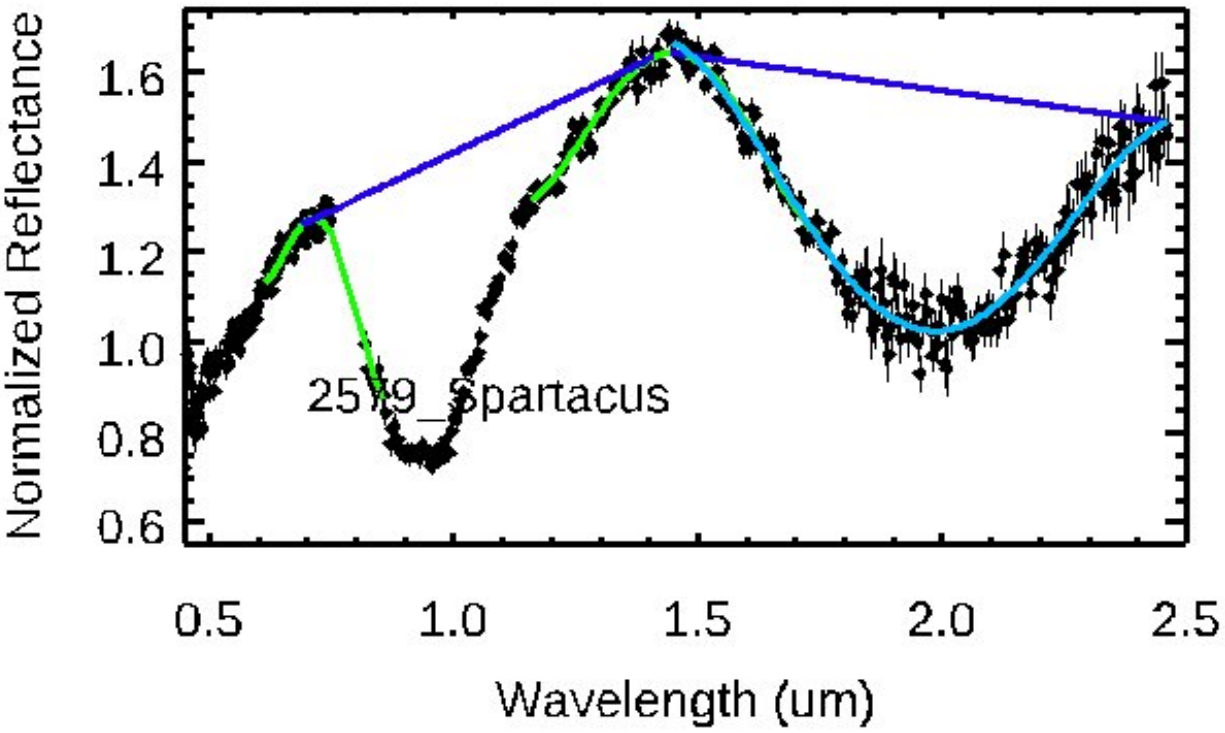

Figure 2: The VNIR spectrum of V-type asteroid 2579 Spartacus

calibration equations. In this case, using band centers in those equations will return incorrect mineralogical determinations. One of the main goals of this thesis is to provide the scientific community with a new set of calibration equations that are applicable to a wide variety of spectral conditions, including noisy and incomplete spectra. For example, many NIR asteroid spectra were obtained with spectrometers using a dichroic filter, which cuts off the short-wavelength edge of Band I (Sanchez et al. 2020). Often, a second spectrum from the visible wavelength range, complementing the NIR spectrum and thus completing Band I, does not exist. In that case, in order to calculate that asteroid's mineralogy, one needs to use a calibration equation computed from a spectrum that is truncated at the same blue edge as the asteroid spectrum. The left-most dashed vertical line in Figure 1 represent the "real" blue edge, which denotes the wavelength value of the local maximum reflectance points immediately short-ward of the Band I absorption feature (~.75 µm). The dashed line immediately to its right 0.8 µm represents the wavelength of a the blue edge of a truncated spectrum, hereafter called the false blue edge. The three dashed lines on the right represent the 2.5, 2.45 and 2.4 µm cut-offs for the red edge of the spectrum.

My thesis is organized as follows: In section 2, I introduce the meteorites used for the calibrations, which is the same HED sample that Burbine et al. (2009, 2018) used to calculate their calibration equations (which I call the "Burbine sample"). I also introduce another sample of 53 HEDs that are used in this thesis. This greater sample size is used to offset the small number statistics of the Burbine sample, which only contains 13 meteorites. I then introduce the 17 V-type asteroids chosen for this study, and describe my band parameter techniques. Section 3 comprises three subsections. Section 3.1 presents my band parameters and 12 calibration equations derived from the original ("clean") Burbine sample spectra. I show how the equations act on the 53 HED sample as well as the Burbine sample, and confirm that the equations return reasonable mineralogical determinations. I then present the slopes of the Band I continuum from both the real and false blue edge. Afterwards, I perform a frequency analysis similar to the one presented in Lindsay et al. (2015) and Sanchez et al. (2020), which shows how

often using band centers in the incorrect equation return derived mineralogy that is worse than the RMS error of the equations. I then introduce a new concept which I call "modified band I centers," with the aim of producing alternative band parameters that rely on the Band I slope (BIS). The goal here is to offset any anomalies in the calculated mineralogy for the asteroids that might result from BIS discrepancies. The final part of section 3.1 is a presentation of the HED zones — that is, the use of band parameter space to delineate separate boundaries for the howardites, eucrites, and diogenites (Gaffey et al. 1993; Moskovitz et al. 2010; Lindsay et al. 2015). Section 3.2 shows all the results that section 3.1 has, except for the case of the SNR50 Burbine sample spectra. Figure 3a shows the clean reflectance spectrum of the Johnstown diogenite (blue line). Figure 3b shows the same spectrum after artificially adding noise (blue line), in order to imitate the low SNR of a typical asteroid spectra. Section 3.3 presents the results from the asteroids. It begins with a discussion of temperature corrections to the band parameters, and then repeats the same themes outlined above. In chapter 4, I discuss two main themes. The first is an overview of the efficacy of the various calibrations presented in this thesis (there are 35 equations in all), and how they relate to the HED zones and meteorite analog assignments. The second is a discussion of a conundrum uncovered while calculating mineralogy for the asteroids — namely, the FsI (the mol% Fs derived from the Band I centers) over-estimates the mineralogy compared to what we expect, and the FsII (the mol% Fs derived from Band II centers) under-estimates the expected mineralogy. I present some potential reasons for this discrepancy, and discuss their merits or lack there-of.

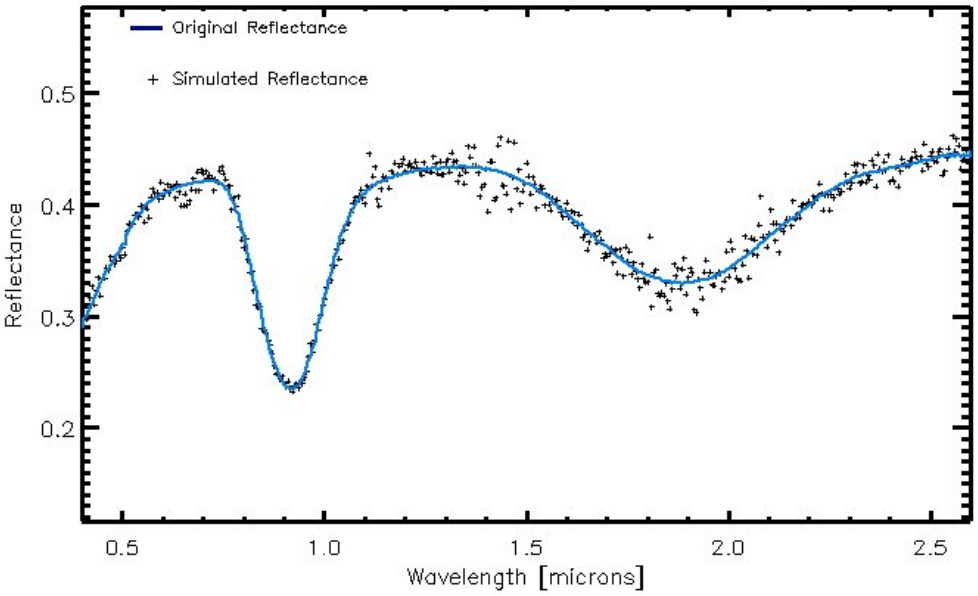

Figure 3a: Original Johnstown Diogenite spectrum

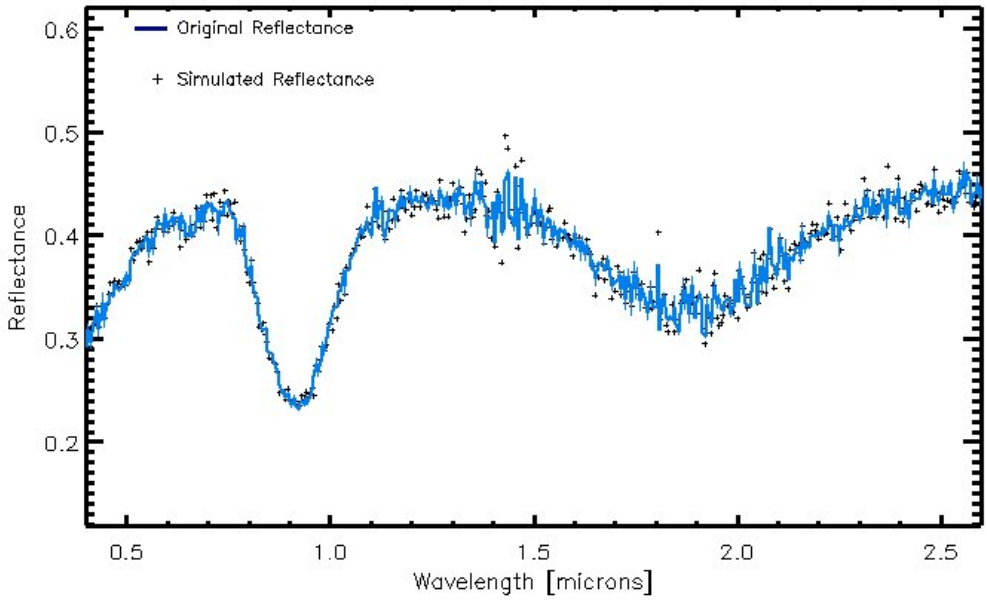

Figure 3b: SNR50 Johnstown Diogenite spectrum. The original reflectance values have had gaussian noise added in order to mimic a typical asteroid spectrum.

Chapter 2 ☽ Data & Methods

2.1 Data

2.1.1 Meteorites

For this study, we use a sample of 53 HED meteorites, composed of 34 eucrites, 12 howardite, and seven diogenites. All of the meteorites of the sample have visible+near-infrared (VNIR) wavelengths (0.3 - 2.6 μm). The reflectance spectra came from the bidirectional spectrometer at Brown University's Keck/NASA Reflectance Experiment Laboratory (RELAB) (Pieters and Hiroi 2004), taken at 0.005 μm wavelength intervals for samples with grain sizes of less than 25 μm. Only a subset of the HEDs with available VNIR reflectance spectra have also had their mineralogy determined in a laboratory setting. This suite of 13 HEDs (Bouvante, EETA79005, EET 87503, EET 87542, EET 90020, Johnstown, Juvinas, LEW 87004, Pasamonte, Petersburg, PCA 82502, Stannern, Tatahouine), hereafter called the "Burbine sample," are the same that were used in Burbine et al. (2007, 2009 & 2018). The Burbine sample contains ten eucrites, one howardite, and two diogenites. This sample was chosen because the pyroxene chemistries (mol% Fs, Wo, and En) have been determined in Burbine et al. (2001) by an Electron Microprobe Analysis (EMPA). The combination of reflectance spectra and known mineralogy allows us to construct calibration equations that correlate spectral band parameters to pyroxene chemistry. By comparing the derived mineralogy from the larger set of 53 with the EMPA mineralogy of the Burbine sample, we can quantify how robust our calibration equations are, which is useful when interpreting the derived mineralogy of the asteroids. The 39 HEDs outside the Burbine sample were also used in Moskovitz et al. (2010.)

2.1.2 Asteroids

This study uses a total of 17 asteroids with publicly available reflectance spectra. The reflectance spectra of six of the V-types, 809 Lundia, 3703 Volkonskaya, 3782 Celle, 3982 Kastel, 5481 Kiuchi, and 34706 2001op83, are from Lindsay et al. (2015). The 4 Vesta and 1929 Kollaa spectrum came from Reddy and Sanchez (2016). 1929 Kollaa has errors about an order of magnitude larger than any of the other spectra. This did not effect the band parameters of 1929 Kollaa, but it did double the mean errors. Not all of these 8 asteroid spectra have wavelength coverage out to 2.5 µm. In cases with incomplete coverage, extrapolation techniques were used to extend Band II out to 2.5 µm. This extrapolation method is described later in this section. The 2045 Peking spectrum is single NIR spectrum (0.435-2.4845 µm) from Moskovitz et al. (2010). It is the only unmodified asteroid spectrum used for a red edge of 2.5 µm band parameter analysis. For each of the other asteroids, visible and near-infrared (NIR) spectra were obtained from the Planetary Data System - Small Bodies Node, and combined into a single VNIR spectrum using an IDL routine. They are 2442 Corbett (NIR: Moskovitz et al. 2010; visible: Xu et al 1995, from the Small Main-belt Asteroid Spectrographic Survey (SMASS)); 4188 Kitezh (NIR: Sunshine et al 2004; visible: Bus & Binzel 2002 (SMASSII)); and the other six NIR and visible spectra from 2566 Khirgizia, 2579 Spartacus, 2581 Harbin, 2912 LaPalma, 3155 Lee, 51111 Jacliff were all obtained from Moskovitz et al. 2010, and Bus & Binzel 2002 (SMASSII), respectively. The two spectra were combined in an IDL routine provided by Sean S. Lindsay by using 3rd order polynomial fits to the visible and near-infrared spectra in a wavelength range that they overlap. The NIR data is then scaled to match the visible data in the region of overlap. Finally, the two pieces are merged together into a single visible + near-infrared spectrum.

All 17 asteroids were normalized to unity at 0.55 µm before spectral analysis was performed. All the V-types had errors given in their reflectance spectra, except for 2442 Corbett, to which we added a global .005 error. We attempted to use the same methods, described in the following section, for all spectra. However, there were some exceptions, which were necessary to obtain acceptable fits. Kiuchi had an extremely noisy spectrum

long-ward of 2.38 µm, so the noisy end of the spectrum was replaced with an extrapolation of a 4th order polynomial fit to Band II. This method has previously been successfully used by Lucas et al. (2019), who used 3rd order fits rather than 4th order. I then added the average error of the spectrum to that part of the fit. We thus ended up with a usable spectrum for input into SARA. To determine the band parameters, we used a 4th order polynomial fit for band II, instead of a 5th order fit (see § 2.2) only for the 2.5 µm red edge for Kiuchi. We used the same extrapolation technique on 34706 2001op83, with the points long-ward of 2.41 µm. For 3782 Celle, we did not alter the spectrum, but to determine the band parameters we fit a 6th order polynomial over band II rather than the 5th order.

2.2 Methods

The VNIR wavelengths relevant to this research range from 0.7 µm to 2.5 µm (Figure 1.) A primary goal of this thesis is to generate a new set of calibration equations to determine V-type mineralogy for a variety of observing conditions that lead to limited wavelength coverage. For observations that only have infrared reflectance data, which may not have coverage or reliable data short-ward of 0.8 µm, I explore the use of two blue edges for Band I: the "real" blue edge determined by the reflectance maximum near 0.75 µm, and a "false" blue edge of 0.8 µm. Frequently, the spectrometers (e.g., IRTF+ SpeX in PRISM mode) used to obtain asteroid spectra only obtain reliable data out to approximately 2.45 µm. Other facilities (e.g., TNG-NICS) only have wavelength coverage out to 2.40 µm. Because of these wavelength limitations, I explore three red edges for Band II: 2.40, 2.45, and 2.50 µm. These are the same red edges used by Lindsay et al. (2016) and Sanchez et al. (2020). In this study, all combinations of the two blue edges and three red edges give a total of 10 calibration equations.

Our band parameters are determined using the IDL-based Spectral Analysis Routine for Asteroids (SARA; Lindsay et al., 2015). In order to determine our band parameters, SARA first identifies four points that delineate the boundaries for the two absorption bands. Point(i) is the short-wavelength edge of Band I, called the blue edge;

point(ii) is the long-wavelength edge of Band I; point(iii) is the short-wavelength edge of Band II; and point (iv) is the long-wavelength edge of Band II, called the red edge.

For the real blue edge, point(i) is found by the following procedure: first SARA locates the maximum reflectance value just short-ward of Band I, around 0.75 µm; then it fits a 5th order polynomial to a 0.25 µm wavelength range centered at that maximum value; then it defines the maximum of that polynomial as point(i). Point(ii) is found as follows: first SARA locates the maximum reflectance value just long-ward of band I, around 1.4 µm; then it fits a 5th order polynomial to a 0.6 µm wavelength range centered at that maximum value, defining that as point(iii); SARA then draws a straight line, beginning at point(i), toward that polynomial, and defines point(ii) as the point where that continuum lies tangent to the polynomial. The Band I slope (BIS) is recorded as the slope of that continuum. In order to determine the BIC, SARA uses the following procedure: the reflectance values of the original spectrum are divided by the straight-line continuum; then a 3rd, 4th, and 5th order polynomial is fit to the bottom 60% of Band I — the band depth is taken to be one minus a ten-point boxcar smooth of the reflectance at the wavelength position of the band center. The BIC and BID (Band I depth) is the average of the minimums and depths, respectively, all three polynomials.

For the 0.8 µm blue edge, a 4th order polynomial is fit to the reflectance values of the wavelength range between 0.8 and 1.15 µm of band I. A 4th order fit gave a better polynomial than a 5th order for this blue edge. Point(i) is simply defined as the value of that polynomial at the 0.8 µm wavelength. The other Band I parameters are found in the same way as for the real blue edge.

For Band II, a 5th order polynomial is fit to the entire absorption feature. Point(iv) is defined as the value of that polynomial at either the 2.4, 2.45, or 2.5 µm wavelength. The BIIC is determined in the same way as the BIC, except the polynomials are fit to the bottom 50% of the band.

The band minimums (BIM and BIIM) are taken as the average of the minimum reflectance values of the three polynomial fits to Band I & II, respectively, prior to dividing by the continuum. Ideally, one would expect the minimum should be independent of the chosen edge. For the clean spectra, this is true. However, for the SNR50 spectral set, we found that although this is true for Band II, this is not the case for Band I. Since the polynomial fits are dependent on the chosen edge, and the false

blue edge is much closer in wavelength value to the absorption feature minimum than the real blue edge is, and since a 4th order polynomial was used for the false edge as opposed to a 5th order for the real edge, three HEDs from the Burbine sample exhibited a change of 0.005 µm in BIM when using the false blue edge. However, the mean BIM for the Burbine sample remained the same.

Band areas are measured as the area between the flat linear continuum and the continuum-divided smoothed reflectance values, using trapezoidal integration.

SARA calculates band parameter 1σ errors by performing 20,000 Monte Carlo simulations for all three orders of polynomial fits. First, gaussian noise commensurate with the level of SNR is added to the reflectance values, resulting in new spectra. The band centers and depths, for each polynomial fit, are recalculated for all 20,000 new spectra, and the errors are taken to be the standard deviation of the 20,000 remeasured centers and depths. The finalized band center and depth error is the average of the errors from each polynomial order. The error in band area is calculated in a similar manner, where 20,000 simulated spectra have their areas computed and the error in band area is taken to be the standard deviation of all measured band areas. See Lindsay et al. (2015) for further details on how SARA performs the spectral analysis calculations.

The meteorite spectra without reduction to the SNR were analyzed for all edge combinations first. This thesis refers to these spectra as the "clean" spectra. As stated in the Introduction, I introduced noise into the HED spectra in order to mimic the SNR of asteroid spectra. Using IDL, we added gaussian noise to each reflectance data point. The standard deviation of the Gaussian was set such that the reflectance divided by the gaussian noise averaged 25 for the 1.35 - 1.5 and 1.8 - 2.1 µm ranges, 37.5 for 1.1 - 1.175 µm, and 50 for the rest of the spectrum. The SNR was decreased to 1/2 and 3/4 to simulate loss of signal in the telluric water bands. The values were chosen to match a typical NASA IRTF with SpeX in Prism-mode reflectance spectrum. This spectral set will be referred to as "SNR50" from now on. Figure 3a and 3b show an example of a typical meteorite spectrum (Johnstown), before and after noise was added to it. Figure 2 shows a typical V-type spectrum (Spartacus) with polynomial fits produced by SARA.

Chapter 3 ☽ Results

One of the primary tasks of this thesis is to produce a set of calibration equations that are relevant to a range of observational scenarios where full wavelength coverage of Band I and Band II may not be available. Those equations are presented in two forms in this section. First, they are calculated using the nominal spectra from the Burbine sample; and secondly, they are calculated using the same sample, but altered by artificially added noise which mimics the typical SNR of observed asteroid spectra. I also derive calibration equations from the Band I Minima.

§ 3.1.1 presents the band parameters (the results of the band analysis techniques performed by SARA), for both the Burbine sample, and the set of 53 HEDs. In § 3.1.2 I will present the calibration equations from the clean spectra, after which, in § 3.1.3 I will apply those equations to the HEDs themselves and compare both the mineralogy from the different blue and red edge combinations to each other, and also to the EMPA molar contents. That will be followed by an analysis of the Band I slopes in § 3.1.4, which will become important in later sections on the asteroids. In § 3.1.5 I will quantify how frequently the truncated spectra cause problems in interpreting derived molar contents. § 3.1.6 introduces an alternative method for calculating modified Band I "centers." And finally, in § 3.1.7, I will separate the howardites, eucrites and diogenites into their own band parameter space, which I will refer to as the "HED zones" (Moskovitz et al. 2010).

3.1 Meteorites (Clean Spectra)

3.1.1 Band Parameters

Table 1 shows the band centers, band area ratios (BAR), Band I slopes (B1S), and the EMPA Fs and Wo mol% from the real, 2.5 µm edge combination for the 13 HEDs with known molar contents. The mean and standard deviations of the whole collection, as well as of just the eucrites and diogenites, are also listed. The mean of the howardite is not relevant since there is only one. The slopes vary greatly, though they are all above zero (this is relevant because that is not always the case with either HEDs or V-type asteroids). Since these thirteen Burbine sample HEDs are the only ones with known molar contents, it is important to analyze their band parameters as an independent data set. Not only is the Burbine sample necessary to develop calibration equations, but it will be useful when comparing the HEDs with V-type asteroids. However, we also determined the band parameters of a set of 53 HEDs (which includes the Burbine sample), four of which have a negative slope. This sample consists of 34 eucrites, seven diogenites, and 12 howardites, and hence we were also able to obtain a howardites mean with this dataset. Rather than perform a full analysis on all the edge combinations with this set of 53 meteorites, I chose to constrain my analysis of this larger set to only certain elements of my research. Therefore, I present the mean band parameters of the real, 2.5 µm edge combination in Table 2. In order to verify that this larger set is representative of the calibrations formulated from the Burbine sample, I compare the band parameters (and molar contents, to be discussed in the next section) in Table 3. The mean BIC and BIIC values between the two sets differ by only 0.001 µm, the mean BAR differs by only 0.043, and the mean BIS by 0.087. All of these are well within the range of the standard deviations of either set, thus assuring that I may confidently use the larger sample of 53 HEDs in my comparison with V-type asteroids.

3.1.2 Calibration Equations

Following the work of Burbine et al. (2009, 2018), I derived calibrations equations connecting the Burbine sample Fs and Wo molar abundance to Band I & II centers. The calibration equations were determined by performing a linear fit to the BIC and BIIC band parameters and the mol% Fs and Wo values determined by EMPA. Using this

Table 1: Burbine Sample HEDs with known molar contents. A real blue edge and 2.5 µm red edge were used to generate these results. Meteorites are arranged from low to high Wollastonite.
† These are average pyroxene mineralogies from electron microprobe analysis.

Meteorite	Type	BI Center (µm)	BII Center (µm)	BAR	Band I Slope	EMPA Fs † (mol%)	EMPA Wo † (mol%)
Tatahouine	Dio	0.920	1.895	1.690	0.05	23.0	1.5
Johnstown	Dio	0.917	1.885	1.390	0.02	23.5	2.8
EET87503	How	0.928	1.950	1.365	0.04	40.3	8.1
Petersburg	Euc	0.933	1.975	1.763	0.09	40.6	9.4
Stannern	Euc	0.938	2.008	1.703	0.14	55.8	9.6
EETA79005	Euc	0.933	1.967	1.790	0.16	43.2	10.3
LEW87004	Euc	0.933	1.973	1.473	0.14	45.0	11.0
Juvinas	Euc	0.935	1.995	1.520	0.10	51.8	11.3
EET87542	Euc	0.940	1.993	1.245	0.04	44.0	13.0
EET90020	Euc	0.938	2.005	1.057	0.00	53.0	13.0
Pasamonte	Euc	0.938	2.002	1.462	0.14	43.5	13.7
PCA82502	Euc	0.940	2.012	1.960	0.23	53.0	14.0
Bouvante	Euc	0.943	2.010	1.907	0.26	53.5	14.0
All HEDs Mean	-	0.934 ±0.008	1.975 ±0.042	1.563 ±0.26	0.110 ±0.079	43.9 ±10.6	10.1 ±4.0
Eucrites Mean	-	0.937 ±.003	1.994 ±.017	1.588 ±0.29	0.131 ±0.078	48.3 ±5.6	11.9 ±1.8
Diogenites Mean	-	0.918 ±0.002	1.890 ±0.007	1.540 ±0.21	0.035 ±0.024	23.3 ±0.4	2.2 ±0.9

Table 2: Band parameters and molar contents for the set of 53 HEDs from using the real, 2.5 µm edges and associated calibration equations.

Means	BIC (µm)	BIIC (µm)	BAR	Slope	FsI (mol%)	FsII (mol%)	Fs ave (mol%)	WoI (mol%)	WoII (mol%)	Wo ave (mol%)
53 HEDs	0.935 ±0.010	1.974 ±0.044	1.647 ±0.300	0.087 ±0.066	44.1 ±10.5	43.1 ±9.7	43.6 ±9.8	10.2 ±4.2	9.9 ±3.6	10.0 ±3.8
Eucrites n=34	0.939 ±0.006	1.995 ±0.023	1.619 ±0.319	.101 ±0.077	50.2 ±7.0	48.8 ±5.4	49.5 ±5.7	12.7 ±2.8	12.0 ±2.0	12.3 ±2.2
Diogenites n=7	0.920 ±0.002	1.899 ±0.009	1.751 ±0.265	0.046 ±0.014	27.4 ±3.0	25.7 ±2.2	26.5 ±2.3	3.6 ±1.2	3.3 ±0.8	3.4 ±0.9
Howardites n=12	0.928 ±0.004	1.949 ±0.019	1.720 ±0.193	0.073 ±0.038	36.9 ±4.5	37.6 ±4.5	37.3 ±4.3	7.4 ±1.8	7.8 ±1.7	7.6 ±1.7

Table 3: Compares the Burbine Sample to the sample of 53 HEDs. This shows the difference between the two data sets for the real, 2.5 µm edges. All results are within one standard deviation of the Burbine sample except those in red. For the Howardites, since there is no standard deviation possible from the Burbine sample (n=1), the standard deviation from the sample of 53 HEDs was used instead.

Means	ΔBIC (µm)	ΔBIIC (µm)	ΔBAR	ΔBand I Slope	ΔFsI (mol%)	ΔFsII (mol%)	ΔFs ave (mol%)	ΔWoI (mol%)	ΔWoII (mol%)	ΔWo ave (mol%)
53 HEDs	0.001	0.001	0.043	0.037	0.2	0.8	0.2	0.1	0.2	0.1
Eucrites	0.002	0.001	0.031	0.030	1.9	0.3	1.1	0.8	0.1	0.4
Diogenites	0.002	0.009	0.211	0.011	2.3	2.1	2.2	0.9	0.8	0.8
Howardites	0.000	0.001	0.355	0.033	0.4	0.4	0.3	0.1	0.1	0.1

method, two sets of five calibration equations were produced: one set for mol% Fs and one set for mol% Wo. The Fs and Wo sets each include two equations for mineralogy using BICs from the real and false blue edges, and three equations for mineralogy using BIICs from the three red edge values (2.40, 2.45, and 2.50 µm). The 10 equations are given in Table 4.

My examination of meteorite and asteroid spectral sets, using different red and blue edges, at different SNR, parallels the work of Sanchez et al. (2020). We started this project to build a parallel HED/V-type paper to the Sanchez et al. (2020) OC/S-type paper. This parallel project largely remains the core of this thesis.

One of these calibrations, Fs vs. BIC, is compared to my rendition of the Burbine et al. (2009) and Burbine et al. (2018) calibration equations in Figure 4. Note that Burbine et al. (2009) uses the Band I Minimum instead of BIC. As seen in Figure 4, most of my data points (black dots) have smaller BICs compared to Burbine's. However, my lowest value is ~ 0.002 µm higher than Burbine et al. (2009)'s lowest value (red disk). This results in a steeper calibration best-fit line, with a noticeably higher coefficient. I found this steeper trend in all ten calibration equations. Burbine et al. (2018) re-derived calibration equations using different band parameter techniques than they used in 2007. Interestingly, the BIC of only one meteorite, Johnstown (green circle at 0.92 µm in Fig. 2), differed from their 2009 BICs. It has a much higher value than the 2009 BIC, which has the effect of a noticeably steeper best-fit line, putting the coefficient about halfway between mine and Burbine's 2009 coefficient. All of Burbine's 2018 equations had larger coefficients than Burbine's 2009 equations, but not so large as mine presented here. This result highlights the need to use calibration equations that match the band parameter analysis method they were derived from. Table 5 lists both sets of Burbine's equations alongside the ones I derived.

Figure 5 shows our mol% Fs Band I calibration from both the real and false blue edge. For the false blue edge, the meteorites with the lowest two values (Johnstown and Tatahouine) have shifted comparatively far to longer wavelengths, yielding a much steeper best-fit line. The mol% Wo calibration plots share the same features, and the equations are listed in Tables 4 and 5.

The R^2 goodness of fit statistics are shown in the tables where the equations are reported, and are calculated as follows:

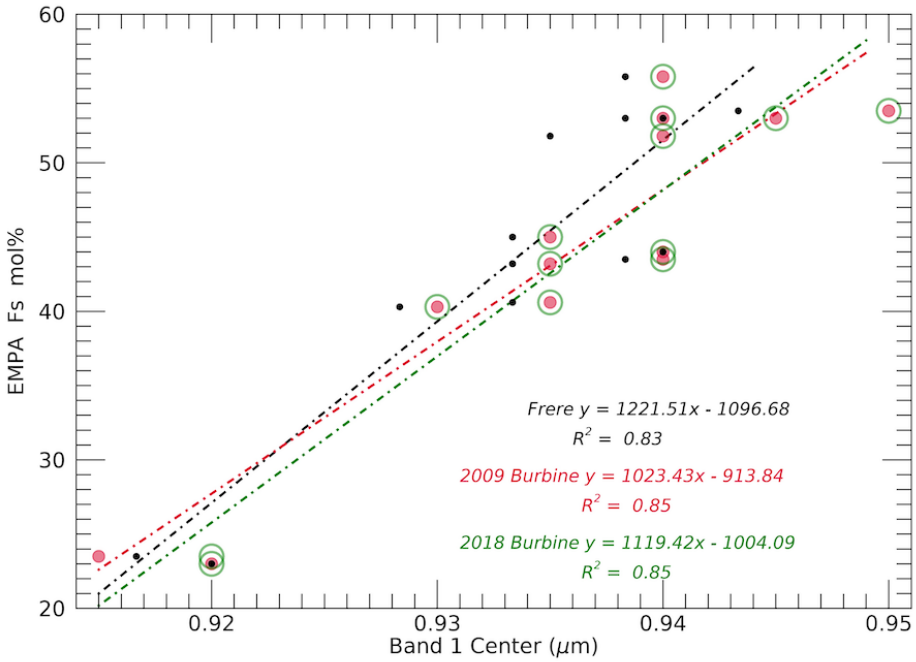

Figure 4: Real, 2.5 µm edge FsI calibration equation from the best fit to the black dots, compared with both of Burbine's FsI equations.

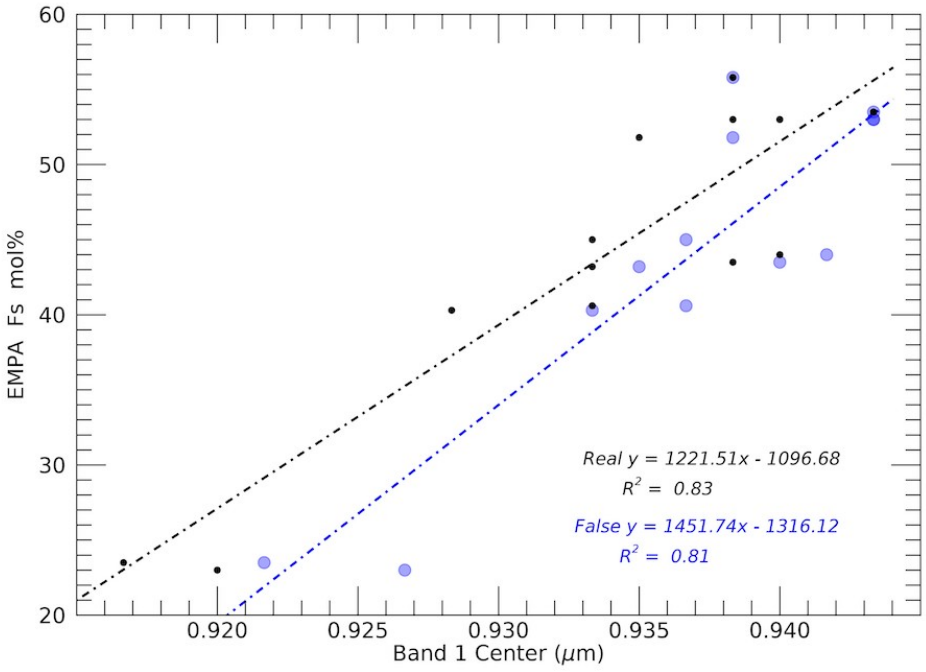

Figure 5: Band 1 Calibrations from the Real and False Blue Edge.

Table 4: Calibration Equations from this paper (Clean spectra)

Blue Edge	Mol% Fs Equation	R^2	RMS	Mol% Wo Equation	R^2	RMS
Real	Fs I = 1221.51×B1C - 1096.68	0.83	4.2	Wo I = 486.41×B1C - 444.04	0.88	1.2
False (0.8 µm)	Fs I = 1451.74×B1C - 1316.12	0.81	4.5	Wo I = 585.56×B1C - 538.42	0.91	1.2
Red Edge						
2.5 µm	Fs II = 239.85×B2C - 429.75	0.91	3.0	Wo II = 90.23×B2C - 168.04	0.89	1.3
2.45 µm	Fs II = 250.84×B2C - 450.49	0.92	3.0	Wo II = 93.82×B2C - 174.76	0.88	1.3
2.4 µm	Fs II = 263.06×B2C - 473.01	0.90	3.2	Wo II = 100.03×B2C - 186.42	0.90	1.2

Table 5. Calibration equations from three papers.

	Burbine 2007	Burbine 2018	Frere 2020
Fs I =	1023.4×BIC - 913.82	1119.4×BIC - 1004.1	1221.51×BIC - 1096.68
Wo I =	396.13×BIC - 360.55	436.31×BIC - 398.33	486.41×BIC - 444.04
Fs II =	205.86×BIIM - 364.3	223.15×BIIC - 398.91	239.85×BIIC - 429.75
Wo II =	79.905×BIIM - 148.3	85.342×BIIC - 159.21	90.23×BIIC - 168.04

$$R^2 = 1 - \frac{\sum_{i=1}^{n} (y_i - y_{fit,i})^2}{\sum_{i=1}^{n} (y_i - \bar{y})^2} \quad (1)$$

Where y_i is the value along the y-axis, $y_{fit,i}$ is the linear fit to the data, and $\bar{y}$ is the average value of those data points. Considering the ferrosilite, my Band I equations have R^2 values of 0.83 and 0.81 for the real and false edge, respectively, slightly lower than Burbine et al's 0.85 and 0.89, both from their real blue edge, from 2009 and 2018, respectively (Tables 4 & 5). For Wollastonite, my Band I equations have R^2 values of 0.88 and 0.91 for the real and false edge, respectively, equal to and higher than Burbine et al's 0.88 and 0.85, both from their real blue edge, from 2009 and 2018, respectively.

The RMS (root mean square) error describes the difference between the actual EMPA mol% and the predicted mol%, and is calculated as follows:

$$RMS = \sqrt{\frac{\sum_{i=1}^{n} (y_i - y_{fit,i})^2}{n}} \quad (2)$$

My RMS errors for FsI are ±4.2 and ±4.5 mol% for the real and false edge, respectively, compared with Burbine et al's ±3.3 and ±4 mol%, both from their real blue edge, from 2009 and 2018, respectively. My RMS errors for WoI are ±1.2 mol% for both the real and false edge, compared with Burbine et al's ±1.1 and ±1 mol%, both from their real blue edge, from 2009 and 2018, respectively. Note that Burbine's 2018 paper only gives one significant figure for RMS.

Figure 6 shows all three of my Fs Band II calibration equations. They are more similar to each other than the two Band I equations are to each other. The more the red edge is truncated, the more the BIICs shift to shorter wavelengths. The meteorites with the two lowest values — lower in both the BIIC and mol% Fs — (Johnstown and Tatahouine) shift the least of all the meteorites (the exact opposite of the situation for Band I, wherein they shifted the most), which has the same consequence of progressively steeper best-fit lines for the more truncated red edges. My Fs Band II equations have R^2

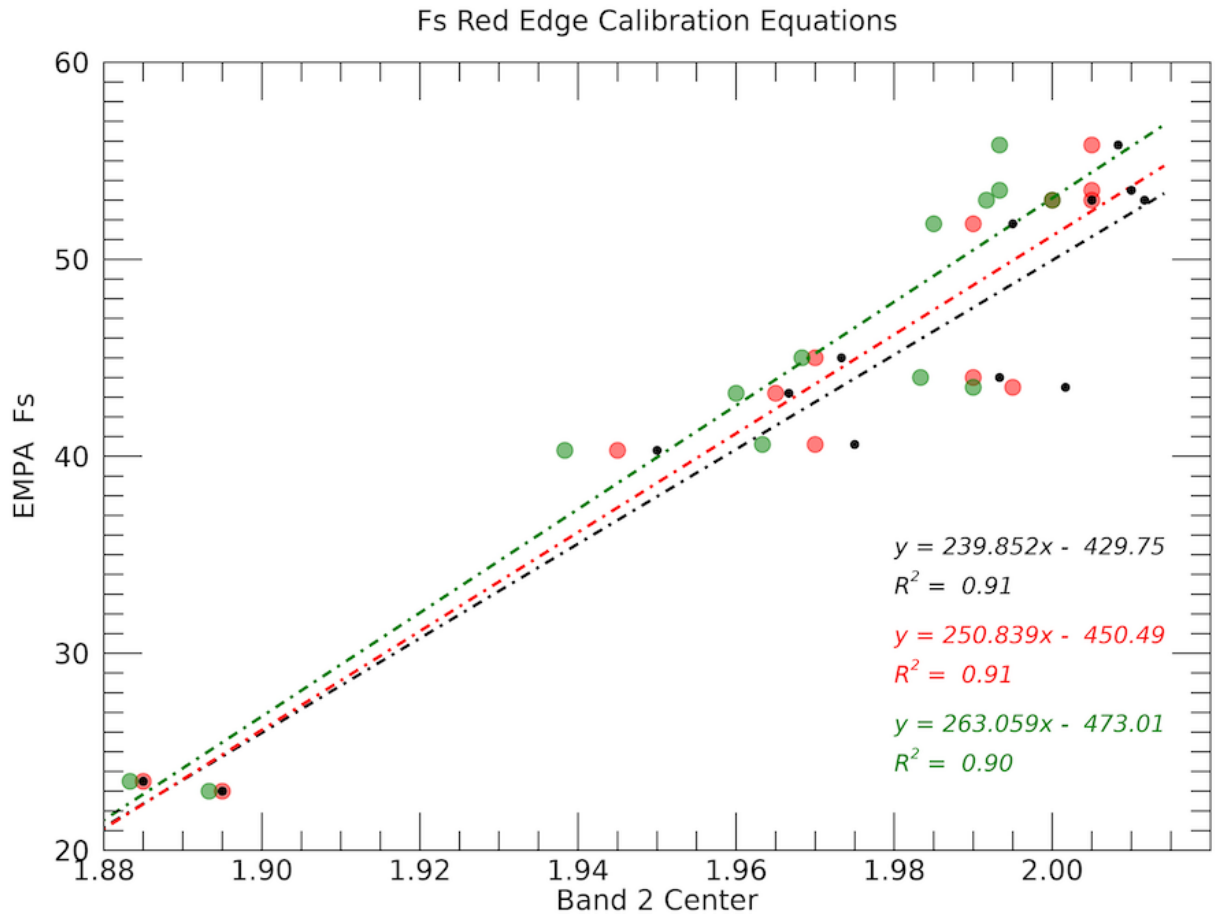

Figure 6: Band 2 Calibrations from the 2.5 µm (black), 2.45 µm (red), and 2.4 µm (green) red edges.

values of 0.91, 0.92 and 0.90 for the 2.5, 2.45 and 2.4 µm red edges, respectively, a bit higher than Burbine's 0.84 and 0.87, from 2009 and 2018, respectively. Note that Burbine's 2009 Band II calibration assumes Band II minima are equivalent to Band II centers, which does not require a red edge cut-off, while their 2018 Band II calibration uses Band II centers. My Wo Band II equations have R^2 values of 0.89, 0.88 and 0.90 for the 2.5, 2.45 and 2.4 µm red edges, respectively, slightly higher than Burbine et al's 0.87, from both their 2009 and 2018 papers.

My RMS errors for FsII are ±3.0 mol% for the 2.5 and 2.45 µm edges, and ±3.2 mol% for the 2.4 µm edge, compared with Burbine et al's (2009) ±3.3 from his Band II minimum equation, and Burbine et al's (2018) ±3 mol% from their 2.5 µm red edge. My RMS errors for WoI are ±1.3 mol% for the 2.5 and 2.45 µm edges, and ±1.2 mol% for the 2.4 µm edge, compared with Burbine et al's (2009) ±1.1 from his Band II minimum equation, and Burbine et al's (2018) ±1 mol% from their 2.5 µm red edge. The band parameters for all edge combinations are shown in Table 6.

Although the BIC and BIIC calibration equations are robust when determining mol% on HEDs (§ 3.1.3), in § 3.3.2 I will show that the BIC equations are less accurate when used on asteroids. This may be in part because the Band I slopes for the meteorites and asteroids are so different from one another (to be shown in § 3.3.3). Although BIMs from clean spectra are theoretically independent of blue edge, they are affected by slope of the continuum. Indeed, the reason for using BICs is to remove any differences caused by the continuum to find the maximum point of absorption in the feature, i.e., the band center. However, since the HED meteorite slopes are so different, and change differently for Band I and Band II slopes, from the V-type asteroid slopes, dividing by the continuum does not seem to produce the expected results of Band I and Band II calibration equations yielding the same mol% (within the uncertainties).

Another slope consideration, is the difference in Band I slopes between using the real and false blue edge. While we demonstrated that the false blue edge calibration equations give reliable mineralogy determinations for meteorites (Table 6), we will show that this is not the case for asteroids in § 3.3. A potential explanation for this is the large difference in HED and V-type Band 1 Slopes. The artificial imposition of a steep slope by using the false blue edge creates B1Cs that are artificially larger than the "real" BIC. As the slope increases, the measured B1C will also increase. Since the Band I

Table 6: Burbine Sample HED's mol% Fs from all edge combinations.
† These are average pyroxene mineralogies from electron microprobe analysis.

Meteorite	Real Blue FsI	False Blue FsI	2.5 Red FsII	2.45 Red FsII	2.4 Red FsII	Real/ 2.5 Fs Ave	Real/ 2.45 Fs Ave	Real/ 2.4 Fs Ave	False/ 2.5 Fs Ave	False/ 2.45 Fs Ave	False/ 2.4 Fs Ave	EMPA Fs †
Tatahouine	27.1	29.2	**24.8**	24.9	25.0	25.9	26.0	26.1	27.0	27.0	27.1	23.0
Johnstown	**23.0**	21.9	22.4	22.3	22.4	22.7	22.7	22.7	22.1	22.1	22.2	23.5
EET 87503	37.3	**38.8**	38.0	37.4	36.9	37.6	37.3	37.1	38.4	38.1	37.9	40.3
Petersburg	**43.4**	43.7	44.0	43.7	43.5	43.7	43.5	**43.4**	43.8	43.7	43.6	40.6
Stannern	49.5	46.1	51.9	**52.4**	51.3	50.7	51.0	50.4	49.0	49.3	48.7	55.8
EETA 79005	**43.4**	41.3	42.0	42.4	42.6	42.7	42.9	**43.0**	41.6	41.8	41.9	43.2
LEW 87004	43.4	43.7	43.6	43.7	**44.8**	43.5	43.5	44.1	43.6	43.7	44.2	45.0
Juvinas	45.4	46.1	48.7	48.7	**49.2**	47.1	47.1	47.3	47.4	47.4	47.6	51.8
EET 87542	51.5	50.9	**48.3**	48.7	48.7	49.9	50.1	50.1	49.6	49.8	49.8	44.0
EET 90020	49.5	**53.4**	51.1	51.2	50.9	50.3	50.3	50.2	52.3	52.3	52.1	53.0
Pasamonte	49.5	**48.5**	50.3	49.9	50.5	49.9	49.7	50.0	49.4	49.2	49.5	43.5
PCA 82502	51.5	53.4	52.7	52.4	**53.1**	52.1	52.0	52.3	**53.1**	52.9	53.2	53.0
Bouvante	55.6	53.4	52.3	52.4	51.3	54.0	54.0	**53.5**	52.9	52.9	52.4	53.5
All HEDs Mean	43.9 ±9.6	43.9 ±9.5	43.9 ±10.1	43.9 ±10.1	43.9 ±10.8	43.9 ±9.8	43.9 ±9.8	43.9 ±9.8	43.9 ±9.7	43.9 ±9.7	43.9 ±9.7	43.9 ±10.6
Eucrites Mean	48.3 ±4.2	48.0 ±4.5	48.5 ±4.0	48.6 ±3.9	48.6 ±3.7	48.4 ±3.9	48.4 ±3.9	48.4 ±3.8	48.3 ±4.1	48.3 ±4.1	48.3 ±3.9	48.3 ±5.6
Diogenites Mean	25.1 ±2.9	25.5 ±5.1	23.6 ±1.7	23.6 ±1.8	23.7 ±1.9	24.3 ±2.3	24.3 ±2.3	24.4 ±2.4	24.6 ±3.4	24.6 ±3.5	24.6 ±3.5	23.3 ±0.4

Slopes of the V-types are much larger than they are for the HEDs, which the calibration equations are derived from, this will lead to an overestimation of the mol% Fs and Wo for V-types. This error in BIC may be larger than the error involved with using B1M instead of a real BIC for the asteroids. In response to this, I produced calibration equations using the Band I Minimum instead of the Band I Center for IR-only data because it is not dependent on blue edge choice. If the error from using "false" BICs is larger than the BIM errors, then I recommend that BIMs and their related calibration equation should be used in cases of NIR-data only without an identifiable 0.75 µm reflectance maximum (see § 4.2). Figure 7 is the same as Figure 4 except it uses the BIM instead of the BIC (Burbine's equations are unchanged). The resulting calibration equation's coefficient is higher than all other Band I equations from the clean spectra presented in this thesis. The calibration equations using the BIM are presented in Table 7, including the SNR50 results, which will be addressed in § 3.2.1.

3.1.3 Applicability of the Calibration Equations

The prevailing assumption is that calibration equations from HEDs can be used to accurately retrieve mineralogy for V-types (Gaffey et al. 2002, Burbine et al 2007, 2009, 2018; Hardersen et al. 2018). However, my results suggest that care is needed when interpreting the derived modal abundance from the different absorption features. If the two bands give disparate results, then that introduces some doubt into the effectiveness of the calibration equations as applied to asteroids. Table 6 shows the derived mol% for the Burbine sample from all edges, for Band I (FsI), Band II (FsII), the mean of those two bands [Fs Ave = (FsI+FsII)/2], and EMPA. Note that the average of the two bands is frequently used in the literature (Burbine et al. 2009; Lindsay et al 2015; Hardersen et al. 2018). Table 8 shows the same for Wollastonite. The mean mol% Fs, for the Burbine sample as a whole, is nearly identical for all edges and combinations, matching the EMPA mean. The same is true for mol% Wo. This is important, as it shows that each calibration equation produces mineralogical results in agreement with the measured EMPA compositions. In Section 3.3., we will see that the derived molar contents for the asteroids is not so consistent when using different edges and absorption features. I have outlined and bolded the entries closest in mol% to the EMPA values. There is no single

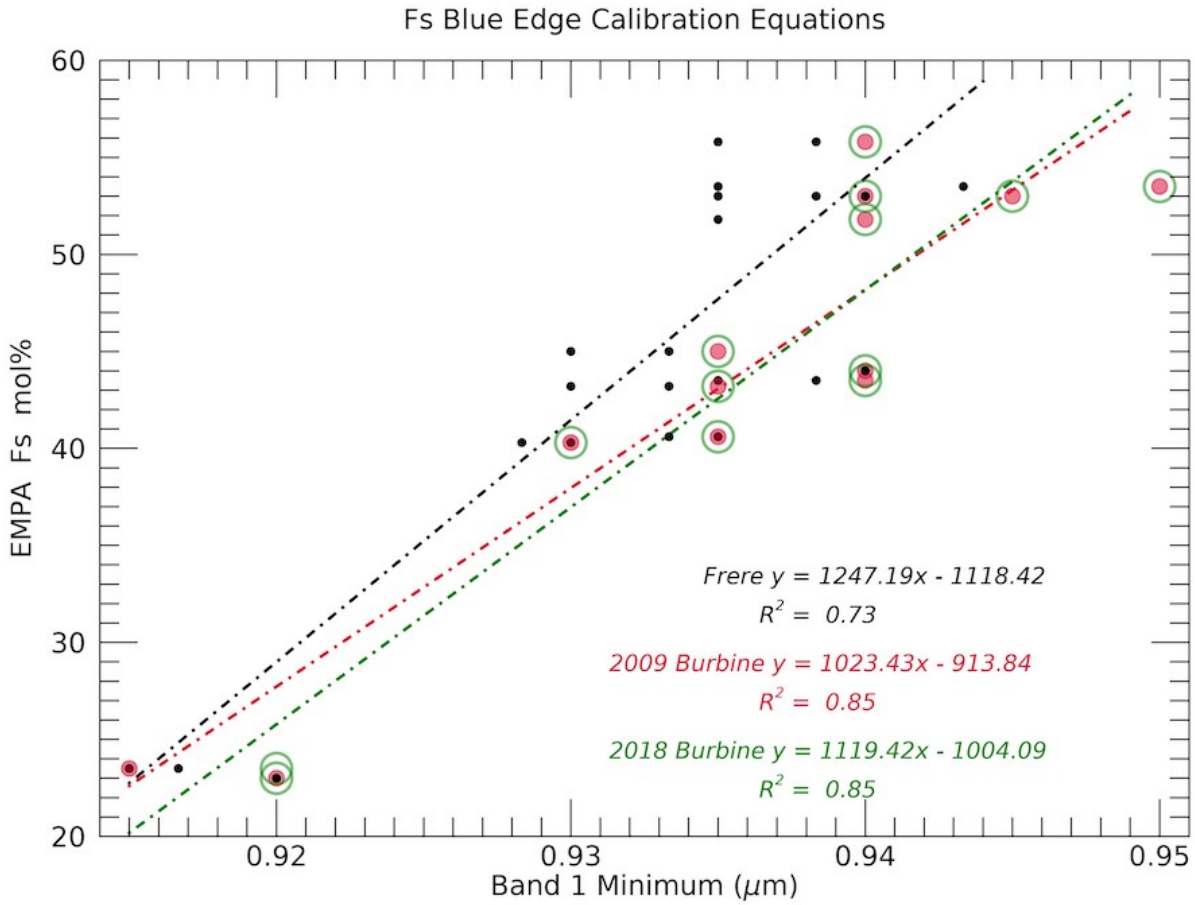

Figure 7: Frere's Fs Min Band I Calibration Equation. The x-axis shows Band 1 Minimums for Frere's and Burbine's 2009 data points, but Burbine's 2018 data points use the B1 Centers.

Table 7: Band 1 Minimum Calibration Equations

Blue Edge	Mol% Fs Equation	R^2	RMS	Mol% Wo Equation	R^2	RMS
Clean	Fs I = 1247.19×B1M - 1118.42	0.73	5.3	Wo I = 494.02×B1M - 450.26	0.79	1.8
SNR 50 (real)	Fs I = 1436.7×B1M - 1293.9	0.70	5.5	Wo I = 585.63×B1M - 535.18	0.81	1.7
SNR 50 (false)	Fs I = 1380.8×B1M - 1241.4	0.84	4.1	Wo I = 541.43×B1M - 493.81	0.90	1.3

Table 8: Burbine Sample HED's mol% Wo from all edge combinations.
† These are average pyroxene mineralogies from electron microprobe analysis.

Meteorite	Real Blue WoI	False Blue WoI	2.5 Red WoII	2.45 Red WoII	2.4 Red WoII	Real/ 2.5 Wo Ave	Real/ 2.45 Wo Ave	Real/ 2.4 Wo Ave	False/ 2.5 Wo Ave	False/ 2.45 Wo Ave	False/ 2.4 Wo Ave	EMPA Wo †
Tatahouine	3.5	4.2	2.9	3.0	3.0	3.2	3.2	3.2	3.6	3.6	3.6	1.5
Johnstown	1.8	1.3	2.0	2.1	2.0	1.9	2.0	1.9	1.7	1.7	1.6	2.8
EET 87503	7.5	8.1	7.9	7.7	7.5	7.7	7.6	7.5	8.0	7.9	7.8	8.1
Petersburg	9.9	10.1	10.2	10.1	10.0	10.1	10.0	10.0	10.1	10.1	10.0	9.4
Stannern	12.4	11.0	13.2	13.3	13.0	12.8	12.9	12.7	12.1	12.2	12.0	9.6
EETA 79005	9.9	9.1	9.4	9.6	9.6	9.7	9.8	9.8	9.2	9.3	9.4	10.3
LEW 87004	9.9	10.1	10.0	10.1	10.5	10.0	10.0	10.2	10.0	10.1	10.3	11
Juvinas	10.8	11.0	12.0	11.9	12.1	11.4	11.3	11.4	11.5	11.5	11.6	11.3
EET 87542	13.2	13.0	11.8	11.9	12.0	12.5	12.6	12.6	12.4	12.5	12.5	13
EET 90020	12.4	14.0	12.9	12.9	12.8	12.6	12.6	12.6	13.4	13.4	13.4	13
Pasamonte	12.4	12.0	12.6	12.4	12.6	12.5	12.4	12.5	12.3	12.3	12.3	13.7
PCA82502	13.2	14.0	13.5	13.3	13.6	13.3	13.3	13.4	13.7	13.7	13.8	14
Bouvante	14.8	14.0	13.3	13.3	13.0	14.1	14.1	13.9	13.6	13.7	13.5	14.0
All HEDs Mean	10.1 ±3.8	10.1 ±3.8	10.1 ±3.8	10.1 ±3.8	10.1 ±3.8	10.1 ±3.8	10.1 ±3.8	10.1 ±3.8	10.1 ±3.8	10.1 ±3.8	10.1 ±3.8	10.1 ±4.0
Eucrites Mean	11.9 ±1.7	11.8 ±1.8	11.9 ±1.5	11.9 ±1.5	11.9 ±1.4	11.9 ±1.5	11.9 ±1.5	11.9 ±1.5	11.9 ±1.6	11.9 ±1.6	11.9 ±1.6	11.9 ±1.8
Diogenites Mean	2.7 ±1.2	2.8 ±2.1	2.5 ±0.6	2.6 ±0.7	2.5 ±0.7	2.6 ±0.9	2.6 ±0.9	2.6 ±0.9	2.6 ±1.4	2.6 ±1.4	2.6 ±1.4	2.2 ±0.9

calibration that stands out as producing the most number of individual meteorite mol% results most consistent with the actual chemistry of the HEDs.

We can gain insight into the efficacy of our equations by comparing the derived molar contents of the Burbine sample to the set of 53 HEDs. As explained below, I found that the averages for the Burbine sample are largely in agreement with the larger 53 meteorite sample. This gives us confidence that the statistics for the larger sample are valid and representative of the HEDs on whole. As such, they will be used as a comparative data set to band parameters for V-type asteroids to look for similarities and differences between HEDs and V-types. Table 2 shows the band parameters of the set of 53 HEDs from the real, 2.5 μm edge combination. I found that the difference (Δmol%) of the mean Fs and Wo for the Burbine versus the full 53 HED sample sets are less than 0.3% (Table 3), except for FsII, which is 0.8%. Although this is well within RMS error, it is almost three times greater than Δmol% for FsI, which calls attention to the potential for the Band II calibration equation to give slightly less reliable derived mineralogy. The difference in Δmol% *between* the populations of howardites, eucrites and diogenites however are quite varied, with howardites exhibiting the least difference at 0.3 Δmol% for Fs ave (ΔFs ave), the diogenites exhibiting the greatest difference at 2.2 ΔFs ave, and the Eucrites in between at 1.1 ΔFs ave. The same is true for Wo ave. The differences in Δmol% between FsI, FsII, WoI, and WoII bands *within* the separate populations of HEDs, are more varied within the eucrites, but less varied for the howardites and diogenites. In other words, when it comes to the difference in the derived mineralogy between the Burbine sample and full set of 53 HEDs, the eucrites exhibit the greatest disparity between Bands I & II. This is true for both Fs and Wo.

3.1.4 Slopes

I examine the Band I slopes (BIS) because they are highly effected by the change from the real to the false blue edge. When using the false blue edge, the slope of the continuum fit is not the true BIS that is defined by the real blue edge (point (i)) and point (ii). As previously mentioned in Section 3.1.2, the result is an artificial increasing

of the BIS. This artificial increase of band slope will result in an artificial increase for the B1C determination.

The average slopes for the Burbine sample are 0.110 ± 0.079 and 0.221 ± 0.116 for the real and false blue edge, respectively, giving a 0.112 difference between them. Figure 8 shows how the slope is effected by changing blue edges, as a function of BIC and BIIC. The diogenites exhibit the greatest change, mostly due to Tatahouine. These will be compared to the asteroid slopes in § 3.3.3. The set of 53 HEDs show overall shallower slopes, but the change in slope is slightly greater. The means are 0.087 ±.066 and 0.218 ±.097, for the real and false blue edge, respectively, giving a 0.131 difference between them. With the Burbine sample, the false edge slopes are about double the real edge slopes. With the larger data set of 53 HEDs, it is somewhat more than double. Although the false edge slopes are about the same in both samples, the real edge slopes are quite a bit lower in the larger sample, which, it will be seen, exacerbates the slope discrepancy between the meteorites and the asteroids. The larger set also shows that diogenites show the greatest slope change, with the false edge mean slope almost seven times that of the real edge mean. In order to ascertain how serious the slope problem is, I will perform a frequency analysis of it and several other parameters in the next section.

3.1.5 Frequency Analysis

As stated above, I presented the calculated Fs and Wo molar contents of the 13 HEDs using all edge combinations in Tables 6 and 8. It is not surprising that the mean mol% is identical for all edge combinations, since that is the whole point of the calibration equations for the different edges. The red edge and blue edge "problem" happens when using the wrong equation on asteroid spectra can result in errors in determining mineralogy that are larger than the RMS error of the calibration equation itself. With such a limited set of available equations in the literature (Gaffey et al. 2002; Burbine et al. 2009, 2018), the use of equations that don't match the band parameter analysis is common. It is for this reason that I provide a set of calibration equations that are applicable to truncated or noisy asteroid spectra. This has the additional benefit of

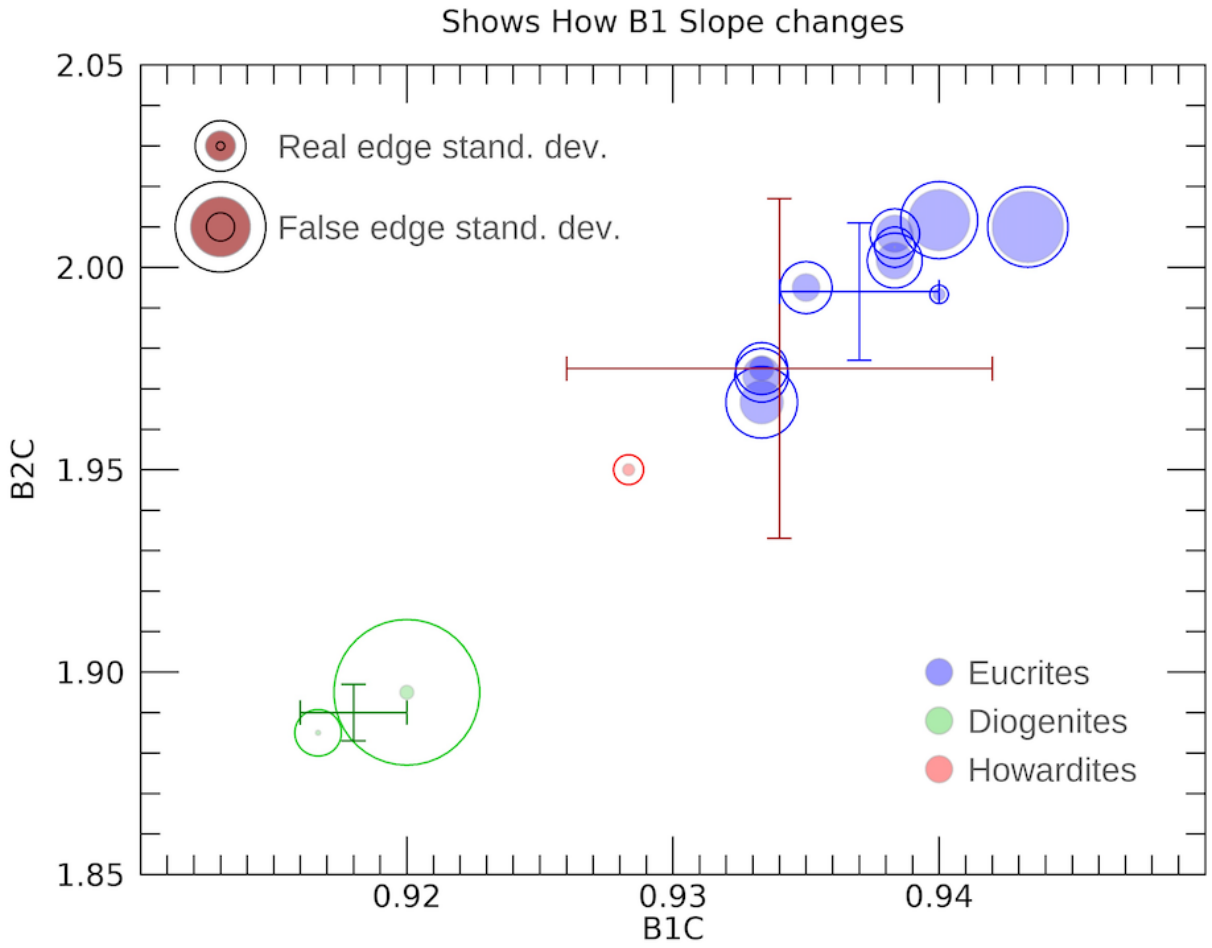

Figure 8: Burbine sample Band I slopes. Discs are real blue edge slope magnitudes between 0.003 and 0.265. Circles are false blue edge slopes between .069 and .542. Brown crosshair is standard deviation of the mean of all 13 HEDs. Blue and green crosshairs show the mean and standard deviation of the Eucrites and Diogenites, respectively. Brown discs show the mean of the slopes, and black circles show the $\pm$ standard deviation.

providing the first set of equations that allow for mineralogy determinations from NIR only data.

In order to ascertain how serious a problem the truncated spectra are, and provide recommendations on how others should use calibration equations, I evaluate the consequence of using equations from only one set of edges applied to band parameters measured with different red and blue edge choices. The standards I am comparing to are the real blue edge and 2.50 µm red edge equations. This is chosen as the standard because it is what is frequently used to establish calibrations from meteorite spectra, which always have full Band I and Band II wavelength coverage with good SNR. Specifically, I calculate the molar contents by using the *false* blue edge BICs in the *real* blue edge calibration equation, as well as by using the 2.4 and 2.45 µm BIICs into the 2.5 µm calibration equation. The point here is that if you are analyzing a truncated spectrum, then previous to this thesis there were no calibration equations for V-type asteroids except for the real blue edge and the 2.5 µm red edge ones. By comparing the derived mol% from using two different inputs into a single equation (Δmol%), we can quantify how often the edges result in mol% errors that are larger than a calibration's RMS error. This is shown in Figure 9, using the Burbine sample. For the blue edge, the mean difference between using the "false" BICs as opposed to the "real" BICs in the real blue edge equation is 3.76 Δmol%. Although this is still within the RMS of ±4.2 mol%, it is still concerning, as four of the meteorites fall above that line, and four are just barely below. In other words, ~30% of the Burbine sample meteorites are problematic in terms of the "blue edge problem." This discrepancy motivates the need for a false blue edge calibration equation. Notice that there is a slight trend for HEDs with smaller BICs, corresponding to the diogenites, to respond more strongly to Δmol%. This makes sense because the smaller the BIC, the closer the center is to the blue edge, and therefore the more likely to be altered when dividing by the slope of the straight-line continuum.

The red edge does not present the same level of concern. The 2.45 µm BIICs run through the 2.5 µm calibration equation yield a mean difference of only 0.42 Δmol%, and the 2.4 µm BIICs run through the 2.5 µm calibration equation yield a mean difference of 1.1 Δmol%. For this reason, this paper focuses its analysis more heavily on Band I than Band II. However, the red edge Δmol% appears to be a larger problem for

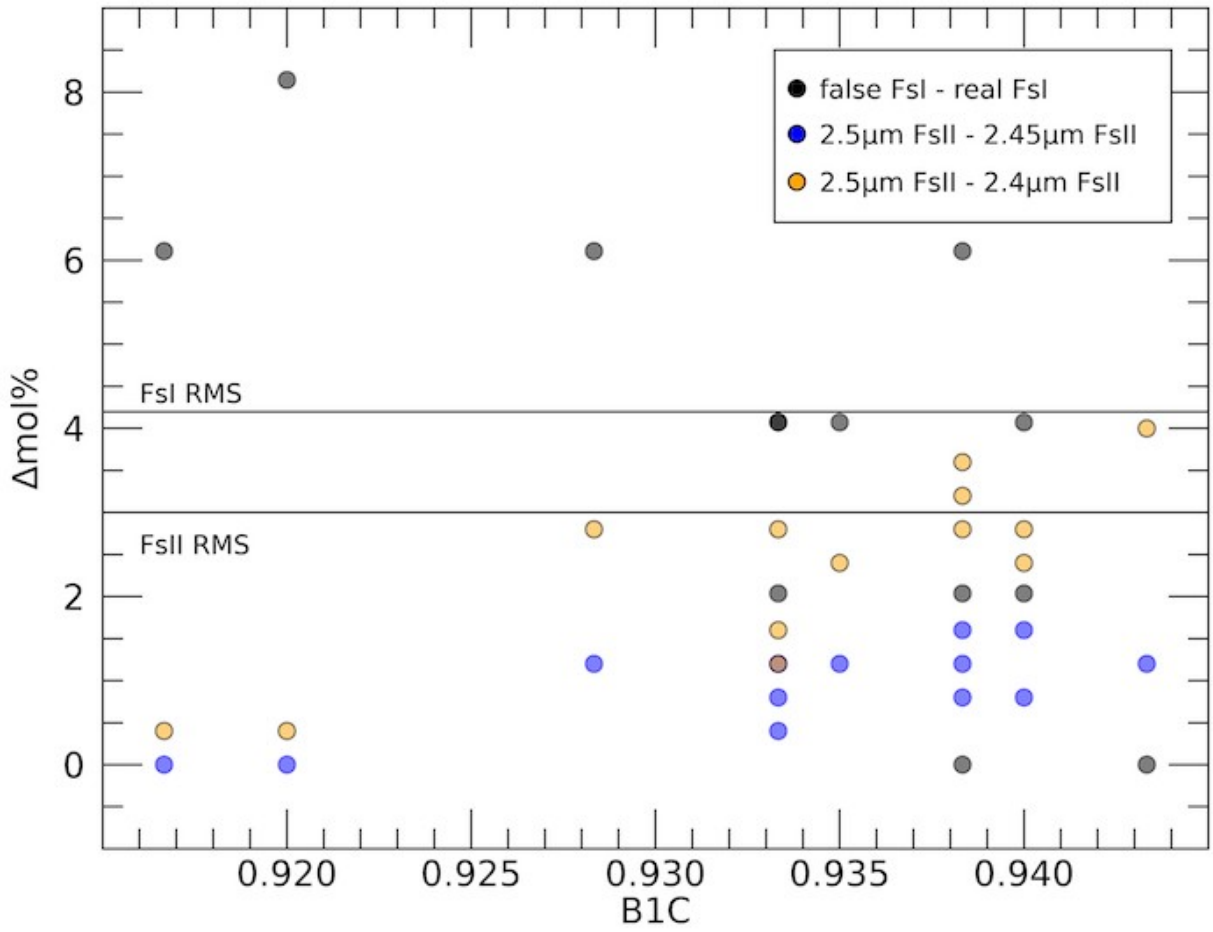

Figure 9: Frequency of cases for the Burbine sample in which the Δmol% for different edges, using the same equation, is greater than the respective RMS error.

larger BICs. The problem is also systematic in that the Δmol% is always positive. Even though Δmol% is below the level the uncertainty of the standard equations, these kinds of systematic errors are always a concern because they always behave the same way. For these reasons, and also in the case of incomplete or noisy asteroid spectra long-ward of 2.4 µm, it is important to provide the three Band II calibration equations, which supplement the work of Lindsay et al. (2016) and Sanchez et al. (2020). Having the complete set of calibration equations should yield greater accuracy for those who desire to derive molar contents with truncated V-type asteroid spectra in the future. It also offers the first set of calibration equations for IR only datasets. This is a valuable contribution because VNIR spectra require time on both visible and NIR telescopes, which adds time and cost to asteroid mineralogy research projects. Additionally, the observational conditions for data from two telescope are taken at different times, in different locations, and with different observing conditions, all of which can have an affect on the quality of the spectral data.

Figure 10 shows the frequency analysis for the set of 53 HEDs. For the blue edge, the mean difference is 4.9 Δmol%, which is well above the RMS error of ±4.2 mol% from the clean BIC equation, bolstering our previous conclusion from the Burbine sample frequency analysis above. 24 of the 53 meteorites, or 45%, have Δmol% values greater than the ±4.2 mol% RMS error, and another nine have a values of 4.1 Δmol%, which is just below that RMS error. Using the SNR50 BIIC equation RMS of ±5.5 has no effect on the frequency of the blue edge "problem." The 2.45 µm BIICs run through the 2.5 µm calibration equation yield a mean difference of only 1.2 Δmol%, and the 2.4 µm BIICs run through the 2.5 µm calibration equation yield a mean difference of 2.6 Δmol%. The Δmol% of 13 of the 53 HEDs, or 25%, are greater than the RMS error, and another eight lie just below the RMS value. These results from the larger sample set emphasize a greater need for multiple Band II calibration equations. The trend that edge choice is more important for larger BICs is very evident with this larger sample. This emphasizes that the "red edge problem" is more of a concern for eucrite-like mineralogies, which have higher BICs due to a higher amounts of Fe^{2+} and Ca^{2+}.

Burbine et al. (2009) used Band II minimums instead of centers in all of their analyses. The reason for that was because of the low signal-to-noise of the Band II absorption feature in asteroids, as well as the incompleteness of that feature in general,

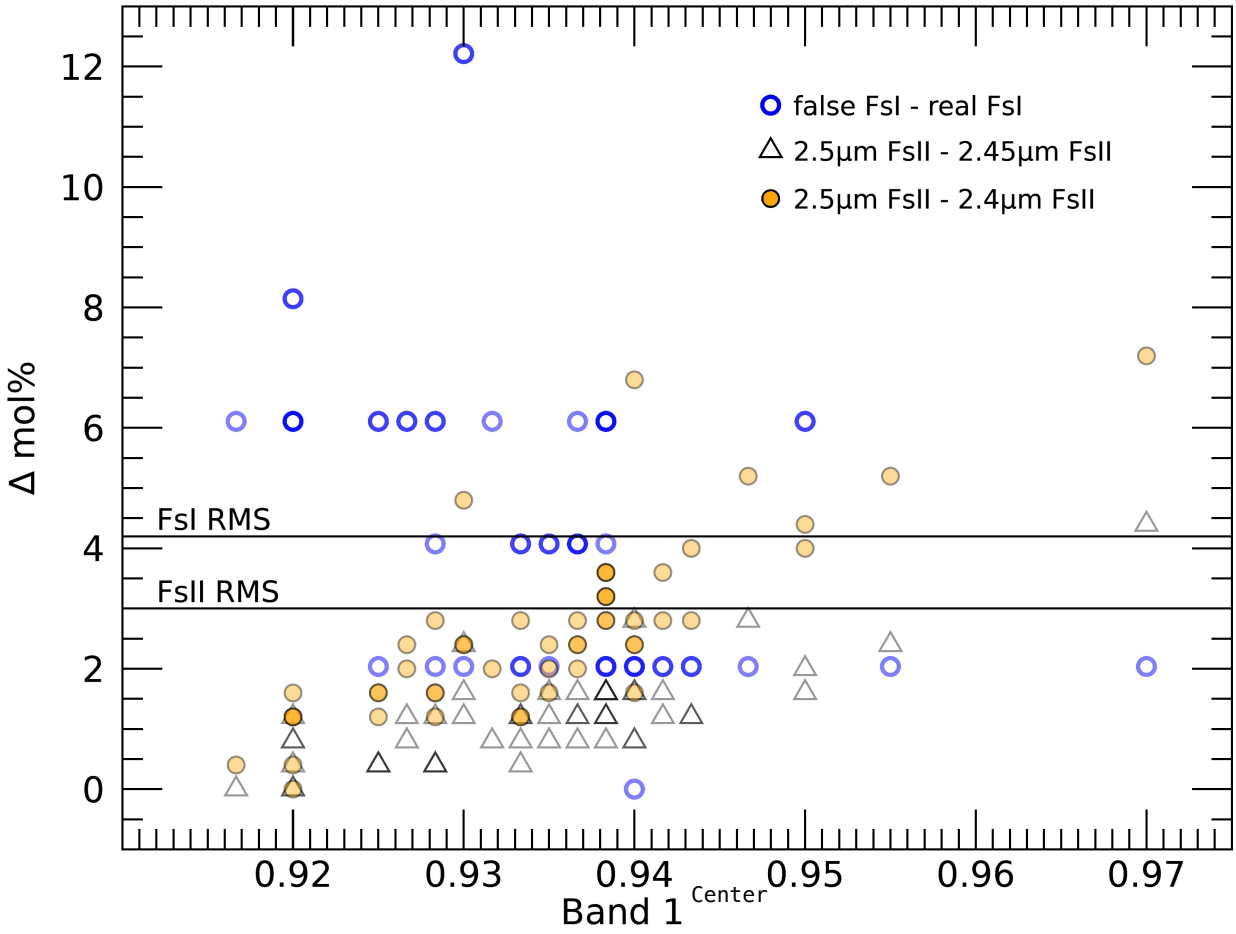

Figure 10: Frequency of cases for 53 HEDs in which the Δmol% for different edges, using the same equation, is greater than the respective RMS error.

since the reflectance values appear to increase beyond the range of the usable part of the spectrum (Burbine et al. 2009). Since using BIIMs might be used by another researcher, and in the interest of thoroughness, I repeat this frequency analysis using the Band I and II minimums in the real and 2.5 µm Band center equations (Figure 11). For the blue edge, the mean difference is -1.8 Δmol%. Here, the systematic one-sidedness of the Δmol% always being positive, as exhibited in the previous cases, is no longer adhered to. The Δmol% of 11 of the 53 HEDs, or 21%, are greater than the 4.2 mol% RMS error. Of those, 9 have negative values. For the red edge, the mean difference is 3.7 Δmol%, which is above the RMS, and only two meteorites exhibit a negative difference, so that the red edge "problem" is also systematically positive in this case. The Δmol% of 35 of the 53 HEDs, or 66%, are greater than the 3.0 mol% RMS error of the BIIC equation. Interestingly, Δmol% for this full 53 HED sample is worse for Band II, whereas the Burbine sample showed a greater problem for Band I. This presents good evidence that the Band II minimums shouldn't be used in a BIIC calibration equation when the centers are available. But it also works the other way: BIICs should not be used as inputs into BIIM calibration equations. In fact, it is best to use the calibration equations that best match the band analysis techniques that were used in determining the band parameters. Burbine et al. (2018) also makes this point.

Whereas the above analyses were performed using different band centers into the standard equations chosen, I also performed the converse test by using the same band centers in different equations. Figure 12 shows the derived mol% Fs when using SARA's BICs from the real blue edge in three different BIC calibration equations — mine, and two from Burbine et al. (2007 & 2018). EMPA mol% is also plotted for comparison. Notice how the two results from using Burbine's equations are both very close to each other, and also quite a bit lower than the EMPA and my results.

3.1.6 Modified Band I "centers"

There are two kinds of slope discrepancies in this thesis. One, the discrepancy between the slopes computed from the real blue edge as opposed to the false blue edge; and two, the discrepancy between the HED slopes and the V-type asteroid slopes (to be shown in § 3.3.3). This section focuses on the latter issue.

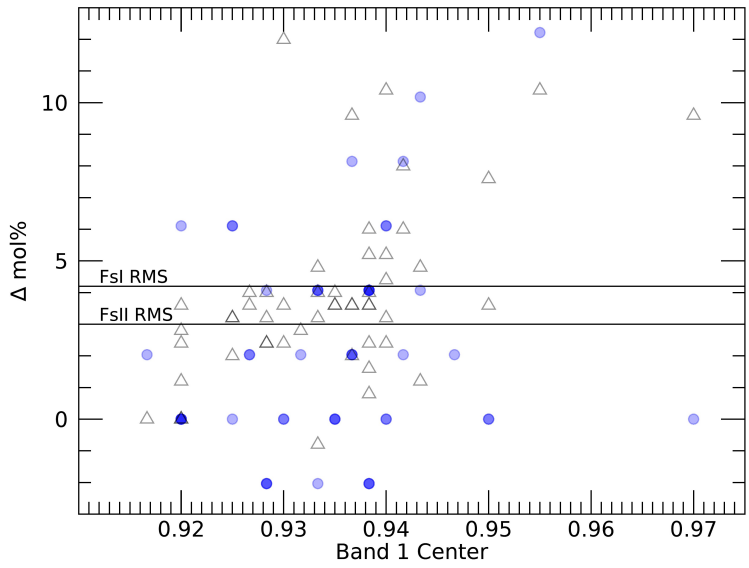

Figure 11: Frequency of cases for 53 HEDs, in which the Δmol% for using the Band *Minimums* in the Band *Center* equations, is greater than the respective RMS error. Circles are Band I. Triangles are Band II. The values of two meteorites lie below the confines of this figure.

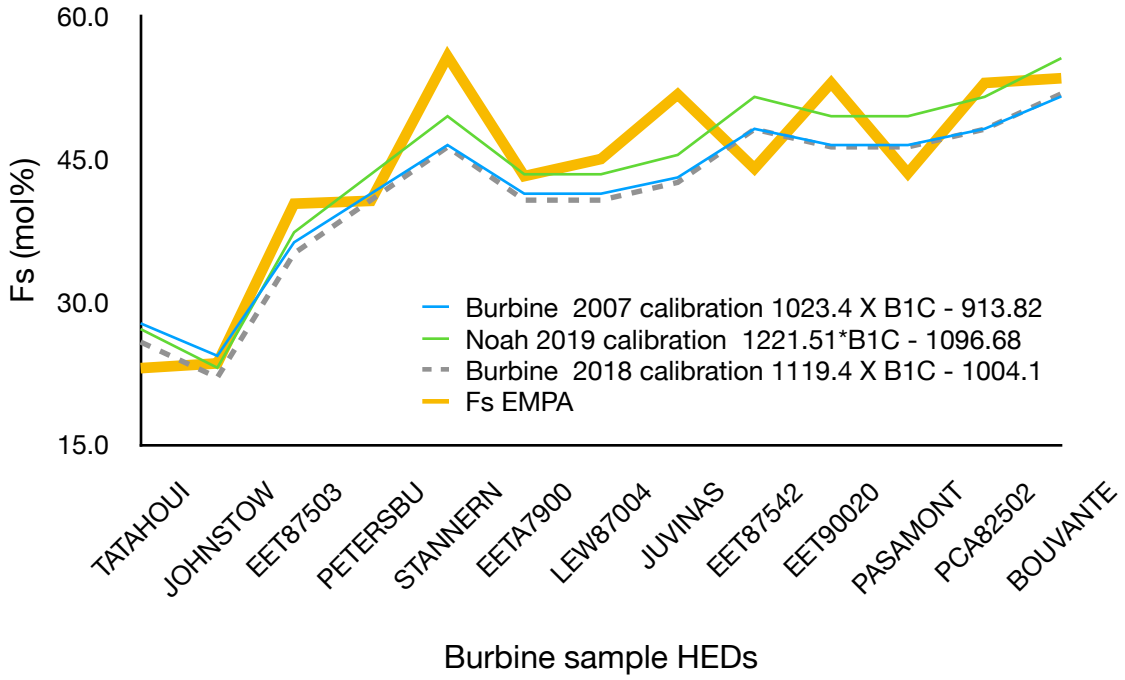

Figure 12: Derived mol% Fs from using a single set of BICs (SARA's real blue edge) in three different calibration equations. EMPA mol% Fs is also plotted.

Because the slope, shape and position of the Band I absorption feature is what causes the BIC to be different from the BIM, I investigated the possibility of adding an offset to the BIMs (using the clean spectral set). This gives a different way of computing a Band I "center" that takes account of slope, and has the additional benefit of potentially being applicable to infrared-only spectra that does not encompass the entirety of Band I. Figure 13 plots the Burbine sample BIC - BIM (called the "offset" in this thesis) against the real blue edge slope, to give

$$\text{Offset} = 0.033 \times \text{BI Slope} - 0.002 \tag{3}$$

Solving for BIC, I obtain

$$\text{BIC}_{\text{mod}}\ (\text{mol}\%)\ (\pm) = 0.033 \times \text{BI Slope} + \text{BIM}\ (\mu\text{m}) - 0.002 \tag{4}$$

where "mod" is short for modified. I then input these modified BICs into the BIC calibration equation and examine the derived molar abundances. The results are in excellent agreement with those from using the regular BICs, with the mean value identical. However, it will be seen in § 3.3.4 that this method, when applied to asteroids, yields remarkably higher Fs content than from using the BICs themselves. This is because the offset equations depend on the slope, and as will be discussed in § 3.3.3, the slopes for the asteroids are altogether much higher than the meteorite slopes. In an attempt to resolve this issue, still using the same offset idea, I added the asteroids to the offset plot, which is shown in Figure 14. This yields

$$\text{B1C}_{\text{mod\_2}} = 0.016 \times \text{B1 Slope} + \text{BIM}\ (\mu\text{m}) + 0.001 \tag{5}$$

There appears to be a curvature to the points in Figure 14, so I fit polynomials all the way through the 5th order. Although the higher orders have a higher R^2, they are not useful because of the severe downturn at the longer wavelengths. However, it will be seen later that the 2nd order polynomial yields results consistent with our other equations. This gives us a third possibility for calculating Band I "centers".

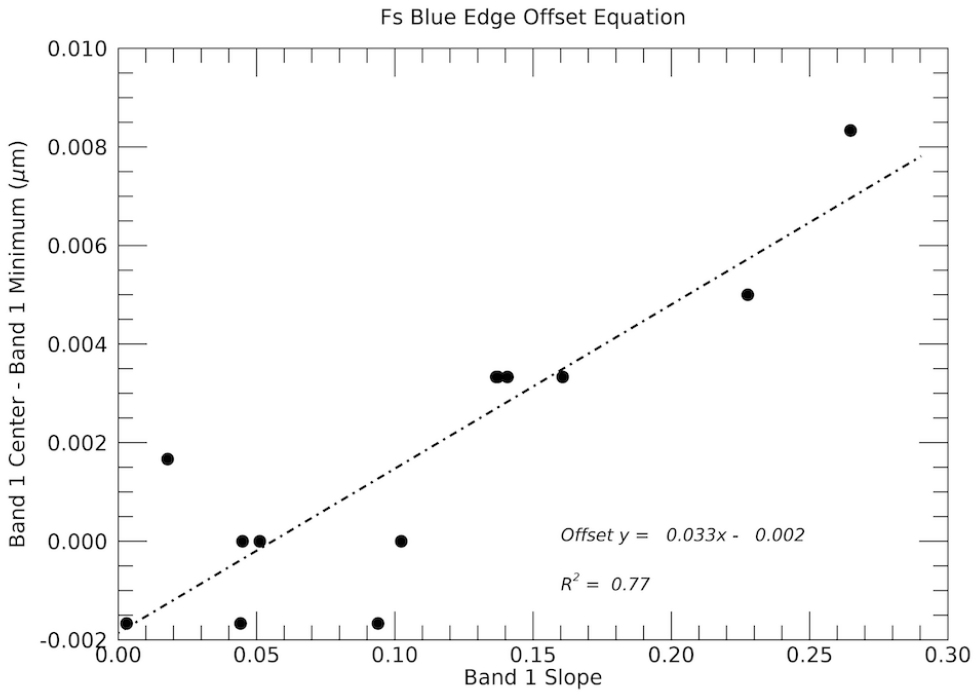

Figure 13: Fs Blue Edge Offset Equation from Burbine sample only

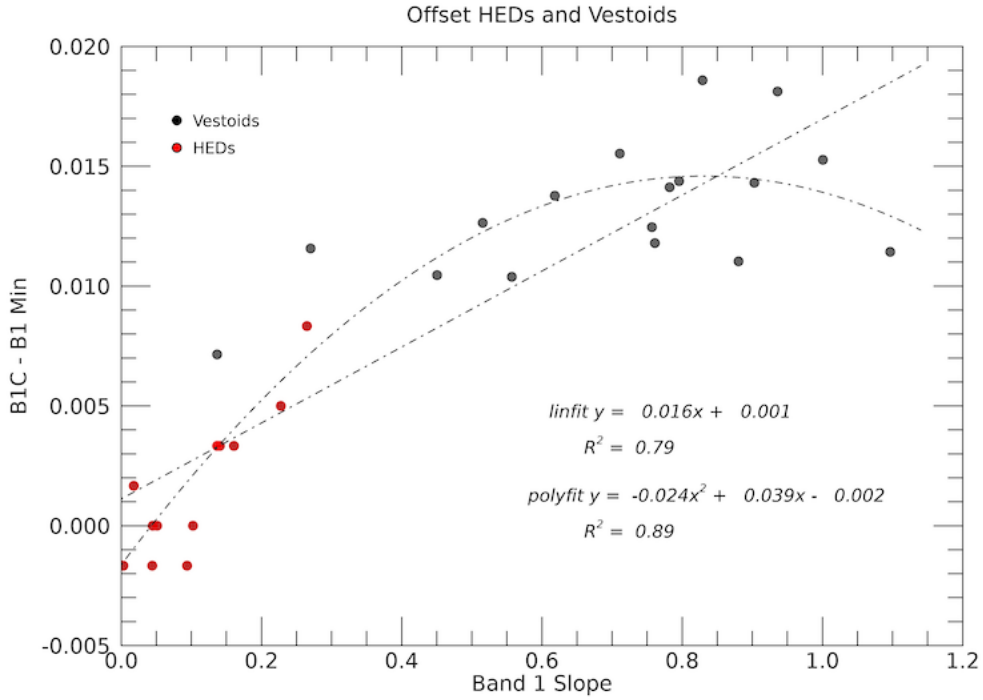

Figure 14: Blue Edge Offset Equations from HEDs and V-types.
V-type BICs are temperature corrected

$$B1C_{mod\_quad} = -0.024 \times BIS^2 + 0.039 \times BIS + BIM\ (\mu m) - 0.002 \quad (6)$$

The calculated mean mol% Fs for the Burbine sample using the $B1C_{mod\_2}$ and $B1C_{mod\_quad}$ centers are 43.7 and 43.3 mol%, respectively, which is well within the RMS error.

3.1.7 HED Zones

Howardites, eucrites and diogenites can be largely separated from each other by the amount of Fs and Wo in Pyroxenes, with the complication that eucrites, which result from magma flows, are divided into two subgroups — cumulate and non-cumulate (Stolper 1977, McSween et al. 2011). Non-cumulate eucrites are basaltic material from quickly-cooling magma (Klein & Hurlbut, 1977), and cumulates are gabbros, the solids that settle out of slower-cooling magma. Basaltic eucrites are more enriched in Fe (Mayne et al. 2009), and the cumulates have a higher diversity in Fe-content due to the fact that cumulates are the result of fractional crystallization. Non-cumulate eucrites have the greatest mol% Fs and Wo chemistries, diogenites have the least amount, and howardites have some amount in between. The composition of cumulate eucrites overlaps with that of both non-cumulate eucrites and howardites, introducing complexity into categorizing both meteorites and asteroids. Fs and Wo are dependent on the amount of Fe and Ca, respectively, which in turn effect the band centers of the absorption features that those elements correspond to. Therefore, we can plot BIC vs. BIIC to separate the meteorites into their three constituent subtype zones (Burbine et al. 2009; Moskovitz et al. 2010). Figure 15 plots those data points, for both the real (disks) and false (squares) blue edges, for the 53 HEDs, with polygons drawn around the points for each subtype for the real blue edge data points only. Whereas the diogenites are clearly in their own separate area, the cumulate eucrites and howardites overlap one another. The squares show how the band centers have shifted as a result of changing to the false blue edge cut-off. Figure 16 is similar to Figure 15, except it plots only the real blue edge points, and excludes the data point from an anomalous eucrite, MAC02522, because the average pyroxene calculated from its spectrum is not physically meaningful

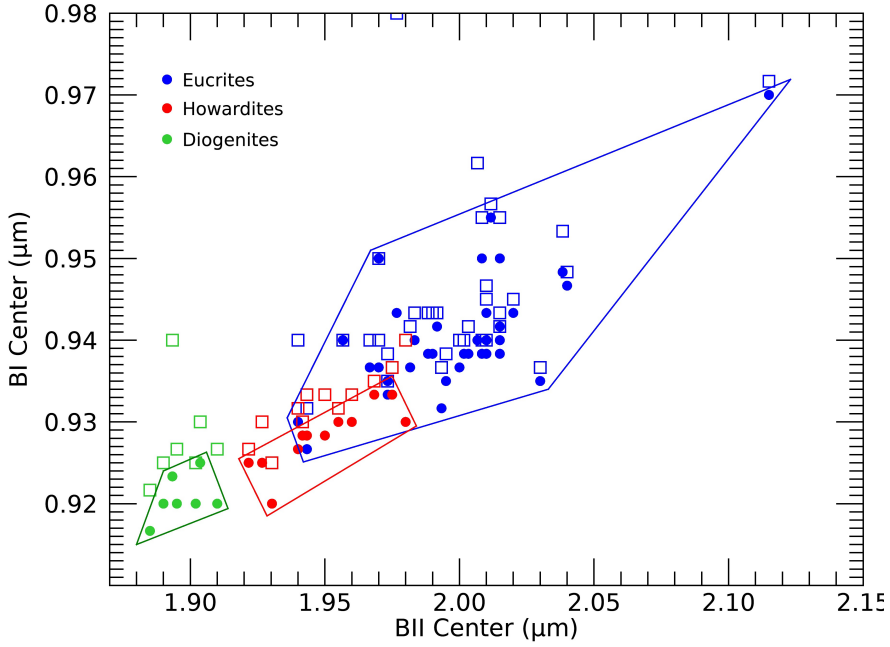

Figure 15: Subtype zones from 53 HEDs for the real, 2.5 µm edges. The discs are fro the real blue edge. Polygons are drawn around the boundaries of those data points to delineate the subtype zones. The squares are their data points from the false blue edge.

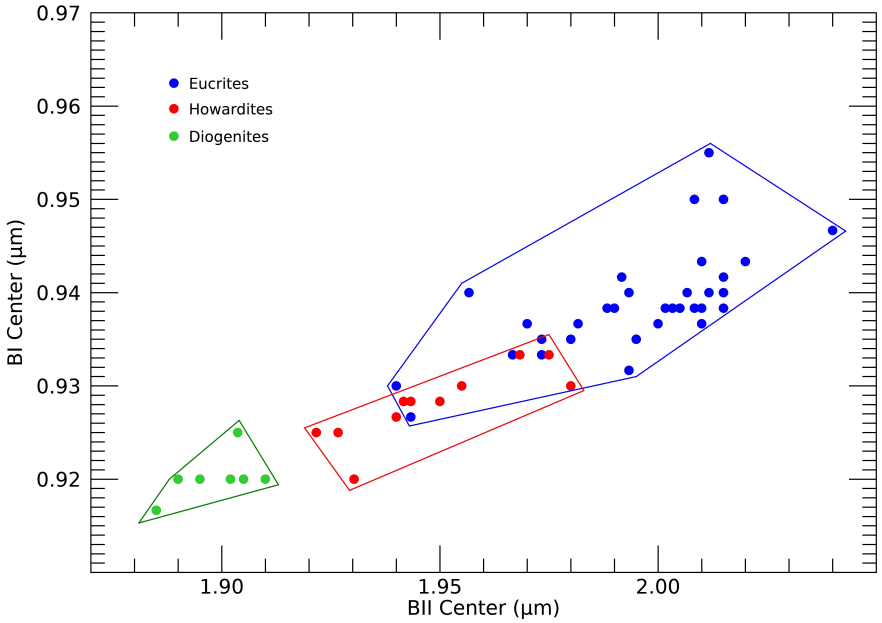

Figure 16: Subtype zones from 53 HED for the real, 2.5 µm edges. The anomalous eucrite in the top right corner from Figure 15a has been removed.

due to two compositionally disparate areas within its matrix that yield high and low Fs values compared with the average value (Maybe et al. 2015). Figure 17 shows the HED zones for the false blue edge. In § 3.3.5 we will over-plot the asteroidal band centers onto these subtype zones.

There is another way to separate out the subtypes — by plotting BIIC versus BAR (Moskovitz et al. 2010). Figure 18 performs this with the diameter of the bubble indicating Band I slope. As with the above method, the diogenites are firmly separated from the other two subtypes. Since there is such a large overlap in the average BAR ± 1-σ for each meteorite type, BAR alone does not help discriminate between the howardites, eucrites and diogenites. However, Moskovitz found that the BARs for his sample of inner Main Belt V-types were noticeably higher in value than the HEDs. In § 3.3.5 I will perform that same comparison. Plotting the slopes as circle diameters separates the subtypes from each other statistically, with the diogenites mean being half that of the eucrites.

We can also separate the HEDs from other meteorite types as Gaffey et al. (1993) did, by plotting BIC versus BAR, which I call the "Gaffey plot" in this paper. This plot differentiates the HEDs (Gaffey et al, 1993), ordinary chondrites (Gaffey et al, 1993), ureilites (Cloutis et al. 2010) and lodranites/acupulcoites (Burbine et al. 2010, Lucas et al. 2019) from each other. Figure 19 does this for the Burbine sample using the real, as well as false blue edges, and the 2.5 µm red edge. It also over-plots asteroid (4) Vesta from the band analysis results of three different sources: mine used in this paper, Gaffey et al.'s (1993), and a spectrum from the near-infrared wavelength range only, in order to quantify the results when the visible portion of an asteroid's spectrum is not obtainable. Interestingly, the false blue edge produces results for the HEDs most consistent with Gaffey. The conclusion should not be that a false blue edge produces mineralogical results most consistent with HEDs. Rather, a case is made that the boxes representing compositional meteorite types in the Gaffey plot were produced using methods that are different than the methods used by SARA; and that in order to properly differentiate meteorite types from one another by plotting BIC against BAR, a researcher needs to use the Gaffey-type plot that is commensurate with one's methods (see McClure and Lindsay 2020). This echoes the point made earlier about using calibration equations appropriate to one's band analysis techniques.

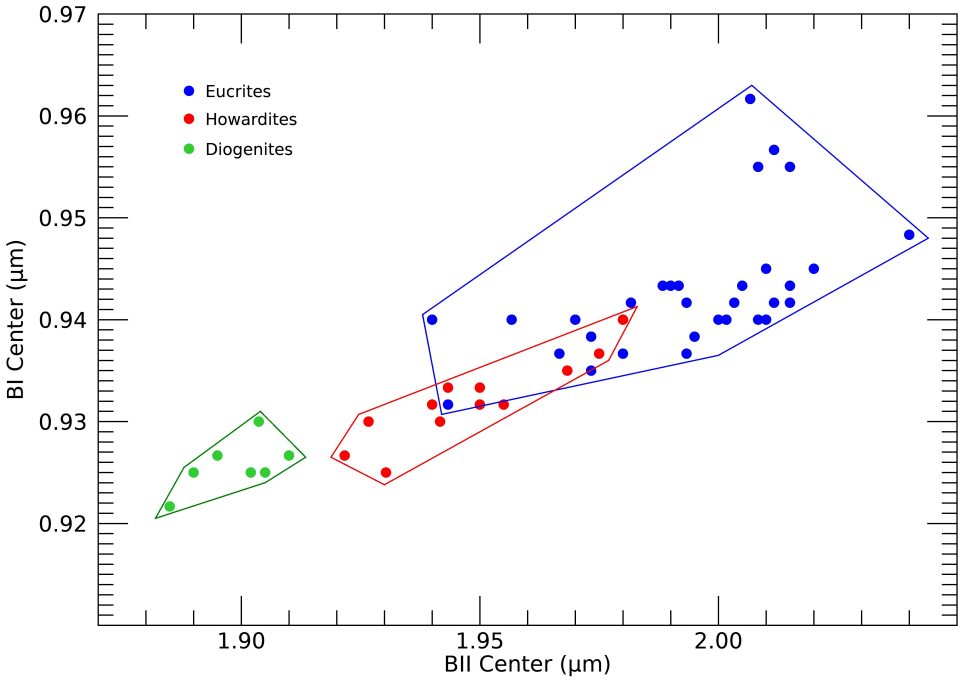

Figure 17: Subtype zones from 53 HED for the false, 2.5 µm edges. The anomalous eucrite in the top right corner from Figure 15a has been removed.

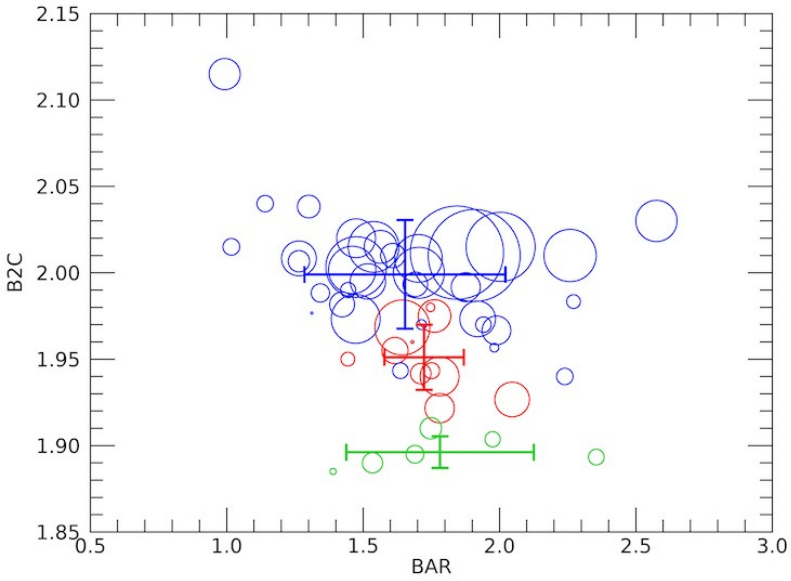

Figure 18: Subtypes for 53 HEDs for the real, 2.5 µm edges Blue is eucrites, red is howardites, green is diogenites. Means and standard deviation for each subtype is shown. Circle diameter is Band I Slope. Euc mean B1 slope = 0.091. How mean B1 slope = 0.071. Dio mean B1 slope = 0.046

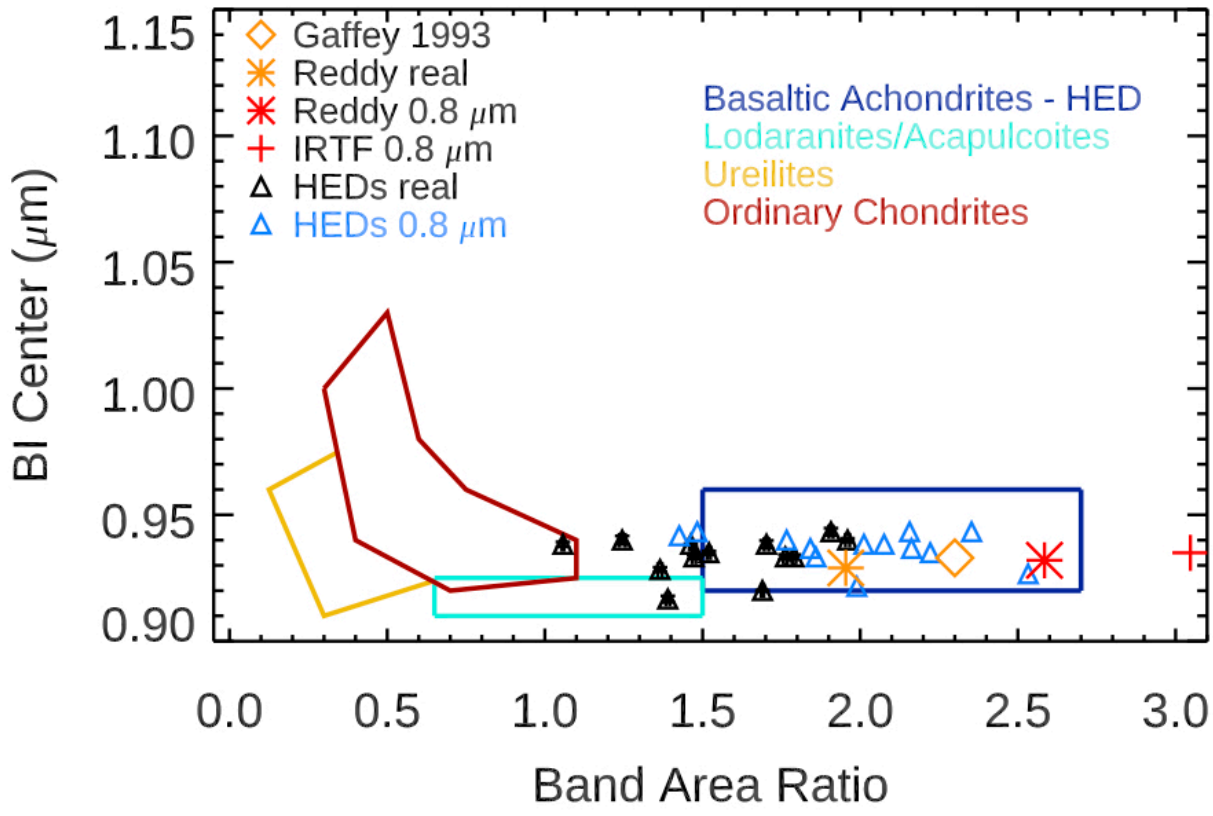

Figure 19: The Gaffey plot, showing four meteorite type zones. The HEDs were assigned to the dark blue rectangular zone in 1993 by Gaffey et al. Teh black triangles are the data points from the real blue edge, and the blue triangle are from the false blue edge. The remaining symbols are the band parameters from four different versions of asteroid (4) Vesta spectra.

To emphasize this point, I have redrawn the HED boundary in the Gaffey plot in Figure 20. It has shifted very noticeably to the left, overlapping much of Burbine's lodranites/acapulcoites zone, and touching the toe of the ordinary chondrite (OC) "boot." However, it is possible that if I were to analyze OCs using the same techniques used in this thesis, then the OC polygon would also shift to the left. Note that McClure & Lindsay (2020), who also used SARA, found that the OC boot shifted down, and also extended its left boundary to shorter wavelengths, but did not as a whole shift to the left in a manner likewise to my HED boundary in Figure 20. The vast majority of data points are contained within my HED boundary.

In Figure 21 I redraw the HED zone in the Gaffey plot for the false blue edge, still using the 2.5 µm red edge to calculate BAR.

Figure 22 shows the Gaffey plot for the 53 HED sample. Most of the data points are contained within my HED zone. However, there are several points at longer wavelengths which still remain in Burbine's HED zone, as well as four data points which lie above and/or to the left of my HED zone. Discounting MAC 02522, those three meteorites would only slightly change my HED boundary on the left-hand side. Since I did not perform an analysis on an SNR50 version of the 53 HED sample, I will use the boundary drawn from the Burbine sample, as it appears in Figure 21, for the remainder of this paper.

3.2 Meteorites (SNR50)

The difference in signal-to-noise for the spectra from meteorites (SNR~600) versus asteroids (SNR~50) is great. In the Introduction, I described the process by which I decreased the SNR of the Burbine sample meteorites to be comparable to asteroid spectra. In this section, I generate calibration equations from this noisy spectral set that give "realistic" (Sanchez et al. 2020) uncertainties in mineralogy for asteroids. We want to have uncertainties that are commensurate with the quality of spectra we have for

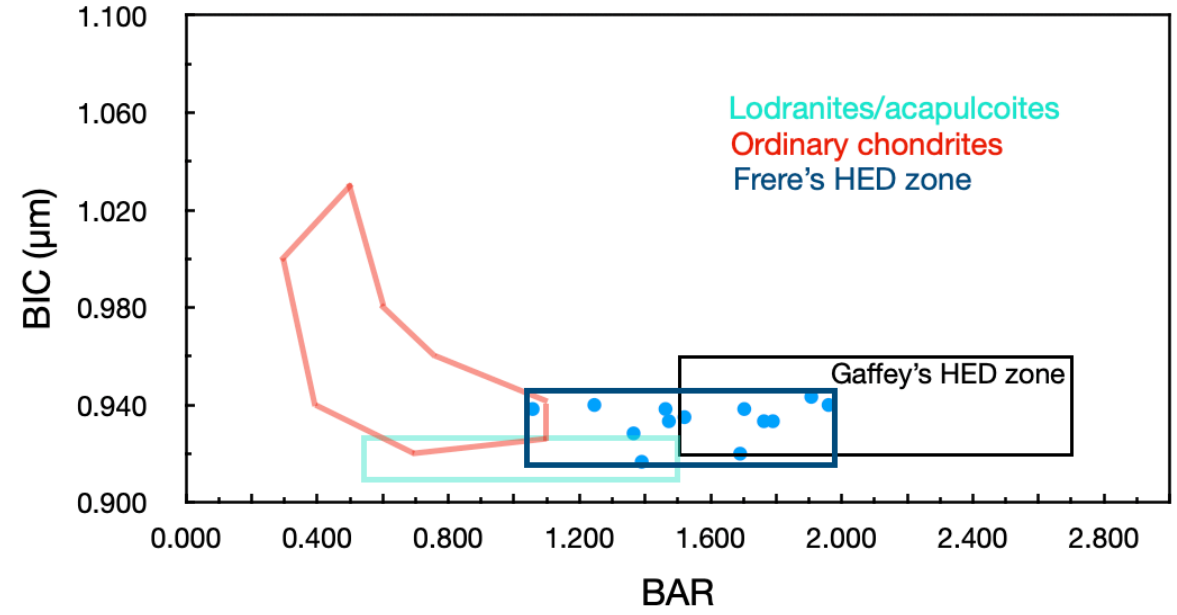

Figure 20: The Gaffey plot. The Burbine sample band parameters for the real, 2.5 µm edges are shown. A box was drawn around those points to signify the HED zone, as distinct from the HED zone (formerly called the basaltic achondrite (BA) zone) from Gaffey et al. (1993).

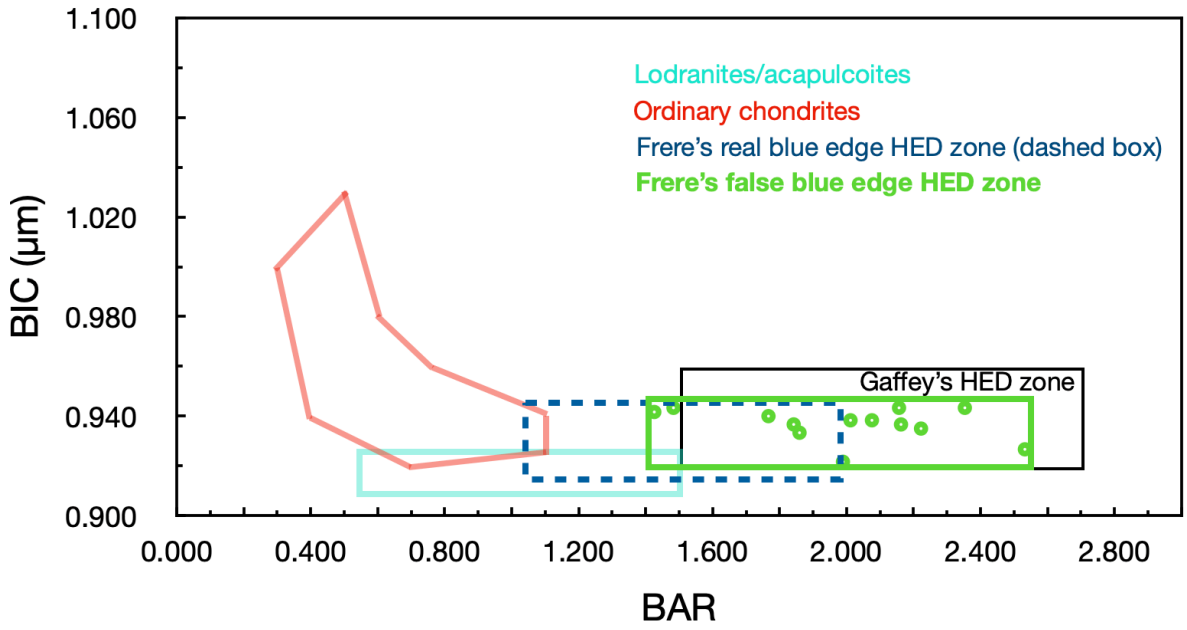

Figure 21: The Gaffey plot for the Burbine sample, using the false, 2.5 µm edges.

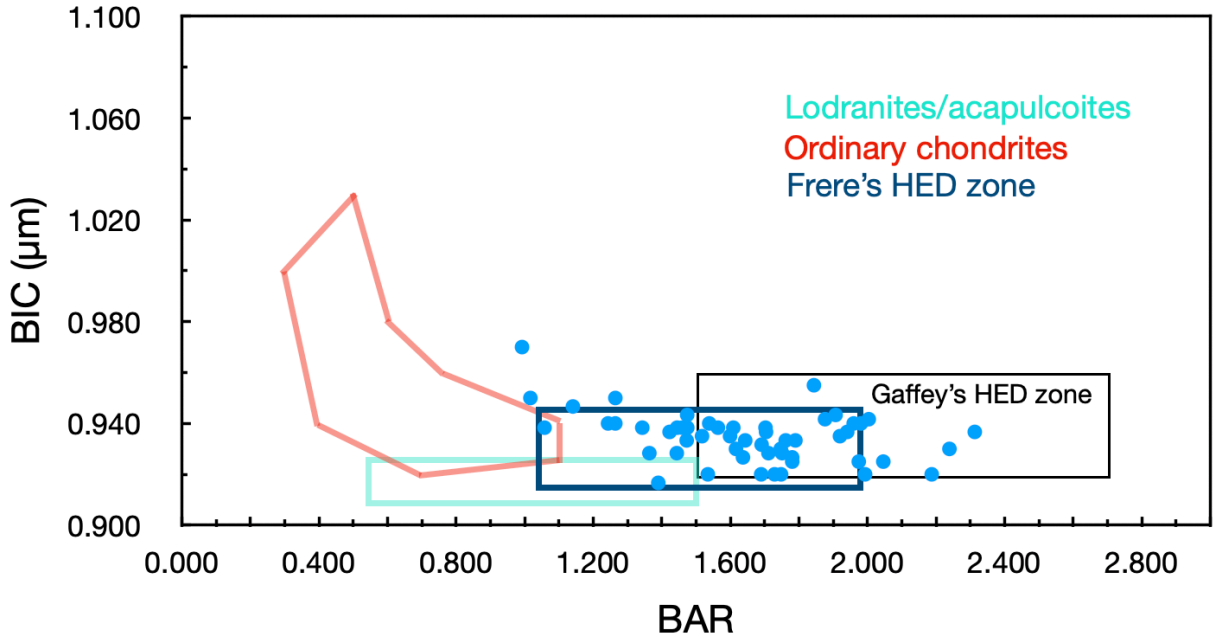

Figure 22: The Gaffey plot for the 53 HED sample, using the real, 2.5 µm edges.

asteroids. Using uncertainties from clean spectra gives the false impression that we can determine mineralogy of asteroids from asteroid spectra with the same precision we can with meteorite spectra. This is not true. It is, however, closer to true asteroid mineralogy uncertainties if we use calibration equations derived from asteroid-like SNR spectra. RMS error uncertainties are a function of band parameter analysis. Therefore we want to define our uncertainties using spectra with similar SNR characteristics to asteroids.

For example, when deriving asteroidal mineralogy, Band I might respond differently to the disparate SNR levels than Band II. I helped explore a similar study for S-type asteroids and ordinary chondrites (OCs), their meteorite analog (Sanchez et al., 2020). In that work, we published a paper entirely devoted to this subject for the S-type asteroids and OCs. The work done here is a parallel study to their research and will be submitted as a companion paper to Sanchez et al. (2020).

3.2.1 Calibration Equations

In order to mimic the low signal to noise ratio of earth-based asteroid spectra, I introduced noise into the Burbine sample (as described in the Methods section), and recalculated the calibration equations, shown in Table 9 and 7. Figure 23 shows the real and false Band I calibration equations for both the real and false blue edge. The coefficient value from the real blue edge SNR50 BIC equation lies mid-way between the coefficient from the same equation from the clean spectra, and the coefficient from Burbine et al.'s (2018) version. As expected, the SNR50 equations' R^2 and RMS increase in both cases. The RMS error for the real blue edge with SNR50 is 5.5 mol% Fs compared with an RMS error of 4.2 mol% Fs for the same equation using the clean spectra. The RMS error for the false blue edge with SNR50 is the highest of all the calibration equations in this thesis — 5.9 mol% Fs — compared with 4.5 mol% Fs for the same equation using the clean spectra. There is little to no change in the Wo RMS between the clean and SNR50 spectra..

Table 9: Calibration Equations from SNR50 HED Spectra

Blue Edge	Mol% Fs Equation	R^2	RMS	Mol% Wo Equation	R^2	RMS
Real	FsI = 1163.58×B1C - 1041.58	0.71	5.5	WoI = 501.01×B1C - 457.24	0.91	1.2
False	FsI = 1086.84×B1C - 973.33	0.67	5.9	WoI = 473.07×B1C - 432.63	0.87	1.4
Red Edge						
2.5 µm	FsII = 214.78×B2C - 379.81	0.82	4.3	WoII = 81.90×B2C - 151.42	0.82	1.6
2.45 µm	FsII = 218.60×B2C - 386.50	0.79	4.6	WoII = 84.19×B2C - 155.61	0.81	1.7
2.4 µm	FsII = 232.64×B2C - 412.49	0.81	4.4	WoII = 88.48×B2C - 163.44	0.81	1.7

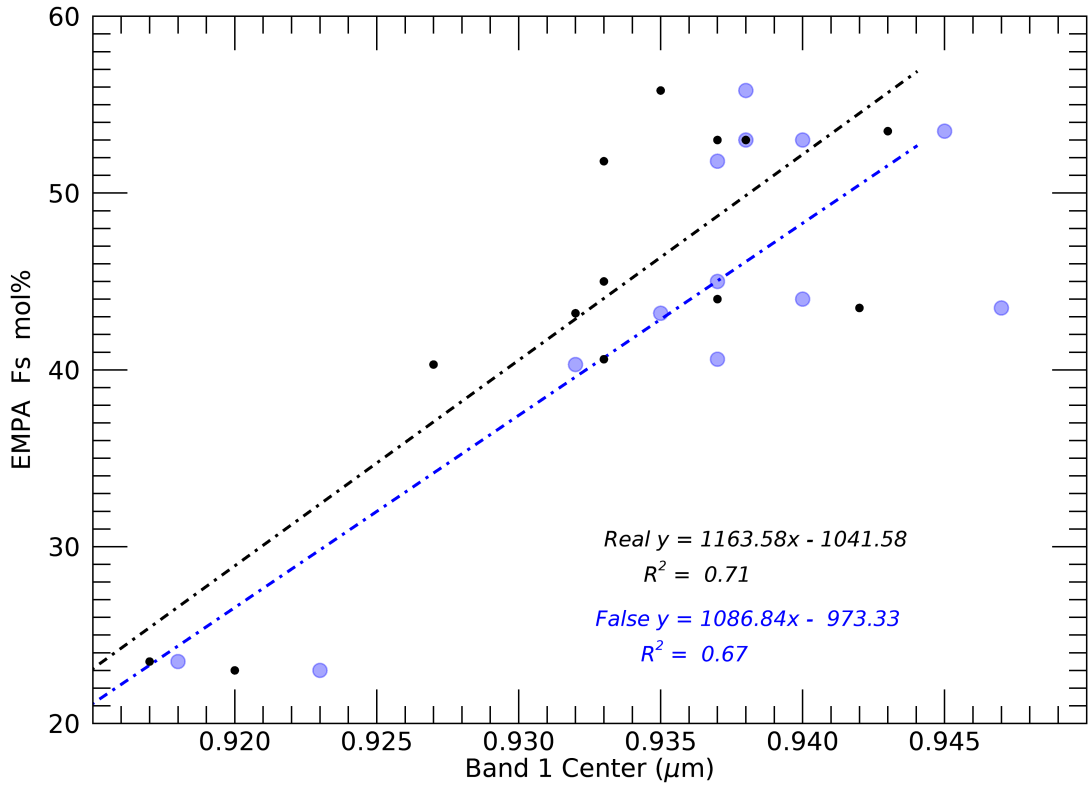

Figure 23: SNR50 Band I Calibration Equations

Figure 24 compares the BIM equation for both the real and false blue edges. Note that the clean HED spectra produce only one set of BIMs for both the real and false blue edge, but that the point-to-point scatter in the data in the noisy spectra results in two BIM equations, one for each blue edge. The linear fit for the real blue edge data points has the highest coefficient of any real blue edge equation (1436.7), because both diogenites' BIMs are at the longer 0.92 µm wavelength, resulting in a steeper linear fit, unlike other versions of the Band I "centers" in which they are separated along the x-axis. The RMS error for the real BIM equation with SNR50 is 5.5 mol% Fs, only slightly higher than the RMS error of 5.3 mol% Fs for the same equation using the clean spectra. However, the SNR50 false blue edge equation's RMS error is surprisingly smaller at 4.1 mol% Fs. Note also that this error is much smaller than the error from the SNR50 false blue edge BIC equation stated above (5.9 mol% Fs). This suggests that asteroidal mineralogy derived from the false blue edge SNR50 BIM calibration might give results better resembling the expected mineralogy of the HEDs. This will be tested in § 3.3.2. The Wo RMS decreased from 1.8 mol% from the clean BIM equation to 1.7 and 1.3 mol% for the SNR50 real, and false, blue edge equations, respectively.

Figure 25 compares four versions of BIC mol% Fs equations: three are presented in Table 5 — the two from Burbine et al. (2007 & 2009) and the one from the clean spectra from this thesis; and the SNR50 version. I present this figure as an overview of the BIC calibration equations calculated from a complete Band I wavelength range.

Figure 26 compares the clean and the SNR50 false blue edge equations using the BICs. This constitutes the most dramatic change, resulting from adding noise to the spectra, of all the equations, with the coefficient increasing by almost 400. This is a warning that incomplete and noisy spectra need to be treated carefully. This is in stark contrast to Figure 24, which shows a comparatively minor change when using the minimums instead of the centers. To elaborate on this point, in Figure 26, the same edge (the false blue edge) was used for BICs, while the noise level of the generating spectra was changed. Whereas in Figure 24, the noise level remains constant at SNR50 for BIMs, while the blue edge was changed. This suggests that, when using BIMs, it doesn't matter so much if you have truncated spectra if your spectra are noisy to begin with. However, it might be a consequence of how I determine the minimum. The BIC is found using smoothed reflectance data instead of a polynomial fit to the band. To test this, a

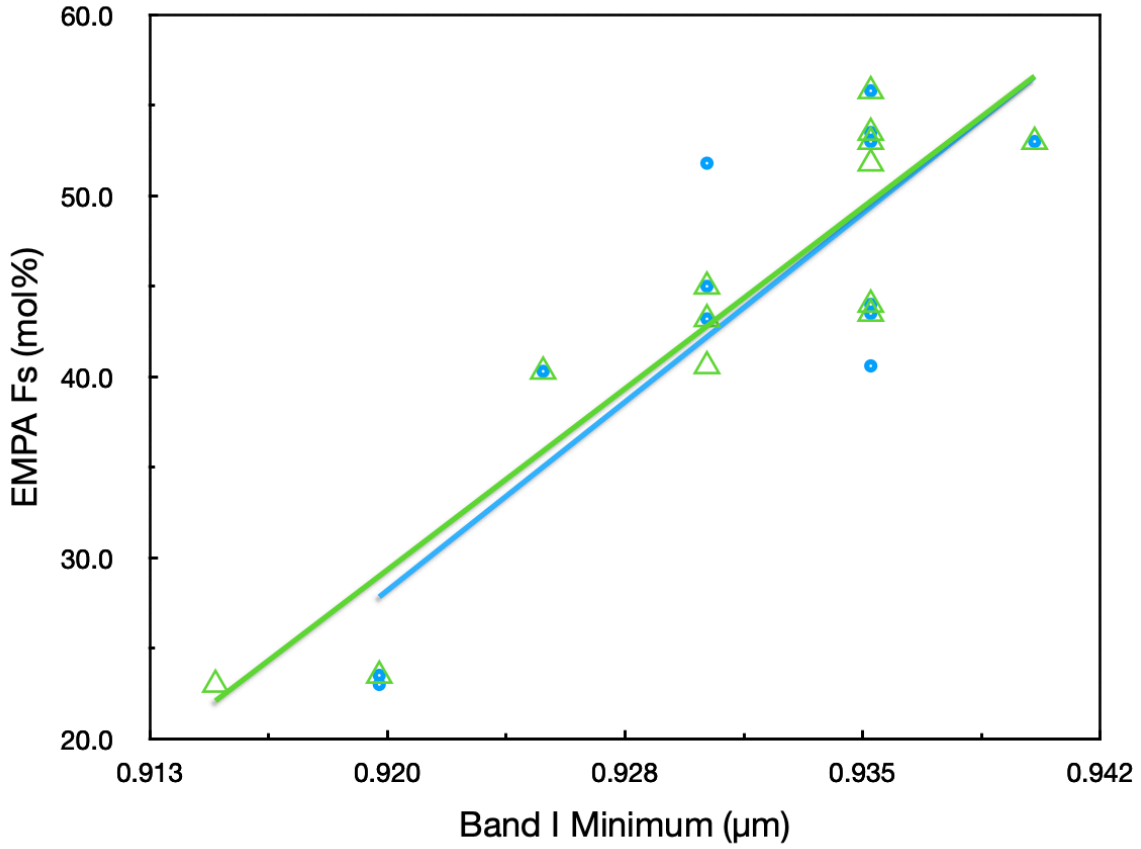

Figure 24: Band I Minimum Calibration Equation. The blue dots are from the real blue edge. The green triangles are from the false blue edge. Linear fits are shown with their corresponding color.

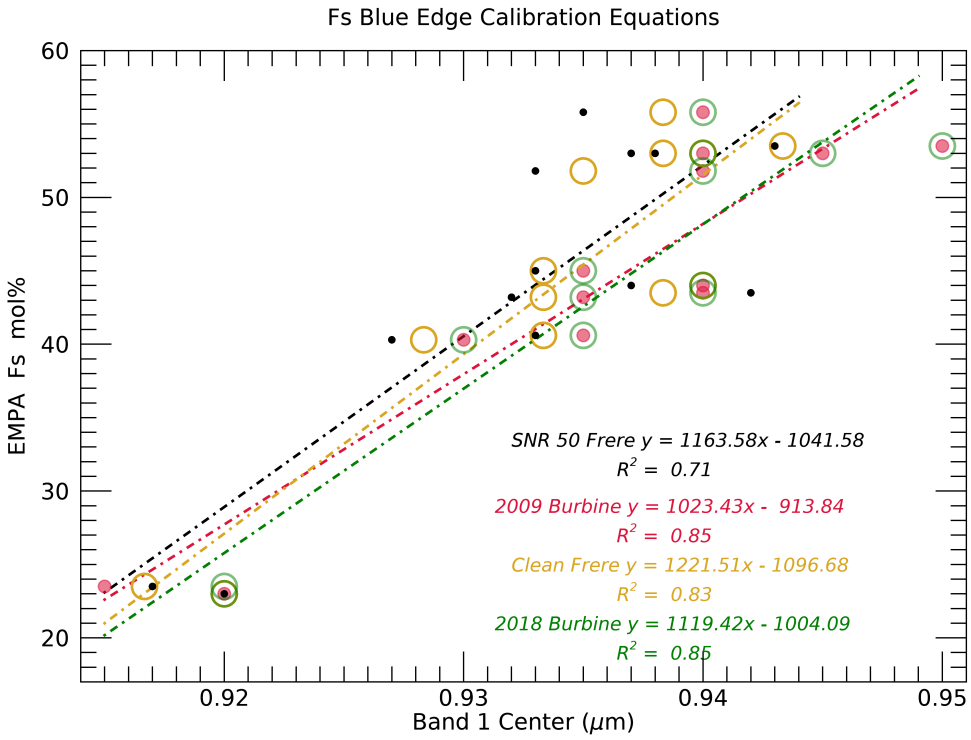

Figure 25: Four versions of BIC Calibration Equations

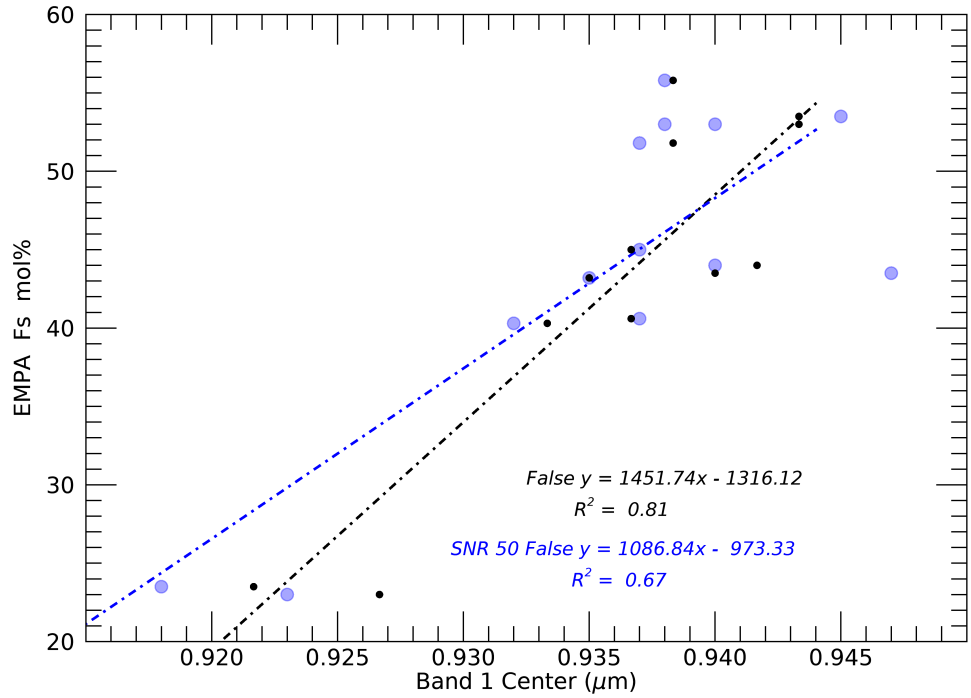

Figure 26: False Blue Edge Calibration Equations

polynomial could be fit to Band I, as is done for the BICs, before calculating the minimum. I did not perform this test.

Figure 27 shows the Band II equations. The slopes of the linear fits are shallower than their clean counterparts by roughly the same amount in each case. The diogenite centers cluster more in the same area, because Tatahouine's BIIC raised by 0.008 µm, as can be seen in Figure 27, which shows derived mol% Wo from both the clean and SNR50 calibration equations. As with the blue edge calibration equations, the RMS error increase by ~1.5 mol% Fs from approximately ± 3 mol% Fs for the clean spectra to approximately ± 4.5 mol% Fs for the SNR50 equations. Unlike the blue edge case, there is a noticeable increase, from approximately ± 1.3 to ± 1.7 in the RMS for Wo between the clean and SNR50 equations.

In going from the clean to the SNR50 Fs calibration equations, the R^2 decreased in value by 0.14 for both the blue edges, and by between 0.09 and 0.13 for the the red edges. In contrast, the Wo R^2 decreased in value by no more than 0.04 for the blue edges, and by between 0.07 and 0.09 for the the red edges.

3.2.2 Comparing Calibration Equations

The Burbine sample HEDs have been arranged in the tables in this thesis from lowest to highest mol% Wo, which follows Burbine et al's (2018) presentation of the same sample. This arrangement is clear in the green line in Figure 28, but notice how the blue line (SNR50 mol% Wo) no longer follows this trend. This is an example of how using noisy spectra can obfuscate band parameters and the resulting mineralogy. Overall, however, both the clean and SNR50 equations are in agreement. The SNR50 equations are the most appropriate equations to use when attempting to retrieve mineralogical information from the reflectance spectra of asteroids. This is because they best represent the uncertainty in determined composition from spectra with signal-to-noise characteristics most common for asteroid observations.

Figure 29 shows the Fs ave from each edge combination, and compares that to Burbine et al. (2018) results and the EMPA values. The main thing to notice here is

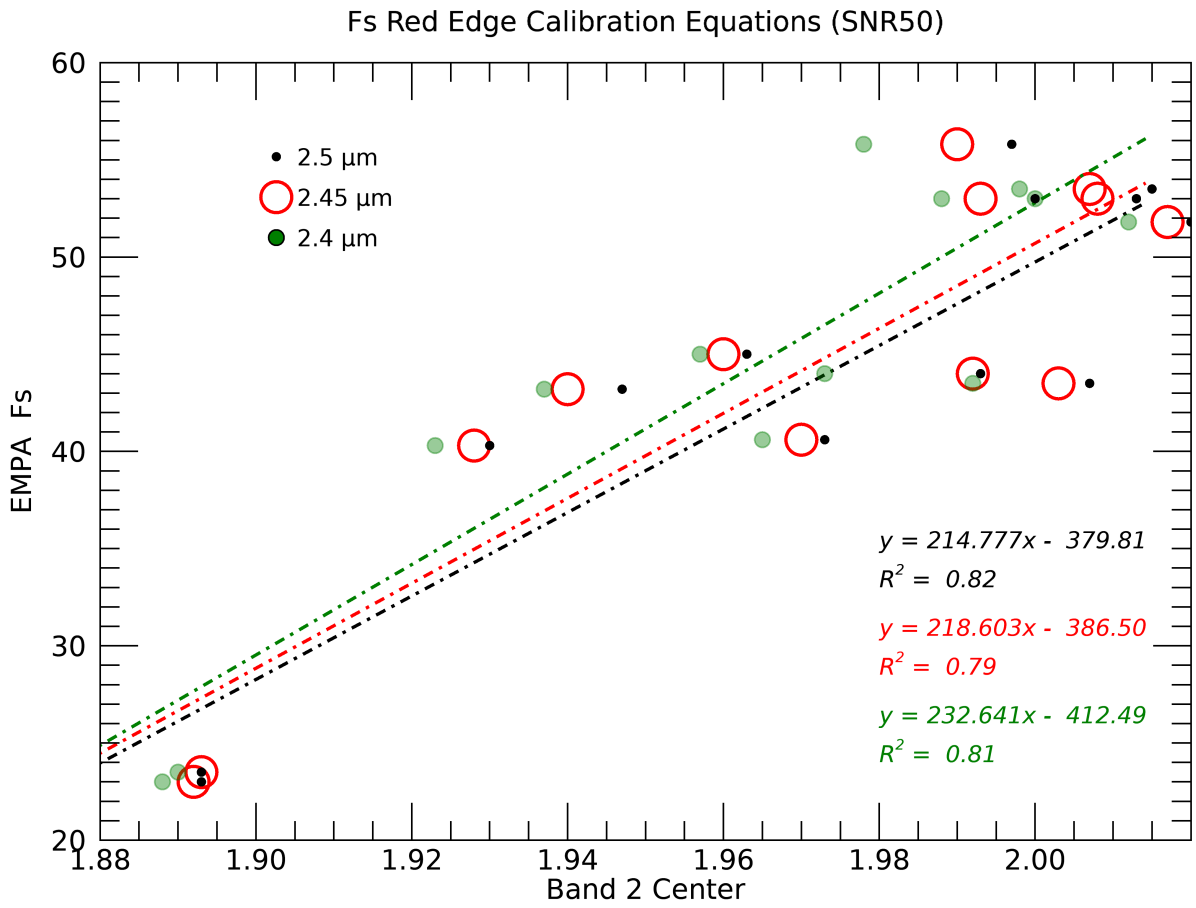

Figure 27: SNR50 Band II Calibration Equations

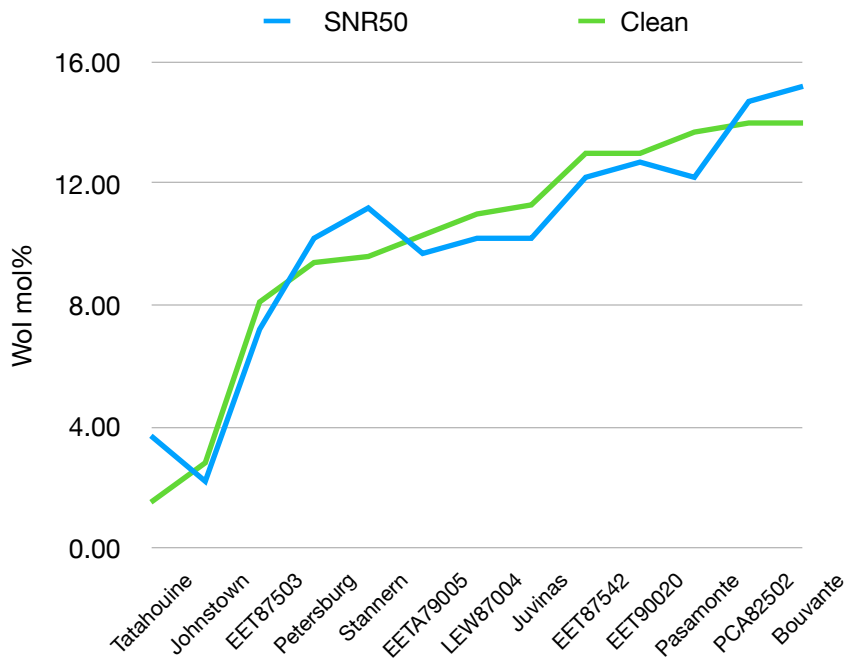

Figure 28: Derived mol% WoI from using both clean and SNR50 calibration equations with their corresponding BICs.

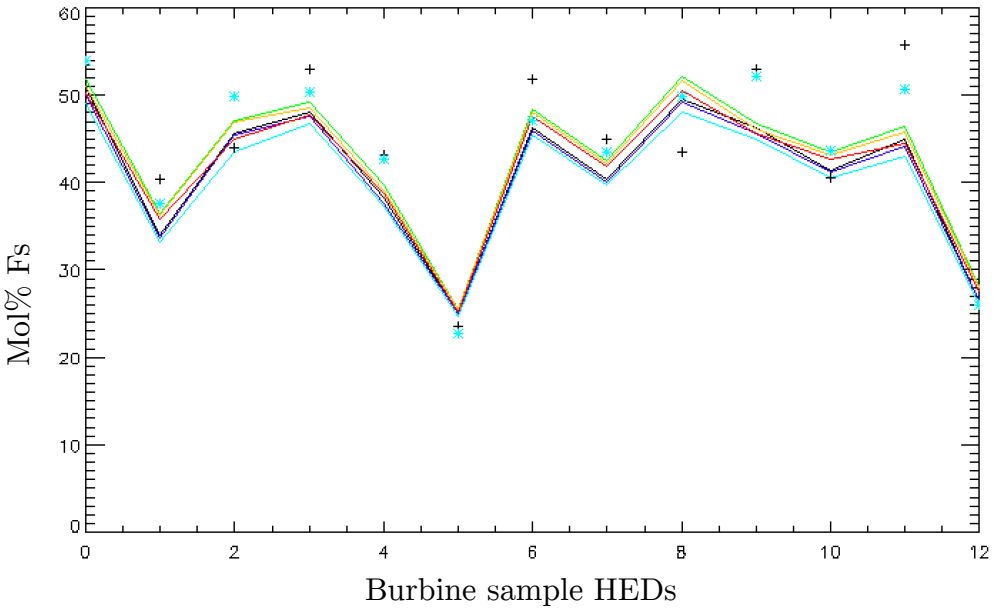

Figure 29: Burbine sample SNR50 Fs ave from all six edge combinations. The asterisk is Burbine et al. (2018) results, and the plusses are the EMPA Fs values.

that the differences between the different edges are less than the differences between SARA's results and both Burbine's and the EMPA results. The small differences between all the SARA-based mineral determinations indicates that all equations reliably return similar mineralogy. Each combination of edge choices have only small differences in RMS errors, with the false blue edge equations being, in general, the least precise. The increase in uncertainty in mineral composition, however, is greatly offset by the ability to retrieve composition from IR-only data sets. IR-only observations can be made with a single telescope on the same night. This limits any telescope+instrument differences and time-dependencies, such as different atmospheric conditions, phase angles, and temperature differences that would exist for data sets reliant on visible and infrared spectra. My recommendation is that the researcher uses the equation from this thesis that best matches the availability to the spectral data that was obtained.

Figure 30 shows the same SNR50 results, but compares it with the clean results. The clean spectra give two groupings of results (dashed lines): one for the real blue edge, with the red edges making very little difference; and a higher up set for the false blue edge, again with the red edges making very little difference. Adding noise to the source spectra has somewhat preserved the gap between the real and false blue edge results, but blurred the red edge gaps. It is important to realize though, that while each individual meteorite's mol% Fs ave deviates more or less from the EMPA values, yet the means from all edge combinations still equal the EMPA mean of 43.9 mol%.

3.2.3 Slopes & BAR

Going from the clean to SNR50 spectral sets, there was a negligible change to the real Band I slopes, with only Petersburg exhibiting a change greater than 0.01, and a mean shift of -0.004. The mean false BIS increased from 0.221 to 0.228 when going from the clean to the SNR50 spectral sets, exhibiting only a 0.007 change. This is not unexpected, as points (i) and (iv) (see the Methods section for an explanation of how they are calculated) are defined the same way for both the clean and SNR50 spectral sets. Compare this with the mean change in BIS when going from the real to the false

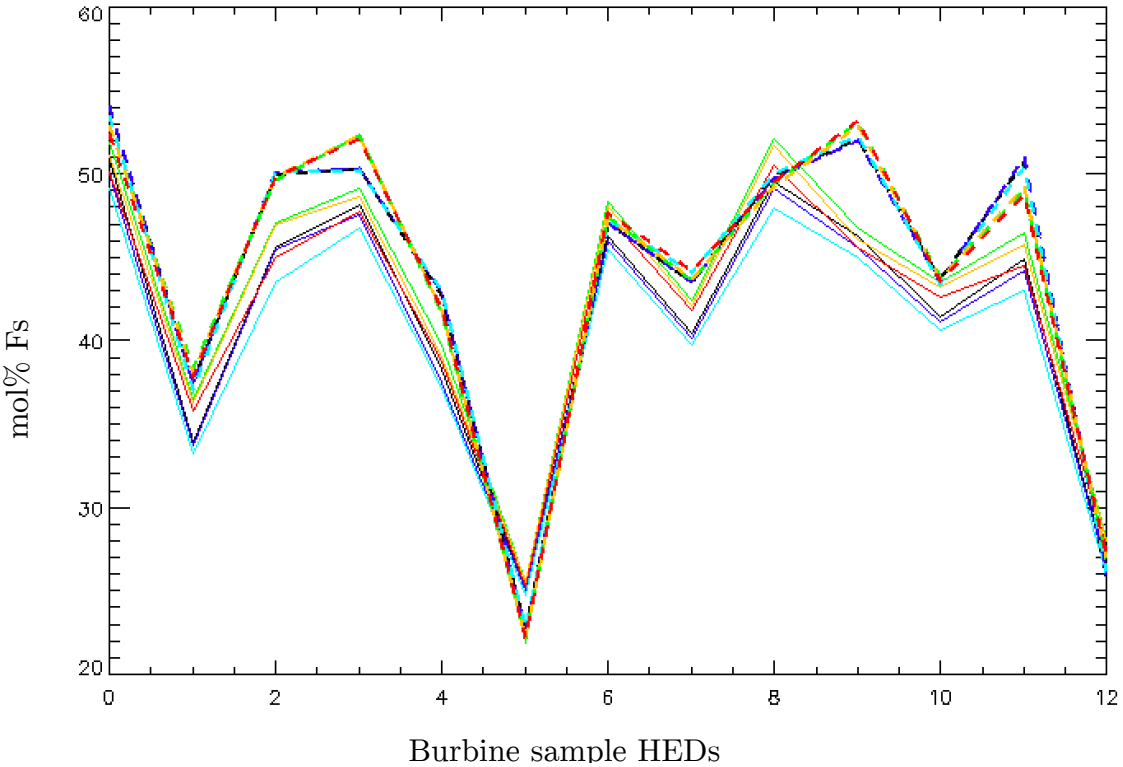

Figure 30: Comparing Burbine sample clean with SNR50 Fs ave from all six edge combinations. The solid lines are SNR50, while the dashed lines are from the clean spectra and equations.

blue edge of 0.112. This change is expected due to point (i) being defined at a different part of the spectrum for the false blue edge than it is for the real blue edge.

The BAR went from 1.991 ± 0.317 to 2.002 ± 0.322 for a change of 0.011, a negligible change. Compare this to a shift of 0.428 from the real to the false mean BAR. The take-away is that the blue edge choice has a much greater effect on the slopes than the noise-level of the spectra.

3.2.4 Frequency Analysis

Here, I repeat the frequency analysis, presented in § 3.1.5, for the decreased SNR spectra to see if the increase in uncertainty leads to an increase in how frequently the choice of edges leads to errors in mineralogy larger than those inherent to the calibration equation. The mean Δmol% for the Burbine sample for the case of using the false blue edge SNR50 BICs in the real blue edge SNR50 BIC equation is 3.6 Δmol%. This is almost identical to the clean spectral set's mean of 3.8 Δmol%. These values are very close to the RMS error from the clean BIC equation of ±4.2 mol%. Figure 31 shows the Δmol% for both Band I and II. In both the clean and SNR50 cases, four of the 13 HEDs from the Burbine sample, or 31%, are above this RMS value, and thus problematic in terms of the "blue edge problem." The RMS error for the SNR50 BIC equation is higher at ±5.5 mol%, and the Δmol% from only two meteorites surpass that value, which is ~15% of the meteorites.

The mean Burbine sample Δmol% for using the 2.4 µm BIICs in the 2.5 µm BIIC equation is 2.4 Δmol%, more than double the 1.1 Δmol% from the clean spectra. This suggests that mineralogy derived from a truncated Band II is more susceptible to spectral noise than that derived from a truncated Band I. The RMS for the clean 2.5 µm BIIC equation is ±3.0 mol%, and 31% of the HEDs lie above this line. The RMS for the SNR50 2.5 µm BIIC equation is ±4.3 mol%, and the Δmol% of one HED equals this value.

Overall the use of reduced SNR calibration equations did not change the frequency of how often the edge choices are the largest source of uncertainty. The errors

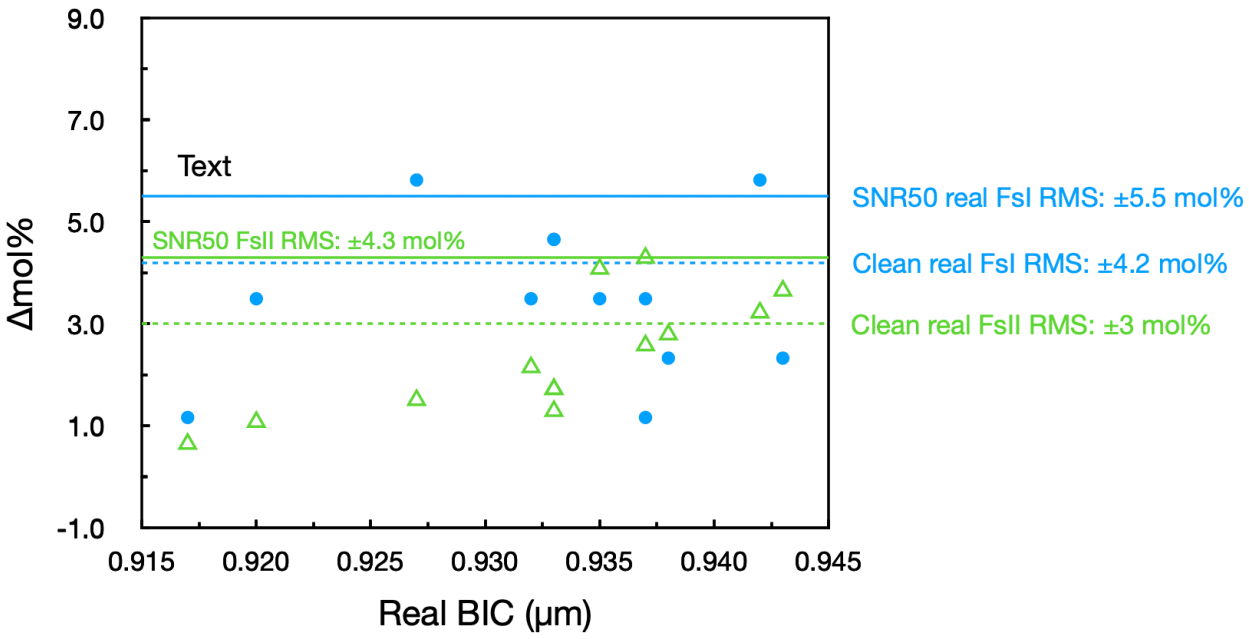

Figure 31: Frequency of cases for the Burbine sample in which the Δmol% for using the false BICs in the real BIC equation (blue dots), and in which the Δmol% for using the false BIICs in the real BIIC equation (green triangles) is greater than the respective RMS error. RMS errors are shown for both the clean and the SNR50 equations.

in determined mol% remain systematic in overestimating molar contents, with worse errors for larger Fe^{2+} content for the Band II equations. Therefore, more caution must be applied to the non-cumulate Eucrites when only incomplete and noisy spectra in the Band II area are available.

3.2.5 HED Zones

I did not perform a band parameter analysis on an SNR50 version of the larger set of 53 HEDs. Therefore I analyze only the Burbine sample here.

Figure 32, analogous to Figure 16, shows the band centers plotted against each other for both the clean and SNR50 spectral sets. The SNR50 (green triangles) data points show slightly more scatter than the clean (blue dots) data points, but overall they align quite well. Thus I conclude that adding noise to the Burbine sample spectra did not alter the make-up of the howardite, diogenite or eucrite zones by using this method. Figure 33, similar to Figure 17, but without the slopes, shows the BIICs plotted against the BARs for the real, 2.5 µm edge combination for the Burbine sample, for both the clean and SNR50 spectral sets. As in the above case, the data points are, on the whole, unaffected by adding noise to the spectra. Figure 34, analogous to Figure 21, shows that adding noise to the spectra have no bearing on the placement of the Burbine sample within my HED boundary in the Gaffey plot. Thus, I can overlay the V-type band parameters onto the Gaffey plot containing the HED boundary that was drawn using the clean HED spectra. There is no need to redraw the HED zone for the noisy spectral set.

3.3 Asteroids

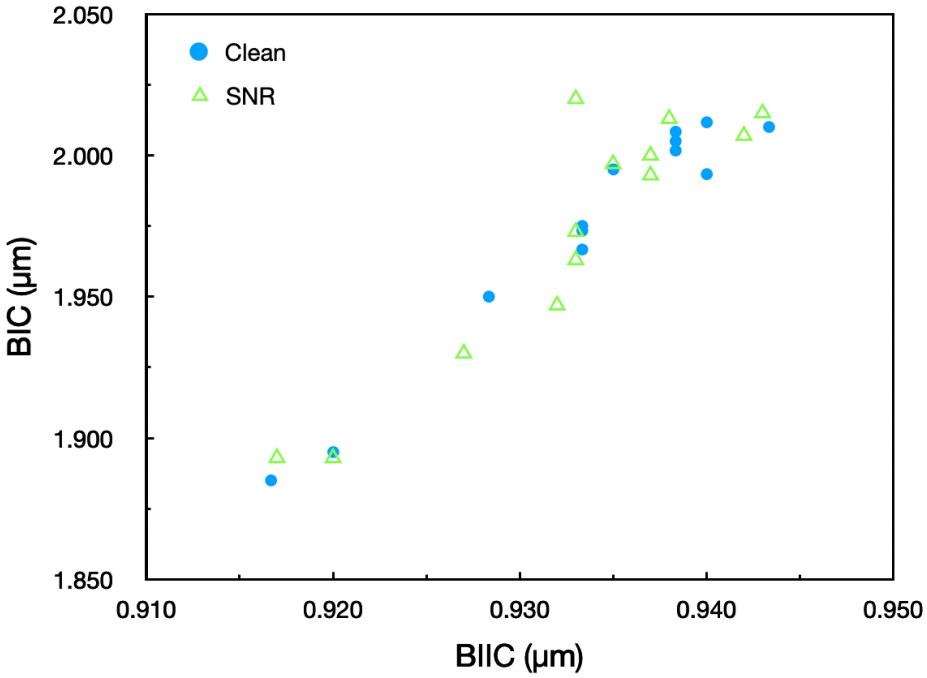

Figure 32: The HED Zone plot. Compares the band centers from the clean (blue) and SNR50 (green) spectral sets.

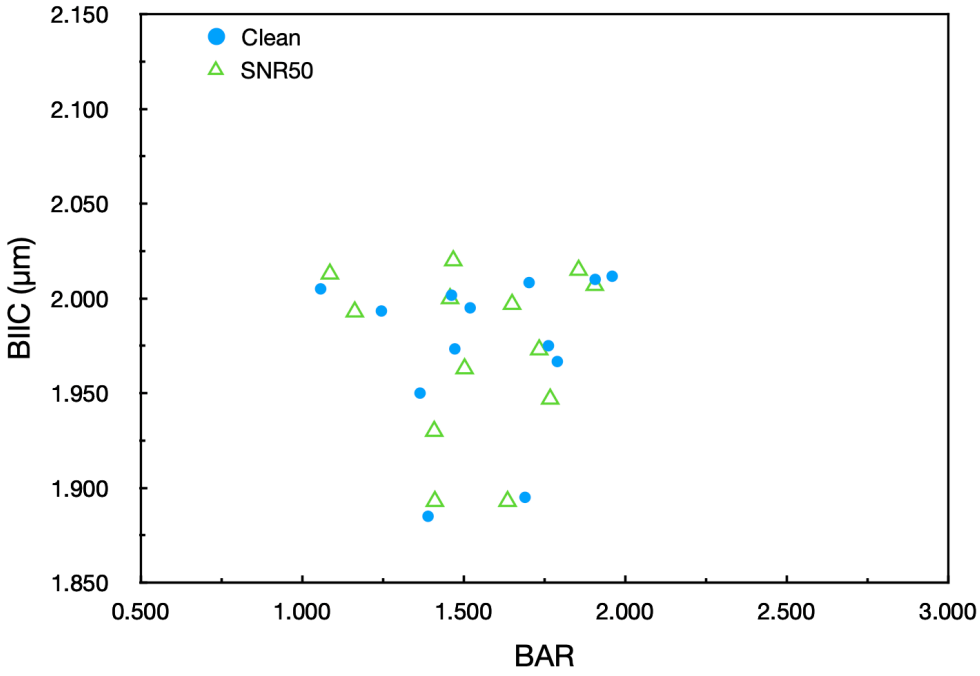

Figure 33: The Burbine sample Band II canters plotted against BARs for the real, 2.5 µm edge combination, for the clean (blue dots) and SNR50 (green triangles) spectral sets.

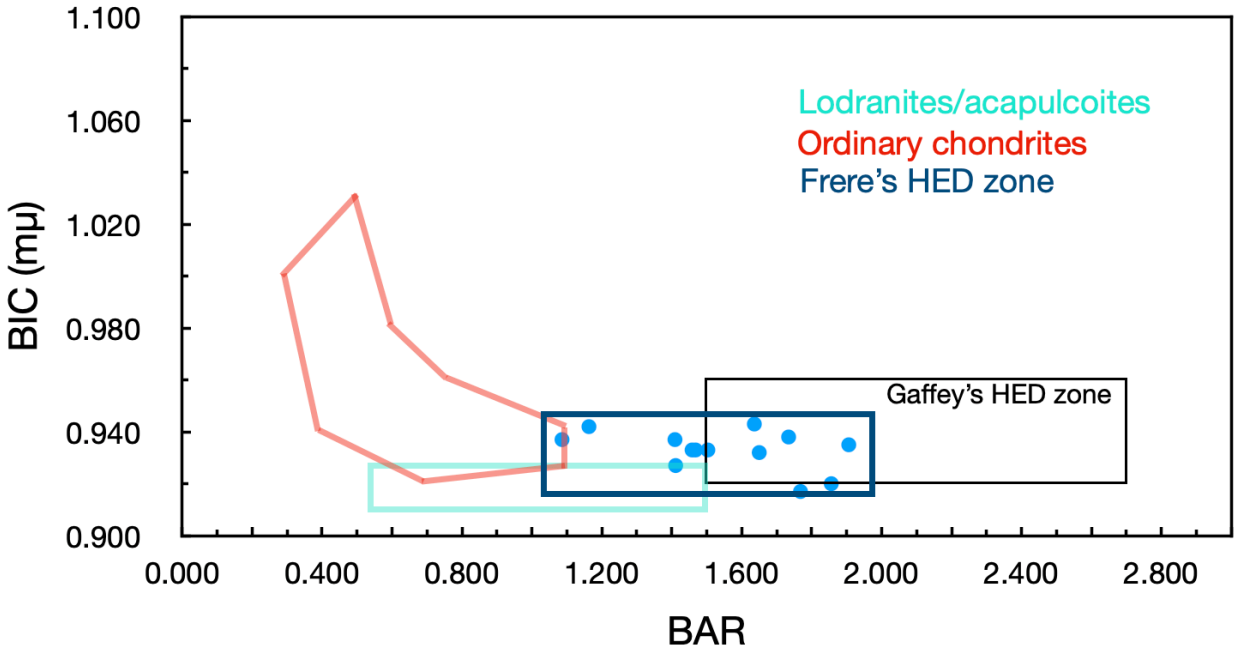

Figure 34: The Gaffey plot for the SNR50 Burbine sample, using the real, 2.5 μm edges.

The motivation to create calibration equations from meteorites is to derive mineralogy for asteroids. By comparing the derived molar contents for asteroids from both the clean as well as SNR50 sets of equations, and for a variety of blue and red edges, I hope to gain insight into the relationship between HEDs and V-types. Additionally, I aim to provide the asteroid research community with a set of equations that reliably determine V-type mineralogy. Such a data set can be used to explore potential parent bodies other than Vesta, and/or the thermal history of this class of asteroids. Ultimately, this sheds light on how our the terrestrial bodies of our solar system formed and evolved. A key step to achieve this is to parse out any inconsistency in the derived chemistry from different absorption features, ie. Band I and Band II.

3.3.1 Temperature Corrections

The purpose of this section is only to justify the use of temperature-corrections. Numerous groups have demonstrated that the 1- and 2-µm absorption features are sensitive to temperature. Changes in temperatures affect the band center positions and width of the absorption features. Band centers move to shorter wavelengths as the temperature decreases (Singer and Rouch, 1985; Schade and Wäsch, 1999; Moroz et al. 2000; Hinrichs and Lucey, 2002; and Sanchez et al. 2012). The meteorite spectra used in this thesis were measured at room temperature (~295 K). Given their distance from the Sun, the main belt asteroid used here have significantly lower temperatures. The V-types used in this study range from 150 K - 205 K with a sample mean equilibrium temperature of 167 K $\pm$ 12 K. Such a large temperature difference should have a noticeable affect on the absorption bands. Since the HED calibration equations apply for spectra measured at room temperature, we must evaluate if temperature corrections to the band parameters are necessary. In the Discussion section I will explore how temperature effects the band centers, and hence the mineralogy derived from the two different absorption features.

In what follows, we use the methodology of Burbine et al. (2009). The temperature of asteroids is calculated as

$$T = \sqrt[4]{\frac{(1-A)L_o}{16\eta\epsilon\sigma\pi r^2}} \tag{7}$$

where L_o is the Solar luminosity (3.828×10^{26} W), A is the bolometric Bond albedo of the asteroid, η is the beaming factor (assumed to be unity), ε is the infrared emissivity of the asteroid (assumed to be 0.9), σ is the Stefan-Boltzmann constant, and r is the heliocentric distance of the asteroid at the time of observation.

The temperature correction equations used here are from Reddy et al. (2012). For eucrites and howardites, the BIC and BIIC corrections are

$$\text{BIC correction (μm)} = 0.01656 - 0.0000552\times\text{T (K)} \tag{8}$$

and

$$\text{BIIC correction (μm)} = 0.05067 - 0.00017\times\text{T (K)} \tag{9}$$

and for diogenites are

$$\text{BIC correction (μm)} = 0.0000000017\times\text{T}^3\text{ (K)} - 0.0000012602\times\text{T}^2\text{ (K)} + 0.0002664351\times\text{T (K)} - 0.0124 \tag{10}$$

and

$$\text{BIIC correction (μm)} = 0.038544 - 0.000128\times\text{T} \tag{11}$$

Using the above equations, Burbine et al. (2018) found that temperature corrections in the BIIC vs. BIC space of their sample of NEAs did not shift the location of asteroids in this space to better overlap with where the HEDs plotted. Therefore they decided to not use temperature corrections on their band centers before deriving molar chemistry. However, NEAs are considerably closer to the Sun than Main belt asteroids, and hence are significantly warmer. The average temperature of the V-types in this thesis is 167 K, while the average temperate of the NEAs in Burbine et al (2018) is 234 K, 40% warmer. Given the large difference in temperature between their NEAs and

MBAs, we re-evaluate the efficacy of temperature corrections to see if they shift our data to better overlap with the HEDs in BIIC vs. BIC space. Indeed, that is what we found.

Figure 35 shows, from the real blue edge, 2.5 µm red edge combination, the BIIC vs. BIC plot of the 17 main belt V-types before temperature corrections (yellow points) and after temperature corrections (blue squares). By drawing boxes around the majority of data points, one can see that the temperature corrections have shifted the V-types (blue box) towards the red box (my HED band parameters), as well as the black box (Burbine's HED band parameters). Changing the red edge has no effect on these trends, and is therefore not further considered in this analysis.

The false blue edge responds differently to the temperature corrections. Figure 36 shows the results of the false blue edge with the 2.5 µm red edge. While the temp-corrected V-type BIICs shift upwards towards the HED BIICs, as expected, the BICs shift to longer wavelengths than the HED BICs. This is likely due to the imposition of an artificially increased slope resulting from not using the entirety of Band 1 to determine the continuum. This will be discussed further in the Discussion section.

Since the overall effect of applying temperature corrections to both Band I and II is to bring the asteroids closer to the HEDs in Figures 35 and 36, we will use the temperature-corrected BICs and BIICs for the asteroids for the remainder of this thesis. Figure 37 shows the effect from all edge combinations. The main thing to note here is that within each blue edge regime (the top three panels are the real blue edge; the lower three panels are the false blue edge), correcting for temperature makes little difference for the different red edges. However, shifting from the real blue edge to the false blue edge regime, both the slope of the V-types' linear fits — which are horizontal in the bottom three panels — as well as the distance between the V-types non-temp-corrected and temp-corrected results changed markedly; and the difference in the linear fit's slope between Burbine's and SARA's band centers differ.

3.3.2. Band Parameters & Molar Contents

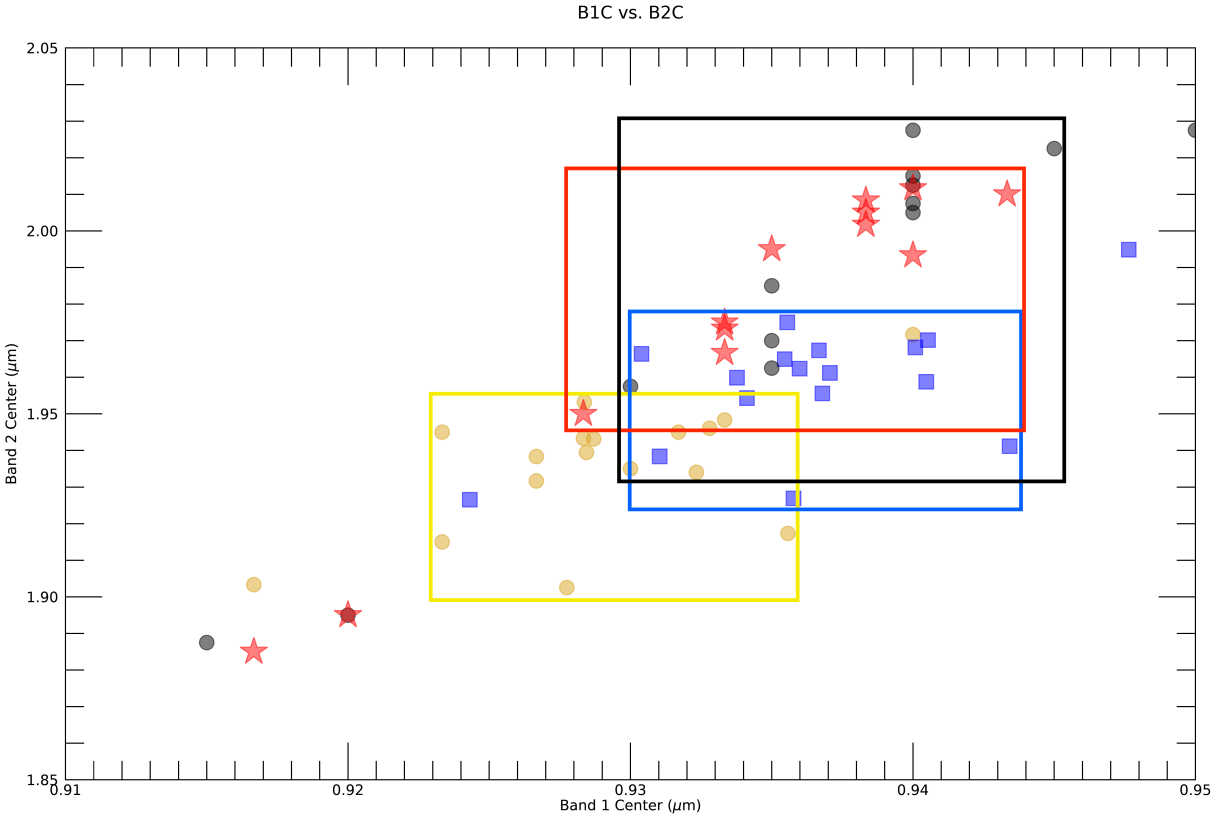

Figure 35: Before & After Temperature Corrections (Real, 2.5 µm). Yellow is non-temp-corrected V-types Blue is temp-corrected V-types. Red is SARA's HED results. Black is Burbine's HED results.

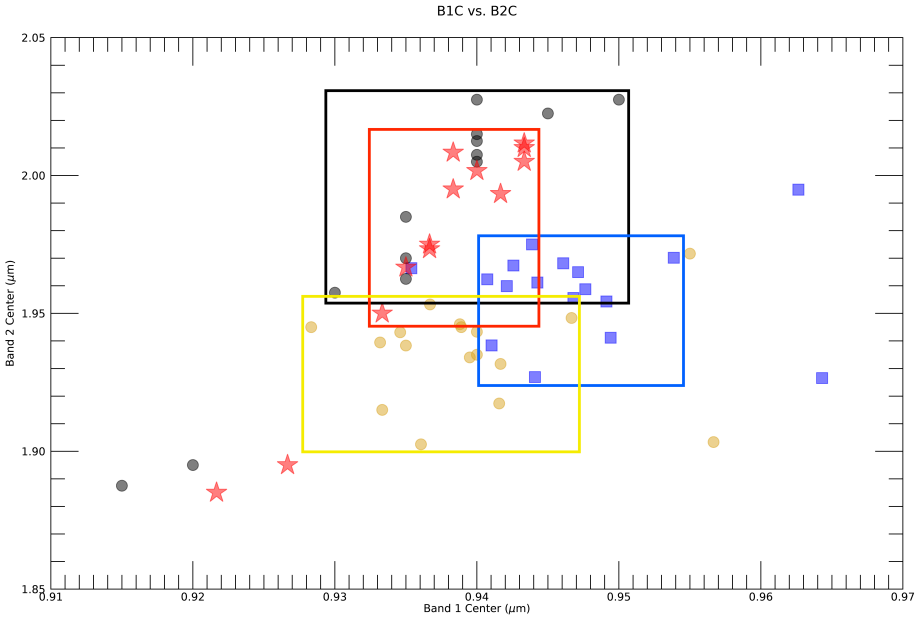

Figure 36: Before & After Temperature Corrections (False, 2.5 µm). Yellow is non-temp-corrected V-types. Blue is temp-corrected V-types. Red is SARA's HED results. Black is Burbine's HED results

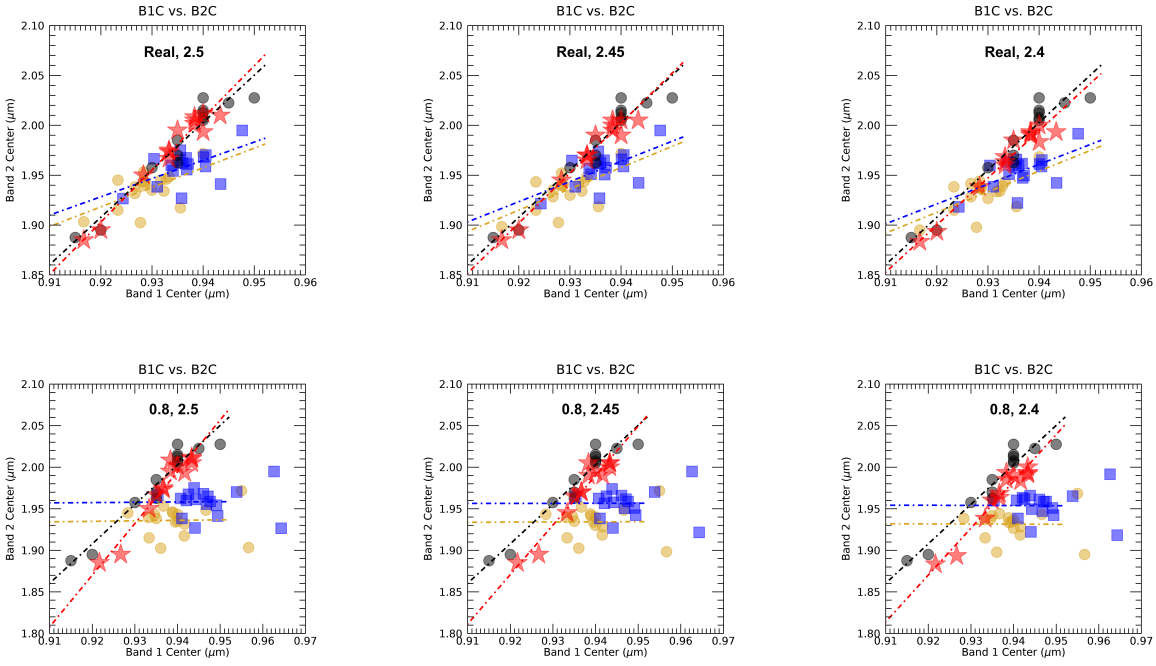

Figure 37: Before & After Temperature Corrections for all edge combinations with best-fit lines. Yellow is non-temp-corrected V-types Blue is temp-corrected V-types. Red is SARA's HED results. Black is Burbine's HED results

Table 10 shows the real, 2.5 µm edge Band I and II centers and errors, BAR and errors, and mol% Fs ave and Wo ave for the 17 V-type asteroids, from the clean spectra. The asteroids are arranged by increasing Wo content, as are all the tables in this thesis. The band centers have been temperature corrected as described in the previous section. The derived molar contents are firmly in the HED range. In fact, the mean Fs ave is identical to the mean Fs ave from the set of 53 HEDs, although the asteroids exhibit about half the standard deviation; and the mean Wo is identical to the EMPA Burbine sample Wo, which is just 0.1% above the Wo ave from the set of 53 HEDs, again with the asteroid standard deviations about half that of the HEDs.

Table 11 shows the SNR50 molar contents for Fs and Wo for both absorption bands, separately and averaged, for each of the 17 V-types, using the real, 2.5 µm edges. They are arranged in the same order as in Table 10. However, the Wo content has changed such that the order no longer goes from low to high Wo, although overall the trend remains.

Table 12 shows the mean derived molar contents from all edge combinations, as well as the Band I slopes for the real and false blue edges. There are dashes in order to highlight repeated information from preceding rows. Unlike for the meteorites, the difference in mol% between Band I & II is very noticeable. The mol% difference (FsI-FsII) is shown in Table 12, with the false edge cases being more than double that of the real edge cases. This is because the false edge FsI gives abnormally high results, with a mean value of ~60 mol%. The reason for this disparity between mineralogy determined using BICs and BIICs is discussed in Section 4.2.

3.3.3 Slopes

The asteroid's slopes are markedly different from the meteorite's — with a mean value several times greater. The real blue edge mean is 0.706 ±0.255, compared with the 53 HED sample mean of 0.087 ±.066. The false blue edge mean is 1.262 ±0.411, compared with the 53 HED sample mean of and 0.218 ±.097. Figure 38 shows a graphical representation of the slopes of the Burbine sample, the set of 53 HEDs, and the V-types.

Table 10: Real, 2.5 µm edge V-type results, arranged by increasing Wo. All band centers and thus molar contents have been corrected for temperature. There is no temperature correction for BAR for vestoids. Fs and Wo are averages of the mol% from the BIC and BIIC equations.

	Band I		Band II				Band 1		
Asteroid	Center	Error	Center	Error	BAR	Error	Slopes	Fs ave	Wo ave
Lee	0.924	0.002	1.927	0.008	2.380	0.025	0.903	32	6
Harbin	0.931	0.001	1.938	0.006	2.118	0.010	0.880	38	8
2001op83	0.936	0.004	1.927	0.023	1.771	0.050	0.829	39	8
LaPalma	0.934	0.001	1.954	0.003	1.920	0.008	0.782	42	9
Volkonskaya	0.934	0.003	1.960	0.009	1.962	0.035	0.618	42	9
Jacliffe	0.930	0.000	1.966	0.002	1.890	0.006	0.557	41	9
Corbett	0.937	0.002	1.956	0.009	2.313	0.022	0.761	43	10
Kirhizia	0.935	0.002	1.965	0.007	1.945	0.019	0.451	44	10
Kastel	0.937	0.001	1.961	0.005	2.154	0.014	0.757	44	10
Kiuchi	0.936	0.006	1.962	0.028	1.802	0.069	0.936	44	10
Kollaa	0.936	0.026	1.975	0.130	1.842	0.290	0.137	45	11
Peking	0.940	0.001	1.968	0.003	1.780	0.008	0.796	47	11
Celle	0.943	0.002	1.941	0.005	1.837	0.024	1.097	46	11
4 Vesta	0.937	0.000	1.967	0.002	1.917	0.004	0.270	45	11
Lundia	0.940	0.002	1.959	0.004	1.865	0.017	1.001	46	11
Kitezh	0.941	0.000	1.970	0.004	1.924	0.011	0.711	47	12
Spartacus	0.948	0.003	1.995	0.017	1.359	0.028	0.516	55	14
All mean st. dev.	0.936 ±0.005	0.003	1.958 ±0.017	0.016	1.928 ±0.230	0.038	0.706 ±0.255	43.6 ±4.7	10.1 ±1.8

Table 11: SNR50 derived mol% Fs and Wo from the real, 2.5 µm edges. The asteroids are arranged by increasing Wo according to the clean derived mineralogy as seen in Table 10.

Asteroid	FsI	FsII	Fs ave	WoI	WoII	Wo Ave
Lee	33.9	34.0	34.0	5.8	6.4	6.1
Harbin	41.8	36.5	39.1	9.2	7.3	8.3
2001op83	47.3	34.1	40.7	11.6	6.4	9.0
LaPalma	45.3	39.9	42.6	10.8	8.6	9.7
Volkonska	44.9	41.1	43.0	10.6	9.1	9.8
Jacliff	41.0	42.5	41.8	8.9	9.6	9.3
Corbett	48.5	40.2	44.3	12.1	8.7	10.4
Kirghizia	46.9	42.2	44.6	11.4	9.5	10.5
Kastel	48.8	41.4	45.1	12.2	9.2	10.7
Kiuchi	47.5	41.7	44.6	11.7	9.3	10.5
Kollaa	47.0	44.4	45.7	11.5	10.3	10.9
Peking	52.3	42.9	47.6	13.7	9.8	11.8
Celle	56.2	37.1	46.6	15.4	7.6	11.5
4 Vesta	48.3	42.7	45.5	12.0	9.7	10.9
Lundia	52.7	40.9	46.8	13.9	9.0	11.5
Kitezh	52.8	43.3	48.1	14.0	9.9	12.0
Spartacus	61.1	48.6	54.9	17.5	12.0	14.7
Mean	48.0	40.8	44.4	11.9	9.0	10.4
St. dev.	±6.2	±3.7	±4.4	±2.7	±1.4	±1.8

Table 12: Mean derived molar contents from 17 asteroids for all edge combinations, as well as Band I Slope. (From the clean equations)

Blue edge	Red edge	FsI	FsII	Fs ave	FsI - FsII	WoI	WoII	Wo ave	WoI-WoII	BI Slope
Real	2.5	47.2 ±6.5	40.0 ±4.1	43.6 ±4.7	7.2 ±5.4	11.4 ±2.6	8.7 ±1.6	10.1 ±1.8	2.8 ±2.1	0.706 ±0.255
	2.45	-	40.3 ±4.4	43.7 ±4.9	6.8 ±5.4	-	8.8 ±1.6	10.1 ±1.9	2.6 ±2.0	-
	2.4	-	40.9 ±4.5	44.0 ±5.0	6.2 ±5.1	-	9.0 ±1.7	10.2 ±1.9	2.4 ±2.0	-
False	2.5	58.9 ±10.8	-	49.4 ±5.8	18.9 ±11.5	16.2 ±4.3	-	12.4 ±2.3	7.5 ±4.6	1.262 ±0.411
	2.45	-	-	49.6 ±5.8	18.5 ±11.6	-	-	12.5 ±2.3	7.4 ±4.6	-
	2.4	-	-	49.9 ±5.8	17.9 ±11.7	-	-	12.6 ±2.3	7.2 ±4.7	-

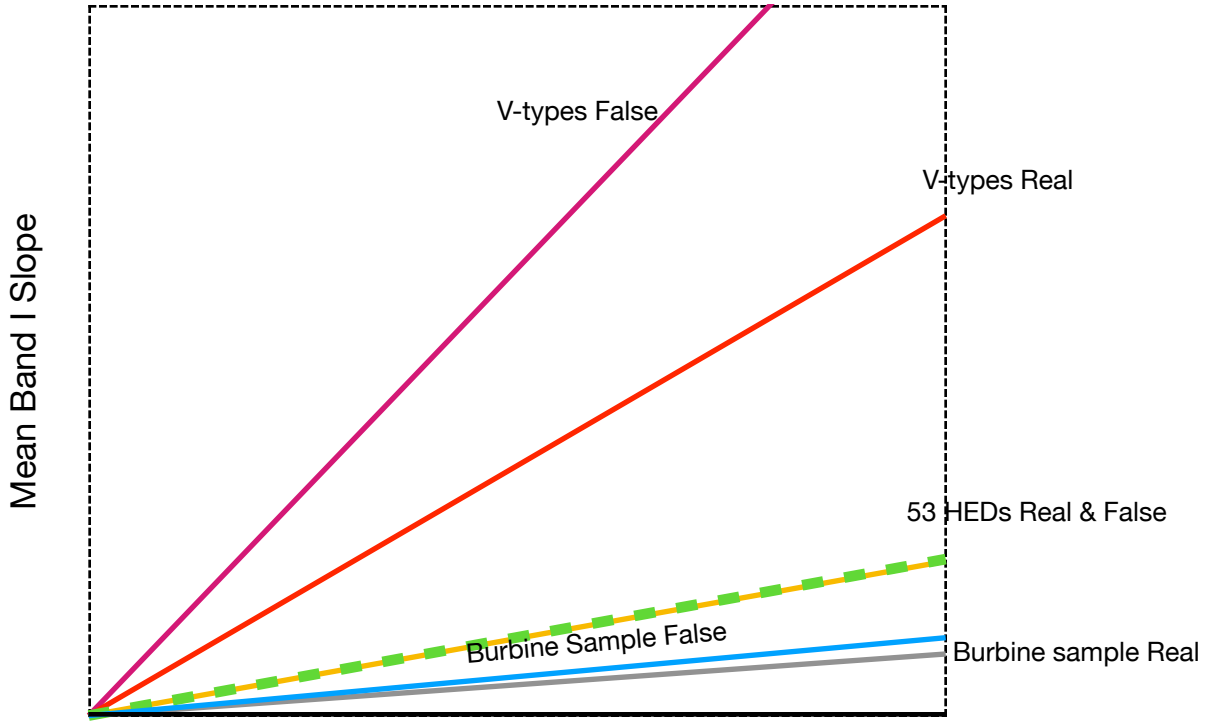

Figure 38: A graphical representation of the HED and V-type slopes

The bottom two lines are the mean HED real blue edge slopes. The middle two lines are the mean HED false blue edge slopes and are almost identical, and the top two lines are the mean asteroid slopes. Not only is the difference between the meteorite and asteroid slopes great, but the difference between the real and false blue edges *within* the asteroid slopes is also great, and much larger than the difference in real to false blue edge slopes for the HEDs. It has been known for decades that asteroid slopes were redder (an increasing reflectance from shorter to longer wavelengths) than their meteorite counterparts (Gaffey 1976, Burbine et al 2001). Only Kollaa has a shallower slope (0.137) than any of the meteorites, in this case six of the Eucrites. Figure 39 shows the asteroid slopes as a function of BIIC and BIC superimposed onto the meteorites plot from Figure 8.

3.3.4 Modified Band I "centers"

In § 3.1.6 I showed that combining the three parameters of BIC, BIM and BIS produced alternative Band I centers for HEDs, which, when propagated through the nominal BIC equation, yielded mineralogy very similar to the EMPA values. Here, we use the equations (3, 4 and 5) to calculate the modified Band I centers for the V-types. Table 13 summarizes the means of all Band I "centers" I tested for both the meteorites and asteroids. The table also shows the derived mol% FsI from using only the real blue edge (hereafter "nominal") BIC Calibration equation. I did not apply temperature corrections to the modified BICs because they were derived from band centers that had already been temperature-corrected.

These modified band centers are more of an empirical correction than a physical phenomenon. Figure 40 summarizes the mol% Fs calculated from several different methods, all for the real, 2.5 µm edge combination. Note the anomalously high value for the mean BIC_{mod} (0.945 µm) and the FsI (57.1 mol%) resulting from using them as inputs into the regular BIC calibration equation. Based on this overestimation, we conclude the original offset equation produced from using only the HEDs is not effective for deriving mineralogy for the V-type asteroids.

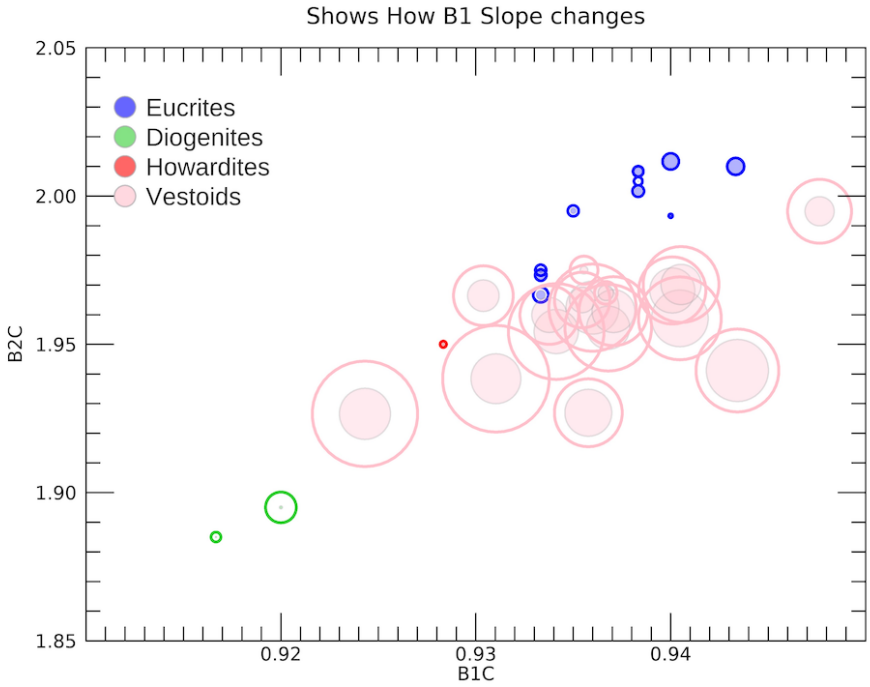

Figure 39: Shows how slopes change. Discs are real blue edge slope magnitudes between 0.003 and 0.265. Circles are false blue edge slopes with magnitudes between .069 and .542. The 2.5 µm red edge was used.

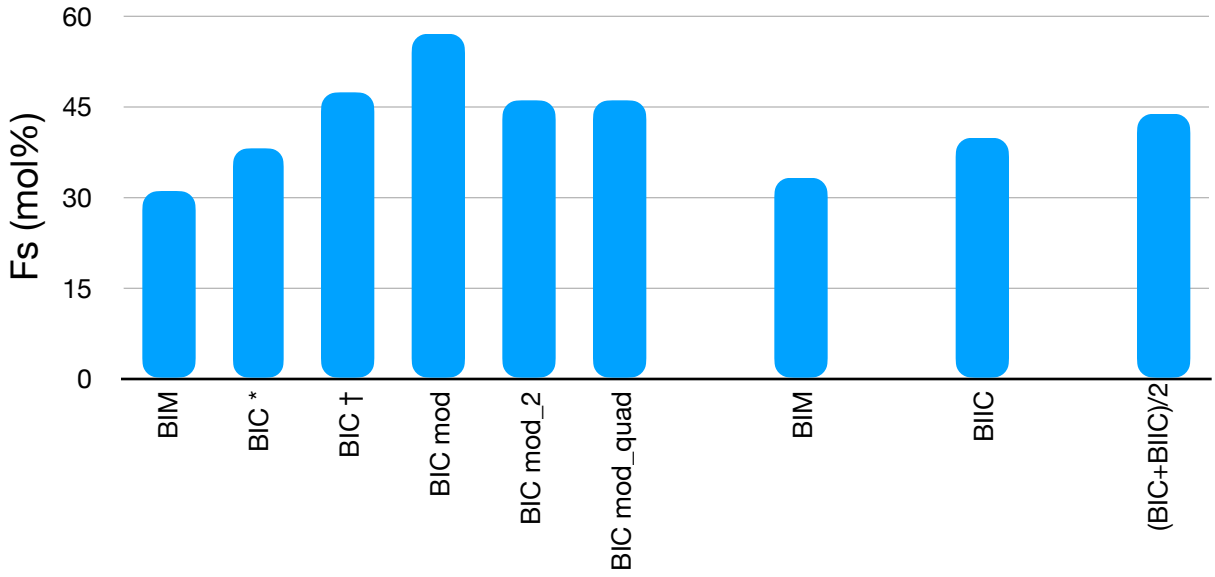

Figure 40: Fs (mol%) from using different Band centers and equations. The six bars on the left use the real BIC equation, the bar labeled BIM uses the BIM equation, the bar labeled BIIC uses the 2.5 red edge BIIC equation, and the last bar represents the average of FsI and FsII from the temp-corrected BICs and BIICs.

Table 13: Various mean Band I "centers" and derived mol% Fs. Temp-corrected B1Cs were used for the offset equation which produced the BICmods.
† from 13 HEDs and V-types

	13 HEDs Band I "centers" (µm)	V-types Band I "centers" (µm)	FsI (mol%) from BIC Equation
B1 Min	.932 ± .007	.923 ± .006	31.1
B1 Center (non-temp-corrected)	.934 ± .008	.929 ±.005	38.2
B1 Center (temp-corrected)	-	.936 ± .005	47.2
BIC_{mod} (13 HEDs)	.934 ± .008	.945 ± .009	57.1
BIC_{mod_2} (all†)	.933 ±.008	.936 ±.006	46.2
BIC_{mod_quad} (all†)	.933 ±.008	.935 ±.005	45.9

It is notable that the mean BIC_{mod_2} is identical to the mean temp-corrected BICs, and only 0.001 µm shorter than the mean BIC_{mod_quad}. The derived molar contents from these equations is shown in Figure 41. FsI from using the temp-corrected BICs is very close to the FsI from using both the BIC_{mod_2} and BIC_{mod_quad} centers. In order to know which of the latter two "centers" produces results most similar to nominal B1C results, I plot the modified centers against the nominal BICs in Figure 42. Figure 42a plots the BIC_{mod_2} centers, and Figure 42b plots the BIC_{mod_quad} centers. A slope of unity would signify that the modified centers are identical to the nominal BICs. Although Figure 42a exhibits a linear fit closer to unity, with a slope of 0.97, then Figure 42b, with a slope of 0.93, it has a smaller R^2 value of 0.71, compared with the Figure 42b R^2 value of 0.81. The greater scatter in the data in Figure 42a prompts me to conclude that BIC_{mod_2} may not not more useful than BIC_{mod_quad} despite its 0.97 coefficient.

3.3.5 HED Analog Zones

A chief goal of researching asteroids is matching them up with their meteorite analogs. Deriving mol% Fs and Wo is one way to compare the V-types and HEDs. If a meteorite shares the geochemistry with an asteroid, then an argument can be made that that the meteorite was ejected from that asteroid. This helps identify potential parent bodies for the meteorites as well as the dynamic and thermal history of the asteroid belt. For the HED - V-type connection, identifying if the asteroids are more howardite, eucrite, or diogenite-like can help: identify if there are multiple parent bodies for the basaltic achondrites; provide additional evidence for how Vesta formed and differentiated (see McSween et al. 2013 for a thorough summary); and generally increase our understanding on how the inner solar system bodies formed. Since the derived molar contents rely upon band parameters, we can identify where the asteroidal band centers and BAR lie in the HED zones identified in § 3.1.7.

Figure 43 shows where the V-type band centers from the real blue edge over-plot onto the HED zones delineated earlier in Figure 16. 14 of the 17 V-types lie within the

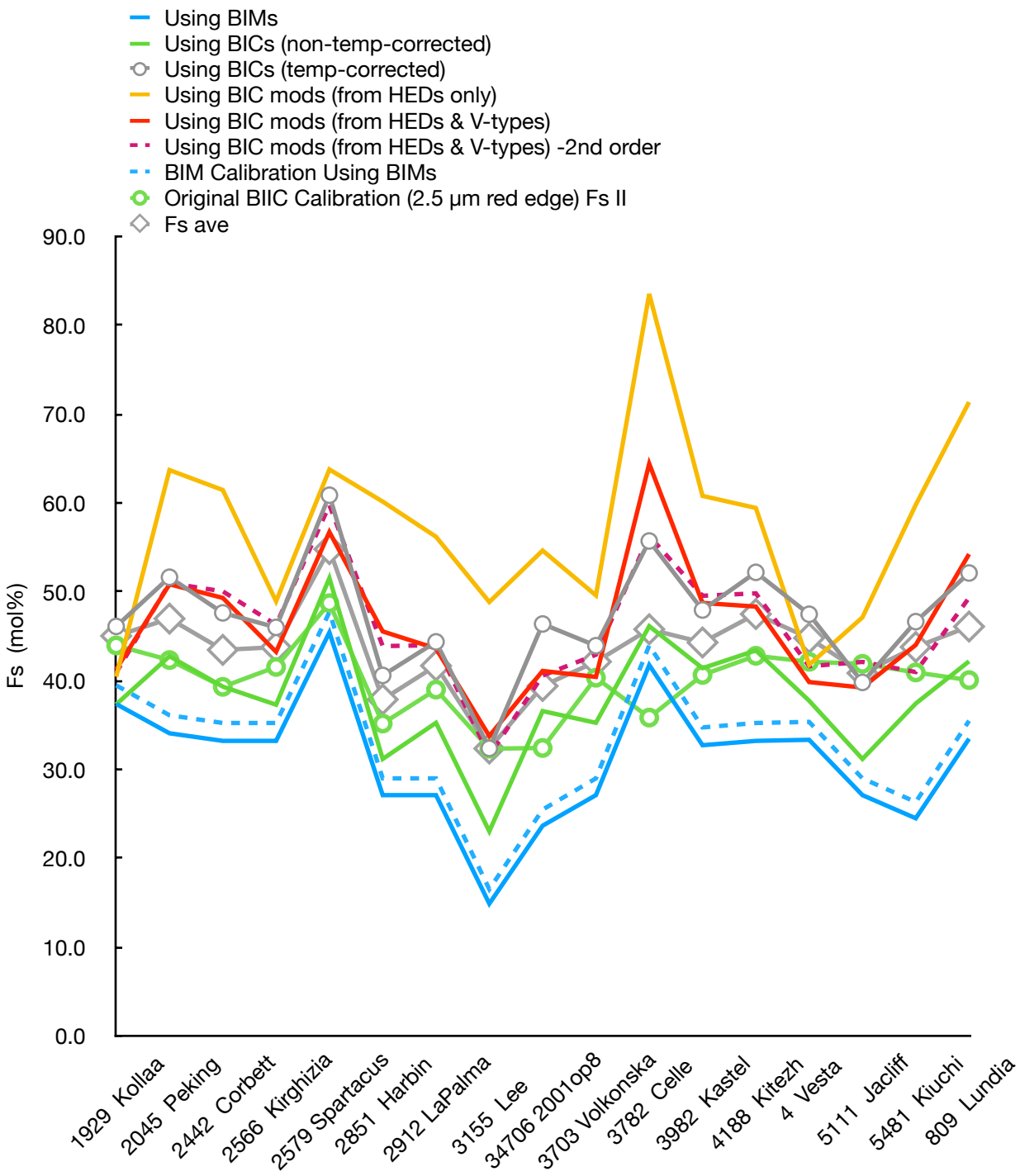

Figure 41: 6 different calculations of derived mol% Fs from using various Band I "centers" in the same nominal BIC calibration equation, as well as FsI derived from the BIM calibration equation. Also shown is FsII and Fs ave.

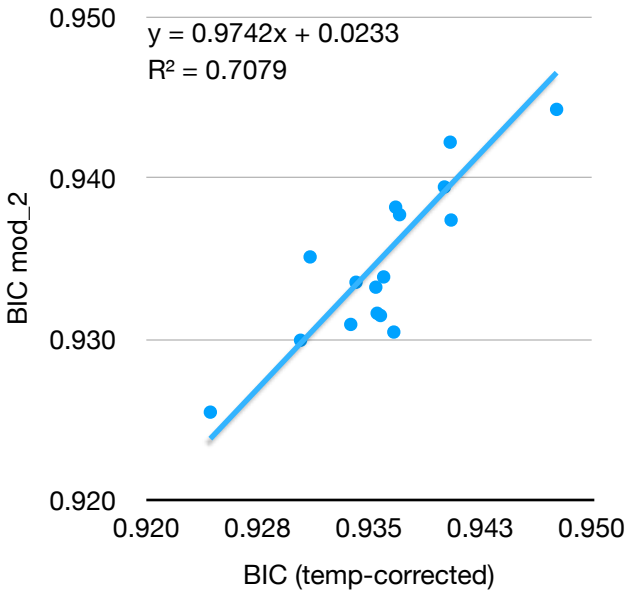

Figure 42a: BICmod_2 is plotted against the temp-corrected BICs and fit with a linear regression.

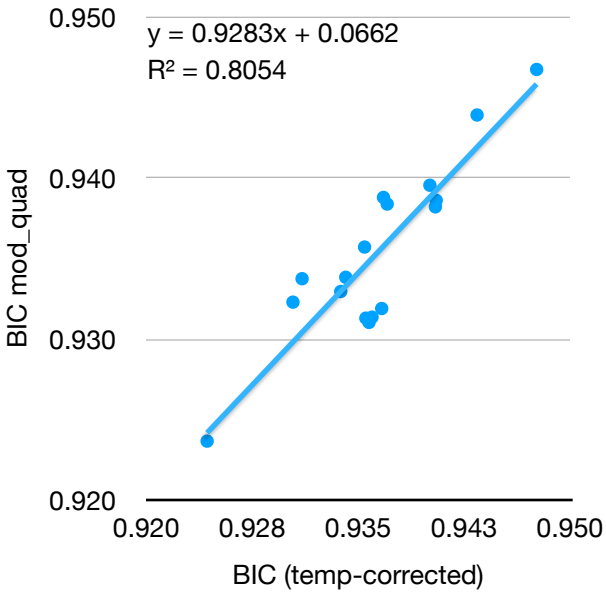

Figure 42b: BICmod_quad is plotted against the temp-corrected BICs and fit with a linear regression.

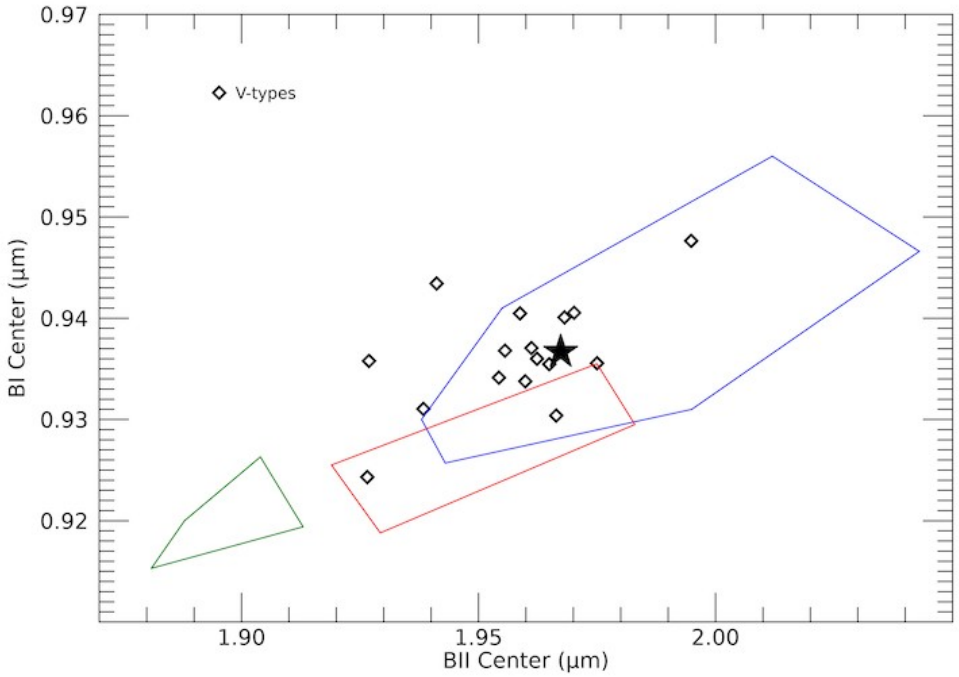

Figure 43: HED Analog Zones for the real blue edge. V-types (diamonds) are plotted onto the eucrite zone (blue polygon), howardite zone (red polygon) and diogenite zone (green polygon). Vesta is the black star.

zones, with one on the cusp. Only three lie in the howardite zone, two of which overlap the eucrite zone, suggesting that they may be cumulate eucrites rather than howardites. Vesta lies in the eucrite zone. None of the asteroids plot near the diogenite zone. This supports earlier research which has found a dearth of diogenitic asteroids in the solar system (Burbine et al. 2001). This is thought to be because the diogenite material lies deep inside Vesta, and if the V-types are mostly ejecta from collisions of minor bodies with Vesta, then it would be difficult to explain a scenario in which a large amount of diogenitic material could be excavated from Vesta without being mixed with eucritic material (which lies closer to the surface), resulting in howardite-like compositions.

Figure 44 is like Figure 43 except for the false blue edge band centers. This contrasts with the previous figure in that eight asteroids lie outside of the zones, although three are right on the cusp of the eucrite zone. Only one asteroid lies inside the howardite/cumulate eucrite zone. The preponderance of asteroids outside of the zones in Figure 44 does not mean that their compositions are not analogous to HEDs; rather, it suggests that the band centers calculated from a false blue edge are prone to error when it comes to assigning meteorite analogs.

In § 3.1.7, Figure 18 showed the three meteorite subtype areas as a function of BIIC and BAR for the 53 HED sample. In Figure 45 I present the V-type data points in a likewise manner, with the means and 1-σ standard deviation of the HEDs represented by crossbars for reference. Since Figure 18 shows significant overlap between the eucrites and howardites, we can interpret the asteroid data points in Figure 45 as suggestive of both subtypes. Prima facie, this appears to clash with the meteor analog assignments of Figure 43. However, regarding that figure, notice that it is the BICs that lift the asteroids out from the howardite zone and into the eucrite zone. Therefore, BIICs are not entirely effective in separating the HED subtypes from one another. Moskovitz et al. (2010) found that their sample of near-earth V-type asteroids plotted farther to the right (larger BARs) then my sample. This could be attributed to compositional differences between the two samples, or to different band analysis techniques. Unlike the case with the HEDs, there is no obvious trend with Band I slope. This could suggest a somewhat uniform geochemistry for the V-types studied in this thesis, or other, unaccounted-for surface effects that homogenize the band parameters for asteroids.

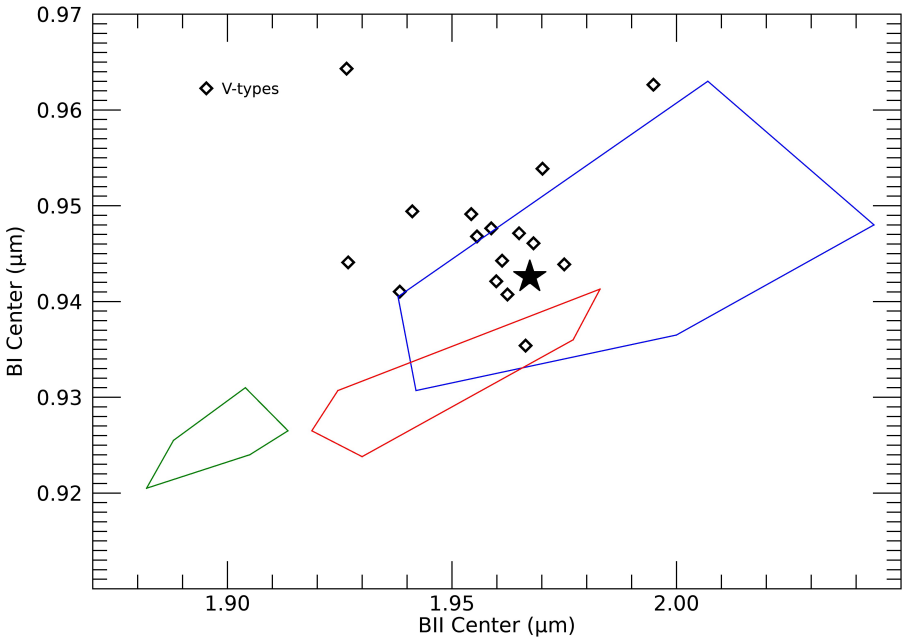

Figure 44: HED Analog Zones for the false blue edge. V-types (diamonds) are plotted onto the eucrite zone (blue polygon), howardite zone (red polygon) and diogenite zone (green polygon). Vesta is the black star.

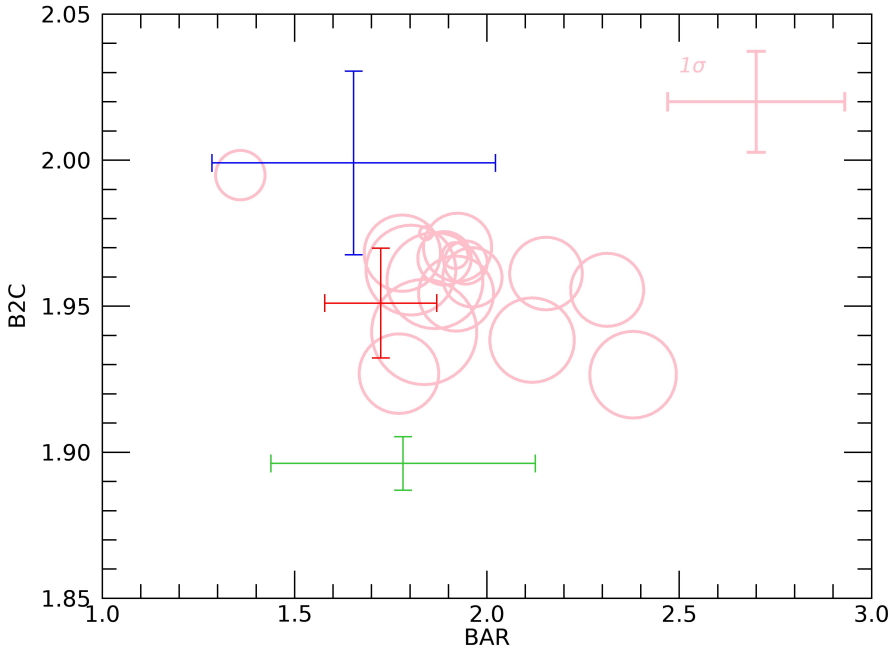

Figure 45: Pink circles are V-types from the real, 2.5 µm edges, with their 1-sigma standard deviation shown in the upper right corner. The blue, red and green crosshairs are HED means and 1-sigma standard deviation for the eucrites, howardites and diogenites, respectively. The bubble diameter signifies Band I slope.

The third method of displaying HED zones that I explore in this thesis is the Gaffey plot, shown in Figure 46. Four of the asteroids lie outside of the BA zone, with BARs higher than the HED BARs.

3.3.6 SNR50

In § 3.2 I showed that decreasing the SNR of the HEDs resulted in different equations and calculated mineralogy compared to the clean spectral sets. The coefficient of determination R^2 and RMS for the Fs calibration equations noticeably increased, but only slightly changed for Wo, compared with those values from the clean Burbine sample spectral set. In this section, I present the derived mineralogy from using the V-type band parameters in the SNR50 equations, and compare it to the results from the clean calibration equations.

Table 14 shows summarizes the SNR50 mol% Fs results as compared to the clean spectra results. The table is organized so that the first row contains results from the clean spectra, with the following row containing the results from the noisy spectra, using the same band parameter and corresponding equation calculated from that parameter. In most cases, the mean Fs rose by roughly 1 mol% when going from the clean equations to the SNR50 equations (Δmol%). The most notable exception to this is the false BIC results, which lowered by 2.8%, which highlights the volatility of a truncated blue edge. The derived FsI from these false BICs and equations are over 55 mol%. The real BIM Δmol% also lowered, but only by 0.5%, demonstrating that BIMs from un-truncated Band I spectra are robust to the noise-level of the spectra. However, as with the case presented immediately above (false BIC results), the derived mol% FsI from these centers are very far in value from the composition of the HEDs — only in this case the value is far lower than expected, by about 10 mol%.

In terms of derived Fs from a single absorption feature (that is either Band I or Band II), the SNR50, 2.4 µm edge combination gives the closest mol% Fs to the Burbine sample EMPA values. This similarity is likely just a coincidence occurring because of the different band parameter methods, and it should not be interpreted as having some physical meaning.

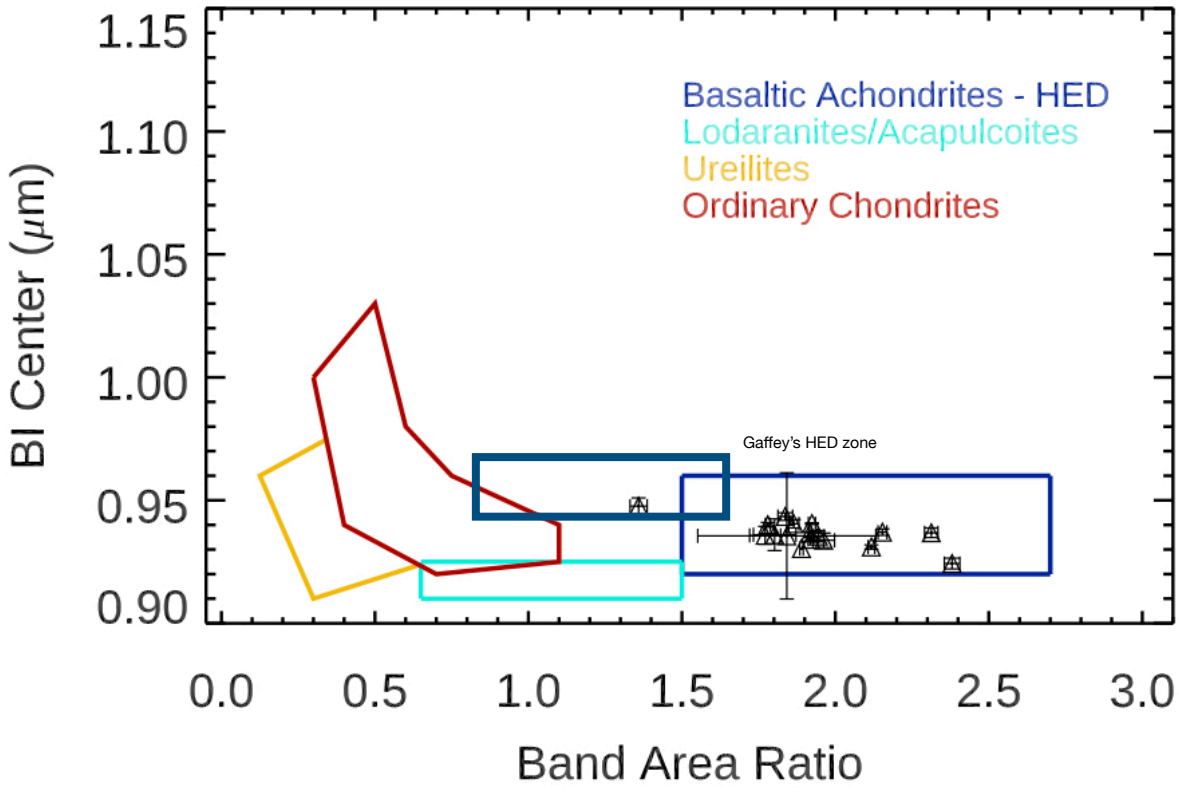

Figure 46: Gaffey plot with the 17 V-type asteroids shown with 1-sigma error bars. The real, 2.5 µm edges were used. The thick blue rectangle denotes my HED zone fro this thesis.

Table 14: Asteroid mean Fs mol% from different calibration equations. Fs Ave is the average of Band I and Band II results form the real, 2.5 edges. Δmol% shows change from the Clean results to the corresponding SNR50 results.
The last three rows show meteorite Fs.

Calibration Equations coming from various band "centers" & edges	**Asteroid Mean Fs mol%**	**Δ mol%(SNR - Clean)**
Clean Real BIC	47.2	
SNR50 Real BIC	48.0	0.9
Clean False BIC	58.9	
SNR50 False BIC	56.0	-2.8
Clean Real BI mins	33.1	
SNR50 Real BI mins	32.6	-0.5
Clean False BI mins	34.6	
SNR50 False BI mins	35.2	0.5
Clean 2.5 µm BIIC	40.0	
SNR50 2.5 µm BIIC	40.8	0.8
Clean 2.45 µm BIIC	40.3	
SNR50 2.45 µm BIIC	41.2	0.9
Clean 2.4 µm BIIC	41.0	
SNR50 2.4 µm BIIC	42.0	1.1
Clean Real, 2.5 Fs ave	43.6	
SNR50 Real, 2,5 Fs ave	44.4	0.8

Various sets of Meteorites mean Fs mol%	
13 HEDs EMPA	43.9
13 HEDs Clean & SNR50 Real, 2.5 µm	43.9
53 HEDs Clean Real 2.5 µm	43.6

Fs ave is computed by averaging the derived mineralogy from Band I and Band II. For Band I, either the BIC or the BIM can be used, with each one having two iterations, depending on which terminal blue edge is chosen — real or false. Band II has three different BIIC values depending on which terminal red edge is chosen. For the clean spectral set, these parameters can be combined in different ways to form 12 different values for Fs ave. Likewise, the SNR50 spectral set produces 12, for a total of 24 different values of mean asteroidal Fs ave. Figure 47 displays theses values in a bar chart. The real, 2.45 edge combination using the BICs (as opposed to the BIMs) yields the closest mean spectrally derived Fs to the Burbine sample EMPA Fs, only 0.1 mol% lower. The real blue edge, 2.5-µm red edge combination using the BICs yields an identical mean value to the set of 53 HEDs, even though there is no a priori reason to assume that would be the case, especially considering the disparity between Band I and Band II molar results. However, it does suggest that if one can obtain spectra with complete absorption features between 0.7 and 2.5 µm, or even 2.45 µm, then the procedure utilized to calculate Fs ave is a wise one.

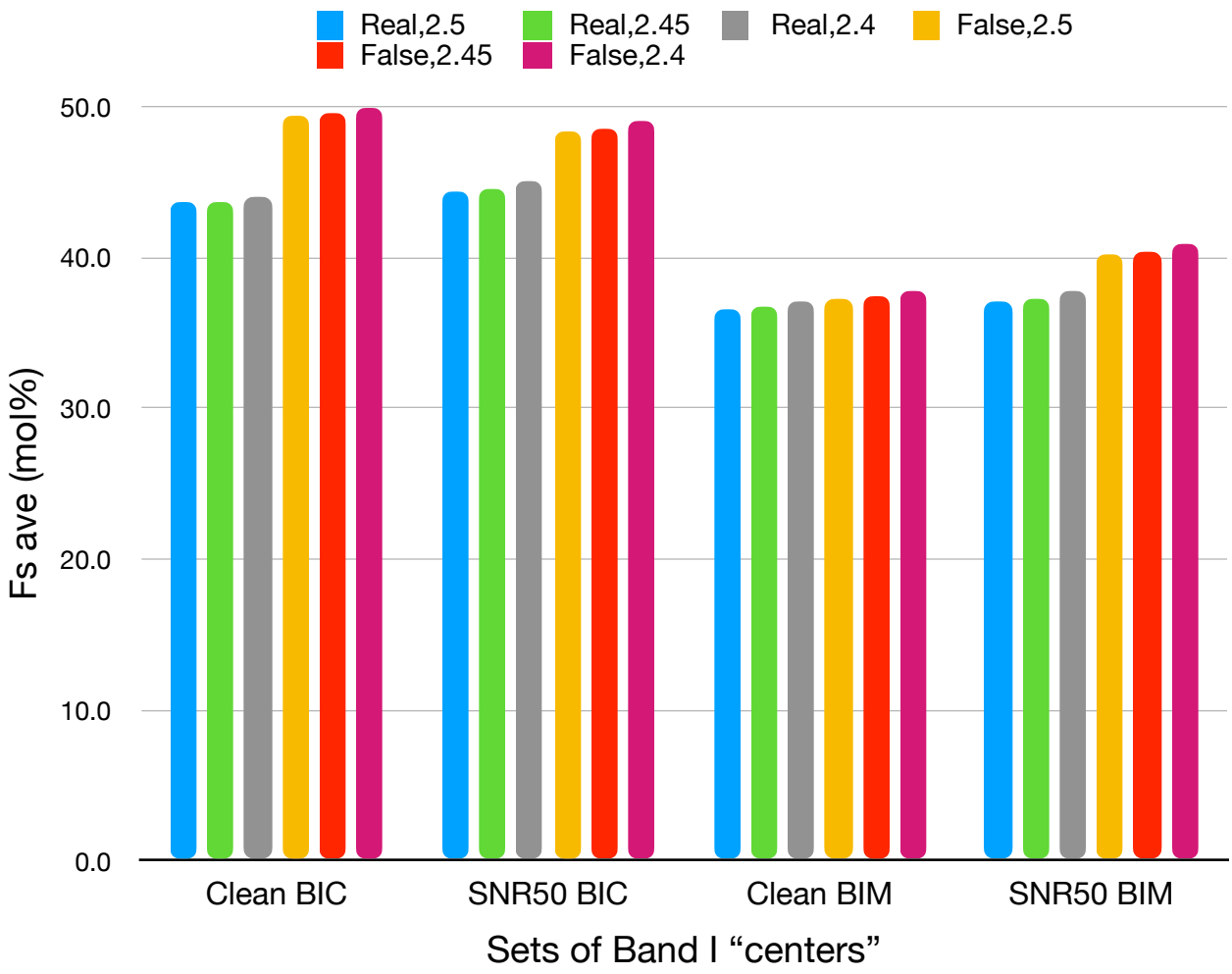

Figure 47: Fs ave calculated in 24 different ways.

Chapter 4 ☽ Discussion

I will discuss two themes here. First, I discuss the relationship between the calibrations and the HED zones. Specifically, I will demonstrate how the location of regions in band parameter space designed to identify meteorite analogs is sensitive to the band parameter analysis used. This analysis investigates meteorite zones in band parameter space designed to identify general HED-like mineralogies and to separate howardite-, eucrite-, and diogenite-like mineralogy for asteroids.. These discussion will lead to a series of recommended uses of the calibration equations presented in the results aimed at providing he community with prescriptions to best retrieve mineralogy from remote observations of V-type asteroids.

Second, I will discuss the disparity of calculated molar chemistry between Band I and Band II for the V-types in this study. The derived FsI from the BIC equations are ~4 mol% higher than that of the HEDs, and the derived FsII from the 2.5 µm red edge BIIC equations are ~4 mol% lower than that of the HEDs, so that the average from FsI and FsII almost equals the EMPA values of the Burbine sample, as well as the calculated Fs ave from the greater 53 HED sample. Since we assume that the HEDs are representative of the V-type asteroids, I look for a physical mechanism that shifts BICs and BIICs in equal, but opposite ways so that the average comes out close to the expectation.

4.1 Calibrations and Meteorite Zones

Burbine et al. (2007, 2009) produced the first set of calibration equations calculated using the true molar contents of HEDs. 11 years later Burbine et al. (2018) produced a new set of equations using the same EMPA values from those same 13 meteorites, but using different band parameters. In this thesis, I present several new equations, once

again using the same Burbine sample. This demonstrates the lack of data available for formulating new calibrations for Vesta-like meteorite analogs. Only one of the 13 in this sample set is a howardite, which is defined as a meteorite having a eucrite:diogenite mixing ratio of 10:1 (Delaney et al. 1983). Since howardites have band centers and mol% values near the middle of the range comprising the band centers and mol% values of the Burbine sample, it doesn't effect the calibration as heavily as the diogenites, which constrain the calibration at the lower values. Although there are only two diogenites in the Burbine sample, the addition of more diogenites with known EMPA mol% values would probably not effect the calibration drastically. For example, Figure 26 in § 3.2.1 displays two calibration equations very different from one another (the clean false blue edge BIC equation, and the SNR50 false blue edge BIC equation), yet when they are used on the asteroid BICs, they result in only a ~3 mol% difference, which is well within the uncertainties of both equations.

My results showed that different calibrations yield different results when deriving molar contents for V-type asteroids. This is true in two senses: one, for different versions of the same type of calibration — for example the Burbine et al. (2009) BIC equation, and my BIC equation; and two, for equations produced by different band parameters — for example my BIM equation, and my BIC equation; or the 2.5 µm red edge BIIC equation, and the 2.45 µm red edge BIIC equation. In all, there are 35 different calibration equations covered in this thesis. Some of them produce similar mol% values, while others do not. In § 3.1.5 and § 3.2.4 (frequency analysis) I showed that using band parameters in equations that were produced by different, incompatible band parameter techniques, yield incorrect mineralogical determinations. Therefore it is important that a researcher use the calibration equations that are applicable to the band parameter analysis methods they used, or to derive their own equations. Specifically, an equation that most closely matches the assignment of the blue edge and red edges should be used if individualized calibration equations are not used. In cases where NIR only data is available, the 0.8-µm false blue edge equation that best matches the band parameter analysis's choice of red edge should be used. For all studies of asteroids with SNR ~50, the set of SNR50 equations should be used to have realistic estimates for the mol% uncertainties.

In § 3.1.5 I suggested that because the SNR50 false blue edge BIM equation, Fs I (± 4.1) = 1380.8 × BIM - 1241.4, has a lower RMS error, that it might return derived asteroidal mineralogy more closely resembling the HEDs than the other Band I equations. Table 14 shows that the mean mol% Fs for the V-types using that equation is 35.2 mol%. While, compared with results from the other three BIM equations, this value is closer to both the Band II results as well as the mean HED mineralogy (43.6 mol% Fs), it is over twice the RMS error (2-σ) of the calibration equation away from the mean HED mineralogy. 35.2 mol% severely underestimates the expected mineralogy of the V-types. Since averaging this value with the already low FsII values yields incorrect, and likely underestimated, mineralogical results, I do not recommend using the Band I minimum in the case when only incomplete spectra are obtained in the Band I wavelength range. Rather, I recommend dispensing with the Band I equations altogether, and just using the SNR50 FsII equation from the 2.4 µm red edge. However, if a researcher finds that the SNR50 false blue edge equation returns reasonable results within one standard deviation of the HEDs mol% Fs (because their data set will be different from mine), then I recommend that they average FsII with FsI. Although the mean derived FsI from that equation is higher than expected (56 mol%) for my V-types, averaging that value with SNR50 FsII from the 2.5 µm red edge gives a mean value of 48.4 mol% Fs for the V-type asteroids, which is not too far from the 43.9 mol% Fs for the Burbine sample, and within the RMS error of many of the calibration equations presented in this thesis.

These different calculated V-type mineralogies based on which calibration equation is used, and if it matches the edge choices for the band parameter analysis used, results in different chemical compositions, but it also effect the meteorite analog assignments. This can be seen in the three different types of zoning spaces: BIC vs. BIIC (Figs., 15 & 16 for HEDs; Figs. 36 & 37 for V-types), BIIC vs. BAR (Fig. 16 for HEDs; Fig. 38 for V-types) , and BIC vs. BAR (Fig. 18 for HEDs & Fig. 39 for V-types., also called the Gaffey plot. The first two attempt to separate the three basaltic achondrite subtypes (howardites, eucrites and diogenites) from each other, while the last one is meant to separate one type of meteorite from another type, such as the HEDs from the ordinary chondrites. None of the zones, initially delineated with the clean spectral set (See Section 3.1.7), changed as a result of adding noise to the Burbine sample spectra,

although an increase in variance of the SNR50 band parameters is noted (Fig. 27). The zones in the BIC vs. BIIC space, and the Gaffey plot, moved significantly when going from the real to the false blue edge. The meteorite zones are strongly dependent on the choice of blue edge. This shows that care in meteorite analog assignment needs to be taken for NIR-only asteroid data sets. If a researcher naively uses the canonical HED zone from Gaffey et al. (1993), or the howardite-eucrite-diogenite zones from Moskovitz et al. (2010), then they may conclude that their asteroids in their sample are not representative of HEDs and may be better classified as S-types. The S- and V-types have significantly different formations and thermal histories, so these errors could lead to missed opportunities to deepen our understanding on the formation and evolution of the asteroid belt and the solar system. For those uninitiated in asteroid research, this may seem to be an obtuse mistake that would not be common, but the use of the Gaffey et al. (1993) HED zone has not been updated since publication, and is used in nearly every VNIR spectral analysis of asteroids. The nearly 30-year old band parameter analysis methods of Gaffey et al. (1993) have also been long outdated by the more modern methods presented here and used by others (naming only a small subset: Burbine et al., 2007, 2009, 2018; Moskovitz et al., 2010; Reddy et al., 2012; Cloutis et al, 2013; Lindsay et al., 2015; Hardersen et al., 2018; etc.). If possible, I recommend a future researcher to redraw those zones according to their band parameter analysis methods, or use the either the zones shown in this thesis that best match their band parameter analysis.

I did not plot the BIIC vs. BAR zones for the false blue edge, but since it's x-axis is the BAR, like the Gaffey plot, then the subtype zones would shift to longer wavelengths, in a manner likewise to the Gaffey plot. I leave it to a future researcher to redraw those zones if it serves their purpose.

4.2 FsI versus FsII

As stated in the previous section, the calibration equations presented here produce a wide range of asteroidal mineralogical determinations. Among them, there are two kinds

of equations in particular that command the most attention: the BIC and BIIC equations governing derived FsI and FsII, respectively. As is seen in Table 12, the Band I Fs mineralogy is an overestimate compared to the average for HEDs, and the Band II Fs mineralogy is an underestimate for all of the asteroids. This is concerning because if V-type spectra are analogous to HED spectra, and the calibration equations reliably return mineralogy, then the calibration equations should give the same derived mineralogy, within the RMS error. This casts doubt on how applicable the HED calibrations equations are to V-type asteroids. In this section, I explore potential causes to the different Band I and Band II results, and look for potential solutions to increase confidence that we can retrieve mineralogy from V-type asteroid spectra using band parameter analysis methods. The potential causes I consider are temperature corrections, SNR level, Band I slope, space weathering (SW), and composition.

Burbine et al. (2009) responded to this FsI vs. FsII discrepancy by averaging the results. However, Burbine et al. (2018) responded by choosing FsI, and ignoring FsII. The reason they gave was that BIICs were more heavily influenced by temperature corrections than BICs. and since they chose to not perform temperature corrections on their band centers, then by using the band centers that were *less* influenced by temperature (the BICs), they could have greater confidence in their derived mineralogy. However, their sample of V-types came from the NEA population of asteroids, whereas my sample is from the Main Belt. Temperature corrections did not act on their sample in such a way as to bring the band centers into closer agreement with the band centers of the HEDs. However, in my case it did, and I therefore chose to use the temperature corrections (see § 3.3.1). Burbine et al's (2018) mean FsII was, like the mean FsII from my sample, lower than the HED mol% Fs, and also lower than the calibration error (in my case, most of the six versions of FsII were within RMS error). Whereas their mean NEA sample FsI was 43 mol%, a less than 1 mol% difference from the EMPA mean. It therefore makes sense that they would choose to regard the FsI results with confidence, since they agree with the HED FsI. However, what then are we to make of their low FsII mean of 35 mol%?

To see if temperature corrections can help to explain the FsI vs. FsII discrepancy, I examined the V-types FsI - FsII against the surface equilibrium temperature of

asteroids in Figure 48. The blue disks are the values from band centers that have not been corrected for temperature, and the green triangles are from the centers that have been temperature-corrected. If temperature-corrections could help to explain the FsI vs. FsII discrepancy, then we would expect the blue data points to approach zero relative to the blue points. However, I found the opposite trend. The discrepancy between FsI and FsII has worsened after temperature corrections. Therefore while important to account for in a band parameter analysis, the temperature of the asteroids does not explain this disparity.

I introduced noise into the Burbine sample in order to calculate more realistic calibrations for V-type asteroids. It is possible that the lower signal-to-noise data could lead to differences in band parameters. One of the stronger telluric water absorptions spans 1.8 - 2.1 µm, which overlaps with the location of Band II Center. The SNR over this wavelength range was reduced to approximately 25 to simulate the decrease in signal due to telluric water. This could lead to a systematic error in measuring the Band II Center, and thus cause a disparity between mineralogy from Band I and Band II. If the difference in SNR between the meteorites and asteroids are responsible for the Band I versus Band II divergence, then FsI - FsII from the SNR50 calibration equations would be closer to zero than FsI - FsII from the clean equations. However, as seen in Table 14, the derived mineralogy changed very little in response to the added spectral noise. Although FsII did increase by ~1 mol%, approaching the ~43 mol% of the HEDs, FsI sometimes increased, and sometimes decreased. In order to explain the FsI vs. FsII division, the combination of an increasing FsI and a decreasing FsII would have to approach the HED mean 43.6 mol% Fs, within RMS error. Since this does not occur, I conclude that the noise-level of the spectra are not responsible for the FsI vs. FsII disparity.

Figure 38 in § 3.3.3 shows that V-type Band I Slopes are much greater than the HED slopes. The band center is defined as the point of maximum absorption for an absorption feature and is found by dividing the reflectance values of the absorption feature by this slope. This procedure is designed to eliminate the variable of slope to determine the maximum of absorption rather than the minimum reflectance value which

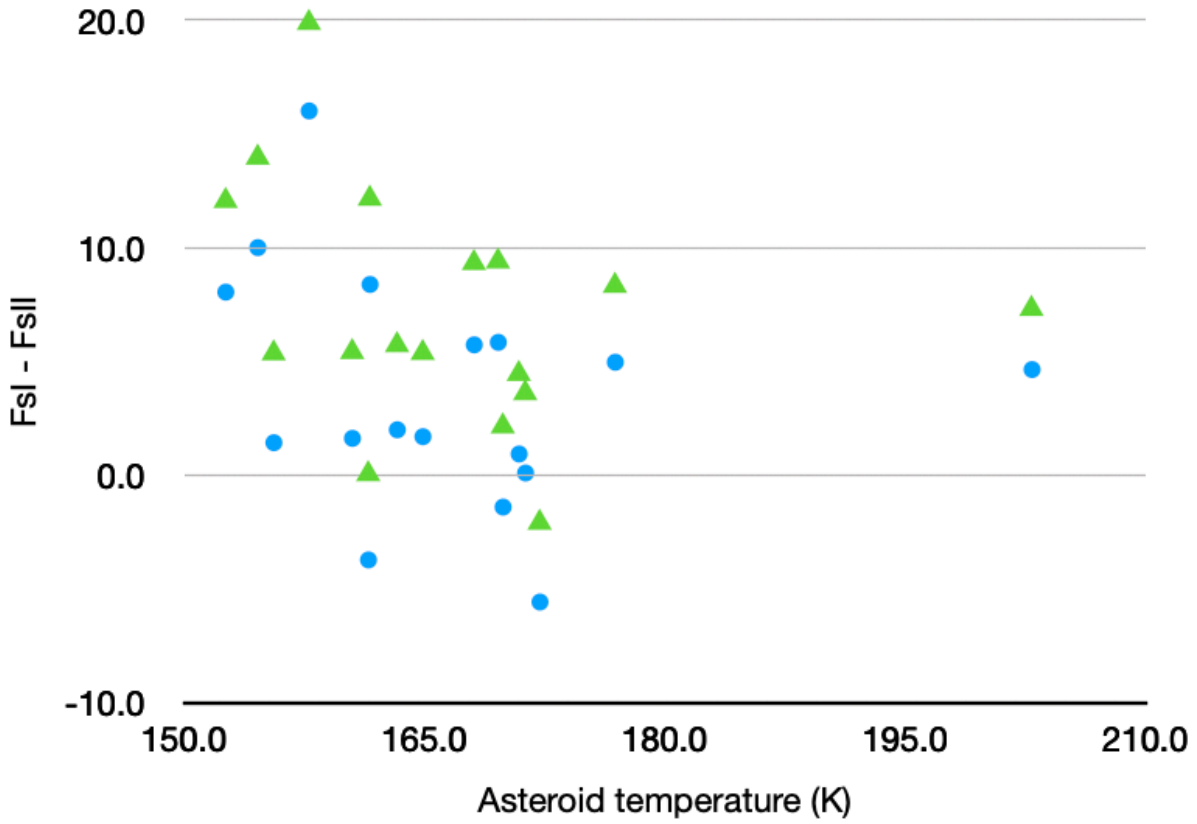

Figure 48: Plots the difference in FsI and FsII for the 17 V-type asteroids. The blue dots are the non-temperature-corrected data points, and the green triangles are temperature-corrected.

is a function of absorption and slope. The mineral chemistry determines the location of maximum absorption. This leads to the expectation that the higher Band I Slopes for the V-types should not affect the determined BICs, and the calibration equations should reliably return asteroid surface mineralogy. The fact that this is not the case indicates that there is a physical mechanism that is increasing the slopes for the asteroids *and* altering the band centers.

An exception to the above slope argument is the case of using the 0.8 µm false blue edge. While measuring a continuum and correcting for it returns the maximum absorption, it only works if the full wavelength range of the band is available. For example, my false blue edge cuts off the reflectance maximum near 0.75 µm, which is required to estimate the continuum. This imposes an artificially high Band I Slope, which will lead measuring an artificially high BIC. For the HEDs, this problem of artificially high BICs is corrected by the the calibration process. However, the greater Band I Slope for the V-types compared to the HEDs results increases the problem resulting with artificially high BICs that are not commensurate with the increase from false blue edge used on HEDs. Since the Fs and Wo mineralogy determined by the calibration equations is directly proportional to BIC, this larger artificial increase to V-type BICs will cause an overestimation of mineralogy when using the false blue edge calibration equations on asteroid data. This effect can be seen by the high FsI average of 58.9 ± 10.8 for V-types in Table 12. Because of this problem, I recommend that for NIR only V-type data sets, mineralogy is best determined using BIIC and their corresponding equations with recognition that mineralogy is likely a few percent underestimate.

The above analysis points toward a physical mechanism that is increasing Band I Slopes and BICs while simultaneously decreasing BIICs. One possible explanation is that asteroids are space weathered. The term "space weathering" encompasses the processes which alter the surface compositions of asteroids, as well as other solar system bodies lacking atmosphere and large magnetic fields (Hapke 2001; Chapman 2004, Fulvio 2012). These include solar wind, cosmic rays, and micrometeorite impacts (Brunetto et al. 2015). SW has been invoked for many years (Chapman, 1979, 2004; Clark et al. 2002) as a possible explanation of the mismatch between S-type asteroids and the OCs. Many

laboratory experiments have attempted to mimic SW by altering the surfaces of meteorites (Hapke, 1965; Moroz et al. 1996; Sasaki et al. 2001; Strazzulla et al. 2005; Marchi et al. 2005; Brunetto et al. 2006b; Loeffler et al. 2008a, 2009; Wasson et al. 2009; Fu et al., 2012; Fulvio et al. 2012). Since pyroxenes are a large component of OCs, as well as HEDs, the effects of these SW experiments on mineral end members, lunar samples and simulants, and OCs are generally applicable to HEDs. The result is a reddening of the spectrum, as well as darkening of the absorption features (Brunetto et al. 2015 and references therein). A reddening of the spectrum translates as higher slopes. Fulvio (2012) points out that the BIS is highly representative of SW alteration (see Hiroi & Sasaki 2001; Strazzulla et al. 2005) and the Bus-DeMeo taxonomy uses slope as a proxy of space weathering (DeMeo et al. 2009). However, as discussed above, the reddening of the slope in itself is not diagnostic of differing mineralogy.

The prevailing belief is that SW does not effect the band centers of silicate absorptions (Brunetto et al. 2015). However, Moskovitz et al. (2010) reports on two sets of SW experiments that have been performed on HEDs. The Bereba eucrite was subjected to ion irradiation to simulate solar wind particles in Vernazza et al. (2006), and the eucrite Millbillillie was subjected to laser irradiation to simulate micrometeorite impacts in Wasson et al. (1997, 1998). Moskovitz et al. (2010) performed a band parameter analysis on the resulting spectra, which returned a fascinating trend: in both cases, the BICs shifted to longer wavelengths, while the BIICs shifted to shorter wavelengths. This corresponds to higher FsI and lower FsII values, which suggest space weathering as the mechanism for the disparity in FsI and FsII in my V-type sample. A caveat is that the fully irradiated spectra no longer resemble the spectra of V-type asteroids, and Moskovitz et al. (2010) suggests this is due to the irradiation process used producing large particle sizes, and therefore should not be considered an analog for space weathered V-types. However, since the shift in BIIC is in the correct direction to explain my derived Band II mineralogy, this suggests that SW could help to explain the FsI/FsII conundrum. Additional experiments showing spectra from a continuum of irradiation levels on more HED meteorites could elucidate this phenomenon.

Finally, there is the case that HEDs and V-type surfaces have different compositions or some non-space weathering surface effect that creates the FsI and FsII differences.

Laboratory measured spectra of pyroxenes, HEDs, and other meteorites also have covered a wide range of sample preparation and measurement techniques included particle size distributions, phase angle, temperature, and composition (Cloutis et al. 1986; Gaffey et al. 1993; Gaffey et al. 2002; Burbine et al. 2002, 2007, 2009, 2018; Klima et al. 2007, 2011; Dunn et al. 2010; Sanchez et al. 2012; Reddy et al. 2012), none of which offer a simple explanation of what causes this FsII and FsII difference in meteorites Additionally, given the long established link based on the similarity of HED, 4 Vesta, and V-type spectra, composition is an unlikely scenario, but it should not be fully discounted. To resolve this problem, more laboratory experiments simulating space weathering and a larger sample of asteroid spectra with measured band parameters are required. It was my goal in this thesis to give future band parameter analysis asteroid researchers new tools with which they can address this problem, as well as more accurately determined band parameters. As it stands, I suggest caution in using band parameters to definitely determine composition. If band parameters are used, however, and if the full Band I feature is available, then the average of FsI and FsII should be used since it results in an answer that appears to best match expectation.

Chapter 5 ☽ Conclusions

In this thesis, I have performed an extensive band parameter analysis on a sample of 13 HEDs whose true mineralogical molar contents are known, and derived new calibration equations. I also calculated the band parameters of a sample of 53 HEDs and 17 V-type asteroids. In particular:

- Using reflectance spectra of HEDs with known mineralogy, I produced a suite of new calibration equations to retrieve mineralogy from V-types asteroids. The calibration equations used a real blue edge and a false blue edge of 0.8 µm and three red edges of 2.40, 2.45, and 2.50 µm. These were chosen to mimic NIR-only data asteroid data (false blue edge) and the observational limitations longword of 2.40 µm of the most often used telescopes with NIR spectrometers.
- I provide the first available calibration equations to be used for NIR-only V-type data sets. This allows researchers the ability to estimate mineralogy for V-types without the need for follow-up visible-light observations made at a separate telescope facility under different observing conditions.
- To generate calibration equations that have molar percentage uncertainties representative of what can be obtained from asteroid spectra with an signal-to-noise ratio (SNR) ~50, I degraded the laboratory spectra of the Burbine sample to asteroid-like SNR and redefined calibration equations. We recommend using this set of equations over the 'clean' when determining the mineralogy of asteroids.
- I provide a variety of explorations in different ways of using and modifying measured band parameters to maximize the usefulness of past and future asteroid studies.
- The traditionally used meteorite zones were updated to our more modern band parameter analysis technique, which is more similar to other currently used techniques than to the method used by Gaffey et al. (1993) that established the original HED zone in BIC vs. BAR space. I also provide newly determine meteorite zones applicable to NIR only data.
- I provide the following recommendations for using calibration equations

- If using published equations, choose the equations that best match your edge choices and details of your band parameter analysis.
- If possible, use the Burbine sample to generate calibration equations for your band parameter analysis method.
- Using the average of mineralogy determined from BIC (FsI & WoI) and BIIC (FsII & WoII) gives mineralogy most similar to the averages of HEDs. I recommend using this average when determining mineralogy of V-type asteroids.
- Due to artificially inflated 0.8-µm false blue BIC values for V-types asteroids, I recommend using BIIC calibration equations if only NIR data is available. The results will be a slight underestimate.
    - However, if your V-type asteroids sample possesses false blue edge BIC values that are not overly inflated, then I recommend averaging the false blue edge FsI results with the FsII results.
- Mineralogy calibration equations for V-types systemically overestimate mineralogy using BICs and underestimate mineralogy using BIICs. For this reason, I conclude that in their current form, these calibration equations will have systematic error that must be noted.
- A potential explanation for this difference is space weathering.

The above conclusions highlight a few salient themes to be taken away from this thesis. First, calibration equations and meteorite zones derived from band parameter analyses are sensitive to the method of the band parameter analysis. Moving forward, asteroid researchers using band parameter analyses to determine V-type mineralogy should develop their own analytical tools or follow the recommendations summarized above. Second, due to the differences in FsI and FsII, the application of calibration equations to V-type asteroids should be taken with caution, and applied with the caveat that FsI is likely an overestimate and FsII is likely an underestimate. The work presented here suggest space weathering on V-type asteroids may be the driving physical mechanism. To resolve this issue, we need more HEDs with measured mineralogy and reflectance spectra, laboratory studies simulating space weathering, and a larger sample of V-type asteroids with visible and near-infrared spectra

Bibliography

Adams, J. B. (1974) 'Visible and near-infrared diffuse reflectance spectra of pyroxenes as applied to remote sensing of solid objects in the Solar System', *J. Geophys. Res.* 79, 4829–4836.

Binzel, R. P. and Xu, S. (1993) 'Chips off of Asteroid 4 Vesta: Evidence for the Parent Body of Basaltic Achondrite Meteorites', Science, 260(5105), pp. 186–191.

Binzel, R. P. et al. (1997) 'Geologic mapping of Vesta from 1994 Hubble Space Telescope images', Icarus, 128(1), pp. 95–103. doi: 10.1006/icar.1997.5734.

Binzel, R. P. amd Lazarro, D. (2000) 'Evidence From a Differentiated AsteroidBeyond 3 AU from the Sun', Meteoritics and Planetary Science, 35(5), p. A26.

Brunetto, R. et al. (2015) 'Asteroid surface alteration by space weathering processes', Asteroids IV, pp. 597–616. doi: 10.2458/azu_uapress_9780816532131-ch031.

Burbine, T. H. et al. (2001) 'Vesta, Vestoids, and the howardite, eucrite, diogenite group: Relationships and the origin of spectral differences', Meteoritics and Planetary Science, 36, pp. 761–781.

Burbine, T. H., Buchanan, P. C. and Binzel, R. P. (2007) 'Deriving Formulas from HED Spectra for Determnining the Pyroxene Mineralogy of Vesta and Vestoids', in 38th LPSC. doi: 10.4009/jsdt.40.1028.

Burbine, T. H. et al. (2009) 'Pyroxene mineralogies of near-Earth vestoids', Meteoritics and Planetary Science, 44(9), pp. 1331–1341. doi: 10.1111/j.1945-5100.2009.tb01225.x.

Burbine, T. H. et al. (2018) 'Can Formulas Derived From Pyroxenes and/or HEDs Be Used to Determine the Mineralogies of V-Type Asteroids?', Journal of Geophysical Research: Planets, 123(7), pp. 1791–1803. doi: 10.1029/2018JE005561.

Burns, R. G. (1970) 'Crystal field spectra and evidence of cation ordering in olivine minerals', American Mineralogist, 55 (9-10): 1608–1632.

Burns, R. G. (1993) 'Mineralogical applications of crystal field theory', United Kingdom: Cambridge University Press.

Bus, S. J. and Binzel, R. P. (2002) 'Phase II of the Small Main-Belt Asteroid Spectroscopic Survey', The observations, Icarus 158, 106-145.

Chapman, C. R. (2004) 'Space weathering of asteroid surfaces', Annual Review of Earth and Planetary Sciences, 32, pp. 539–567. doi: 10.1146/annurev.earth.32.101802.120453.

Clark S. P. 1957. Absorption spectra of some silicates in the visible and near-infrared. American Mineralogist 42:732– 742.

Clark, B. E. et al. (2002) 'Asteroid Space Weathering and Regolith Evolution', Asteroids III, pp. 585–599. Available at: http://adsabs.harvard.edu/abs/2002aste.conf..585C.

Cloutis, E. A. et al. (1986) 'Calibrations of phase abundance, composition, and particle size distribution for olivine-orthopyroxene mixtures from reflectance spectra', Journal of Geophysical Research, 91(B11), p. 11641. doi: 10.1029/jb091ib11p11641.

Cloutis, E.A., Gaffey, M.J. (1993) 'Accessory phases in aubrites: spectral properties and implications for asteroid 44 Nysa', *Earth Moon Planet* 63, 227–243. https://doi.org/10.1007/BF00572470

Cloutis E. A., Hudon P., Romanek C. S., Bishop J. L., Reddy V., Gaffey M. J., and Hardersen P. S. (2010) 'Spectral reflectance properties of ureilites', Meteoritics & Planetary Science 45:1668–1694. doi:10.1111/j.1945-5100.2010.01065.x.

Consolmagno, G. J. and Drake, M. J. (1977) 'Composition and evolution of the eucrite parent body: evidence from rare earth elements', Geochimica et Cosmochimica Acta, 41(9), pp. 1271–1282. doi: 10.1016/0016-7037(77)90072-2.

Delaney J. S., Takeda H., Prinz M., Nehru C. E., and Harlow G. E. (1983) 'The nomenclature of polymict basaltic achondrites', Meteoritics 18:103–111.

Drake, J. (2001) 'The Eucrite/Vesta story', Meteoritics and Planetary Science, 513, pp. 501–513.

Dunn, T. L. et al. (2010) 'Analysis of ordinary chondrites using powder X-ray diffraction: 1. Modal mineral abundances', Meteoritics and Planetary Science, 45(1), pp. 127–138. doi: 10.1111/j.1945-5100.2009.01011.x.

Fulvio, D. et al. (2012) 'Space weathering of Vesta and V-type asteroids: New irradiation experiments on HED meteorites', Astronomy and Astrophysics, 537. doi: 10.1051/0004-6361/201118486.

Gaffey, M. J. (1976) 'Spectral reflectance characteristics of the meteorite classes', Journal of Geophysical Research, 81(5), pp. 905–920. doi: 10.1029/jb081i005p00905.

Gaffey, M. J., Burbine, T. H. and Binzel, R. P. (1993) 'Asteroid Spectroscopy: Progress and Perspectives', Meteoritics, 28, pp. 161–187.

Gaffey, M. J. (1997) 'Surface lithologic heterogeneity of asteroid 4 Vesta', Icarus, 127(1), pp. 130–157. doi: 10.1006/icar.1997.5680.

Gaffey, M. J. et al. (2002) 'Mineralogy of Asteroids BT', Asteroids III, pp. 183–204. Available at: papers2://publication/uuid/A789CEFE-2D07-4930-A9F1-FB79D67E7DF2.

Hapke, B. (1965) ‘Effects of a Simulated Solar Wind on the Photometric Properties of Rocks and Powders’, Annals of the New York Academy of Sciences, pp. 711-xxx, https://doi.org/10.1111/j.1749-6632.1965.tb20395.x

Hapke B. (2001) ‘Space weathering from Mercury to the asteroid belt’, Journal of Geophysical Research 106:10039–10073.

Hardersen P. S., Gaffey M. J., and Abell P. A. (2004) Mineralogy of asteroid 1459 Magnya and implications for its origin. *Icarus, 167,* 170–177.

Hardersen, P. S. et al. (2018) ‘Basalt or Not? Near-infrared Spectra, Surface Mineralogical Estimates, and Meteorite Analogs for 33 V p -type Asteroids ’, The Astronomical Journal. IOP Publishing, 156(1), p. 11. doi: 10.3847/1538-3881/aac3d2.

Hinrichs J. L. and Lucey P. G. (2002) 'Temperature-dependent near- infrared spectral properties of minerals, meteorites, and lunar soil’, Icarus 155:169–180.

Hurlbut, C. S., & Klein, C. (1977) Manual of Mineralogy, 532 pp.

Lindsay, S. S. et al. (2015) ‘Composition, mineralogy, and porosity of multiple asteroid systems from visible and near-infrared spectral data’, Icarus. Elsevier Inc., 247, pp. 53–70. doi: 10.1016/j.icarus.2014.08.040.

Lindsay, S. S. et al. (2016) ‘The Red Edge Problem in asteroid band parameter analysis’, Meteoritics and Planetary Science, 51(4), pp. 806–817. doi: 10.1111/maps.12611.

Lucas, M. P. et al. (2019) ‘Hungaria asteroid region telescopic spectral survey (HARTSS) II: Spectral homogeneity among Hungaria family asteroids’, Icarus. Elsevier, 322(November 2018), pp. 227–250. doi: 10.1016/j.icarus.2018.12.010.

Mayne R. G., McSween H. Y., McCoy T. J., and Gale A. (2009) 'Petrology of the unbrecciated eucrites', Geochimica et Cosmochimica Acta 73:794–819, doi:10.1016/ j.gca.2008.10. 035.

McClure, L.T. and Lindsay, S.S. (2020) 'A Contemporary View of the Ordinary Chondrite Boot that Accounts for Mineralogical Variation', (abstract). 52nd AAS Division of Planetary Sciences Conference.

McSween, H. Y. et al. (2011) 'HED meteorites and their relationship to the geology of Vesta and the Dawn mission', Space Science Reviews, 163(1–4), pp. 141–174. doi: 10.1007/s11214-010-9637-z.

McSween, H. Y. et al. (2013) 'Dawn; the Vesta-HED connection; and the geologic context for eucrites, diogenites, and howardites', Meteoritics and Planetary Science, 48(11), pp. 2090–2104. doi: 10.1111/maps.12108.

Michel, P., DeMeo, F. E. and Bottke, W. F. (2015) 'Asteroids: Recent advances and new perspectives', Asteroids IV, pp. 3–10. doi: 10.2458/azu_uapress_9780816532131-ch001.

Migliorini, F. et al. (1997) 'Vesta fragments from $\nu 6$ and 3:1 resonances: Implications for V-type near-Earth asteroids and howardite, eucrite and diogenite meteorites', Meteoritics and Planetary Science, 32(6), pp. 903–916. doi: 10.1111/ j.1945-5100.1997.tb01580.x.

Moroz, L. V. et al. (1996) 'Optical effects of regolith processes on S-asteroids as simulated by laser shots on ordinary chondrite and other mafic materials', Icarus, 122(2), pp. 366–382. doi: 10.1006/icar.1996.0130.

Moroz L., Schade U., and Wäsch R. (2000) 'Reflectance spectra of olivine-othopyroxene-bearing assemblages at decreased temperatures: Implications for remote sensing of asteroids', Icarus 147:79–93.

Moskovitz, N. A. et al. (2010) 'A spectroscopic comparison of HED meteorites and V-type asteroids in the inner Main Belt', Icarus. Elsevier Inc., 208(2), pp. 773–788. doi: 10.1016/j.icarus.2010.03.002.

Pieters C. M. and Hiroi T. (2004), 'RELAB (Reflectance Experiment Laboratory): A NASA multiuser spectroscopy facility' (abstract #1720). 5th Lunar and Planetary Science Conference. CD-ROM.

Reddy and Sanchez (2016)], Reddy Main Belt Asteroid Spectra V1.0.\ NASA Planetary Data System.

Rubin, A. E. and Grossman, J. N. (2010) 'Meteorite and meteoroid: New comprehensive definitions', Meteoritics and Planetary Science, 45(1), pp. 114–122. doi: 10.1111/j.1945-5100.2009.01009.x.

Sanchez, J. A. et al. (2012) 'Phase reddening on near-Earth asteroids: Implications for mineralogical analysis, space weathering and taxonomic classification', Icarus. Elsevier Inc., 220(1), pp. 36–50. doi: 10.1016/j.icarus.2012.04.008.

Sanchez, J. A. et al. (2020) 'A New Method for Deriving Composition of S-type Asteroids from Noisy and Incomplete Near-infrared Spectra', The Astronomical Journal. IOP Publishing, 159(4), p. 146. doi: 10.3847/1538-3881/ab723f.

Sasaki, S. et al. (2001) 'Production of iron nanoparticles by laser irradiation in a simulation of lunar-like space weathering', Nature, 410, pp. 555–557.

Schade U. and Wäsch R. (1999) 'Near-infrared reflectance spectra from bulk samples of the two SNC meteorites Zagami and Nakhla', Meteoritics & Planetary Science 34:417–424.

Singer R. B. and Roush T. L. (1985) 'Effects of temperature on remotely sensed mineral absorption features', Journal of Geophysical Research 90:12434–12444.

Stolper E. (1977) 'Experimental petrology of eucritic meteorites', Geochim. Cosmochim. Acta 41. pp. 587-611

Strazzulla, G. et al. (2005) 'Spectral alteration of the meteorite Epinal (H5) induced by heavy ion irradiation: A simulation of space weathering effects on near-Earth asteroids', Icarus, 174(1), pp. 31–35. doi: 10.1016/j.icarus.2004.09.013.

Sunshine, J. M. et al. (2004) 'High-calcium pyroxene as an indicator of igneous differentiation in asteroids and meteorites', Meteoritics and Planetary Science, 39(8), pp. 1343–1357. doi: 10.1111/j.1945-5100.2004.tb00950.x.

Tedesco, E.F., Noah, P.V., Noah, M., Price, S.D. (2004) IRAS Minor Planet Survey V6.0. NASA Planetary Data System, IRAS-A-FPA-3-RDR-IMPS-V6.0.

Thomas, P.C., Binzel, R.P., Gaffey, M.J., Storrs, A.D., Wells, E.D., Zellner, B.H. (1997) 'Impact excavation on Asteroid 4 Vesta: Hubble Space Telescope results', Science 277, 1492–1495.

Vernazza, P., Brunetto, R., Strazzulla, G., Fulchignoni, M., Rochette, P., Meyer-Vernet, N., Zouganelis, I. (2006) 'Asteroid colors: A novel tool for magnetic field detection? The case of Vesta', Astron. Astrophys. 451, L43–L46.

Wisdom, J. (1985) 'Meteorites may follow a chaotic route to Earth', *Nature* 315, 731–733). https://doi.org/10.1038/315731a0

Yamaguchi, A., Taylor, G. J. and Keil, K. (1997) 'Metamorphic History of the Eucritic Crust of 4 Vesta', Journal of Geophysical Research, 102(E6), pp. 13381–13386.

Vita

Noah Frere grew up in Syracuse, NY and received a B.A. in Philosophy from Colby College in Waterville, ME in 1995. In 2013 he went back to school at Pellissippi State Community College and The University of Tennessee to pick up the physics and math courses he neglected to take at Colby, and then attended University of Tennessee, Knoxville for graduate school, specializing in astrophysics. While there, he studied Core-collapse Supernovae for one Summer, and then concentrated on asteroids and meteorites thereafter.